Search for Weak Gaugino Production in Final States With One Lepton, Two B-Jets Consistent With a Higgs Boson, and Missing Transverse Momentum With the ATLAS Detector

Search for Weak Gaugino Production in Final States with One Lepton, Two b-jets Consistent with a Higgs Boson, and Missing Transverse Momentum with the ATLAS detector

A dissertation presented

by

Andy Yen

to

The Department of Physics

in partial fulfillment of the requirements

for the degree of

Doctor of Philosophy

in the subject of

Physics

Harvard University

Cambridge, Massachusetts

May 2015

Thesis advisor

John Huth

Author

Andy Yen

Search for Weak Gaugino Production in Final States with One Lepton, Two b-jets Consistent with a Higgs Boson, and Missing Transverse Momentum with the ATLAS detector

Abstract

The ATLAS detector at the Large Hadron Collider is a discovery machine that is able to probe into the multi-TeV scale and search for physics beyond the Standard Model. This thesis presents a search for chargino and neutralino production in final states with one lepton, two b-jets, and missing transverse momentum, consistent with R-parity conserving supersymmetric scenarios. The analysis is based on 20.3 fb^{-1} of $\sqrt{s} = 8$ TeV proton-proton collision data recorded with the ATLAS detector. Observations are found to be consistent with the Standard Model expectations and 95% confidence level limits are obtained in the context of both simplified supersymmetric models and phenomenological Minimal Supersymmetric Standard Models.

Contents

List of Figures

List of Tables

Acknowledgments

There are many people who contributed to making this thesis possible and it would be impossible to list them all. Nevertheless, I would like to give special thanks to a couple people. First, I would like to thank my advisor John Huth for his advice and guidance over the past five years. Without your support and encouragement, the work presented here would not be possible. I would also like to give thanks to the members of my committee, João Pedro Barreiro Guimarães da Costa and Matthew Reece. Thank you for your insightful comments and suggestions.

I would also like to thank the members of the SUSY 1lep2b analysis group who worked on this analysis with me. In particular, Masahiro Morii and Bart Butler for directly advising me at Harvard, but also Zoltan Gecse, Michael Ughetto, Matthew Gignac, Andree Robichaud-Veronneau, and Geraldine Conti. Without your efforts, this analysis would not have been possible.

I would also like to thank David Lopez Mateos and Kevin Mercurio who worked with me on the b-jet performance studies and Andrea Dell'Acqua who worked with me on the New Small Wheel simulation. Your advice and assistance was key to making those projects possible.

I would like to thank the members of the Harvard ATLAS group who I had the pleasure of interacting with over the years. I learned a lot and enjoyed working with all of you. I want to thank Rebecca Krall for her help in reviewing the theoretical sections of this thesis and making my experience at Harvard more enjoyable. I would also like to thank the Caltech CMS group, in particular Harvey Newman and Marat

Gataullin. Thank you for introducing me to particle physics and starting me on this extraordinary journey.

Lastly, I would like to thank my family, especially my parents and grandparents. Thank you for your love and support, without which, I would not have been able to complete this thesis. Thank you!

Chapter 1

Introduction

Back in the 1960's, the theoretical background for the present Standard Model of particle physics was established. In the roughly half century that followed, experimental particle physics has been playing catch up with a number of seminal discoveries, starting with the W and Z bosons at the SPS and LEP colliders, followed by the top quark at the Tevatron collider, and culminating in the discovery of the Higgs boson in 2012 at the Large Hadron Collider (LHC).

Over the past 50 years, the Standard Model has made astoundingly accurate predictions, but we now know that the theory is lacking. For one, it provides no explanation for quantum gravity and does not explain the mystery of dark matter. Since then, a number of theories have been postulated, such as technicolor, supersymmetry, and string theory. However, up to now, none of these have been definitely proven by experiments.

The next frontier of experimental particle physics is to find beyond the Standard Model physics, and it was with this goal in mind that the LHC was constructed. This thesis describes work done at the ATLAS experiment at the LHC on searching for SUSY. The conclusive discovery of the Higgs boson opens up a wide range of new possible SUSY channels. The analysis presented here searches for the direct production of chargino and neutralino through the decay of the neutralino via a Standard Model Higgs. The physics process involved is $pp \to \tilde{\chi}_2^0(\to h\tilde{\chi}_1^0)\tilde{\chi}_1^{\pm}(\to l\nu)$. This analysis has the distinction of being one of the first conducted at the LHC that has the Higgs as a background. We look in the channel with $h \to b\bar{b}$ so the final state we search for is 1 lepton, 2 b-jets, and $\not{E}_T$.

As is typical with any experiment at this scale, much preparation work by thousands of scientists is required before the analysis can even be conducted. In this thesis, work that was conducted to validate b-jet performance is also described. These studies are particularly important for this analysis as good m_{bb} reconstruction will give us a powerful cut to reduce background. Work that was done on upgrades to the ATLAS muon spectrometer is also described. Such upgrades are necessary if we are to perform a similar physics analysis with a muon in the signal at the future High Luminosity LHC.

Chapter 2

Theoretical Background

In this Chapter, the theoretical background on both the Standard Model of particle physics and Supersymmetric models is provided. Both of these are lengthy topics on their own, here the main focus is on the key points which are most relevant for the analysis described in this thesis. As the signature we are searching for contains a Higgs boson, section 2.1 walks through the Standard Model Higgs mechanism. Section 2.2 discusses some of the motivations for SUSY and how the pMSSM model is formulated.

2.1 The Standard Model

The Standard Model of particle physics is currently the best "Theory of Everything" that we have, where everything refers to around 5% of the known universe. All of the Standard Model particles which are predicted by the theory have already been discovered; they are summarized below in Figure 2.1. In the next sections, we will discuss the theoretical background behind these particles and their interactions [37].

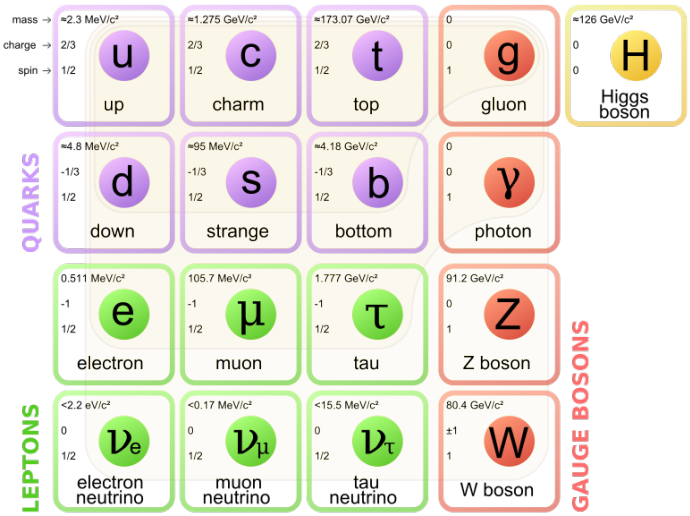

Figure 2.1: All of the Standard Model particles and their properties.[1]

2.1.1 Gauge Groups

We start with a non-abelian gauge theory with gauge group $SU(3) \times SU(2) \times U(1)$. Each matter field ψ transforms under some irreducible representation of this group. Thus the covariant derivative D^μ is defined as:

$$D^\mu = \partial^\mu - igG^\mu - ig_2W^\mu - ig_1B^\mu \tag{2.1}$$

where G^μ are the $SU(3)$ gauge bosons, W^μ are the $SU(2)$ gauge bosons, and B^μ is the $U(1)$ gauge boson, with coupling constants g, g_2, and g_1 respectively. W^μ is a $SU(2)$ 2×2 hermitian matrix which can be expressed as:

$$W^\mu = \begin{pmatrix} W^\mu_{11} & W^\mu_{12} \\ W^\mu_{21} & W^\mu_{22} \end{pmatrix} = \sum W^\mu_a T^{(2)}_a = \frac{1}{2} \begin{pmatrix} W^\mu_z & W^\mu_x - iW^\mu_y \\ W^\mu_x + iW^\mu_y & -W^\mu_z \end{pmatrix} \tag{2.2}$$

where $T^{(2)}_a$ is the usual basis for the Lie algebra $SU(2)$.

2.1.2 The Higgs Field and Symmetry Breaking

Now we can add in the Higgs field which is a complex scalar field with mass dimension 1. In our representation, it can be expressed as:

$$\begin{pmatrix} \phi_1 \\ \phi_2 \end{pmatrix} \tag{2.3}$$

We can add the following operators that respect the symmetries and are renormalizable into our Lagrangian (of course there are more terms in the SM Lagrangian, but these are the only ones we need right now to derive the gauge bosons).

$$\mathcal{L} = -\frac{1}{4}F^{\mu\nu}F_{\mu\nu} - (D_\mu\phi)^\dagger D^\mu\phi - \lambda(|\phi|^2 - v^2)^2 \tag{2.4}$$

The Higgs term in the Lagrangian is quartic and the potential is minimized at each value of ϕ with $|\phi| = v$. Since ϕ is a two-component complex field, there are actually an infinite number of possible minimum. This is shown in Figure 2.2.

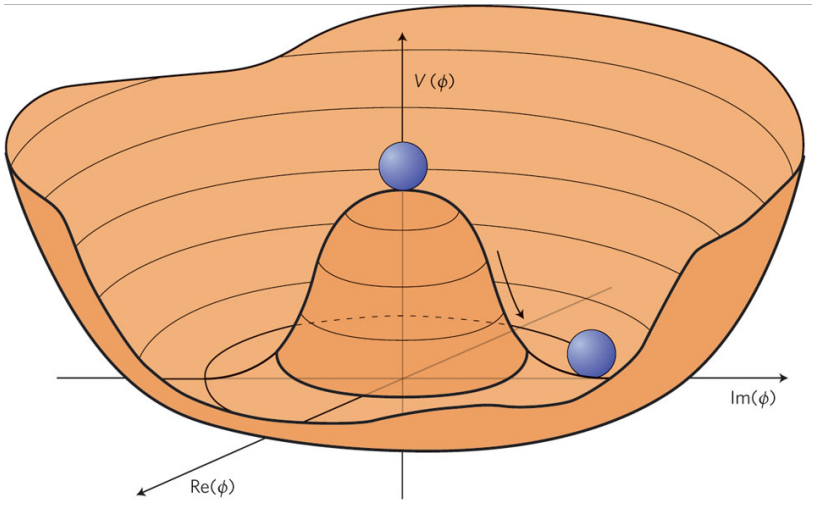

Figure 2.2: The Higgs potential, with the real and imaginary parts of the field ϕ on the x-y plane, and the potential $V(\phi)$ on the z-axis [2].

The Higgs could settle into any of these minima, although we don't really care which because all minima are related by $SU(2)$ rotations. However, because it must pick one minimum, the resulting theory no longer has the full $SU(2)$ symmetry and hence we say that the symmetry has been broken.

We will now arbitrarily pick a Vacuum Expectation Value (VEV) for ϕ, and for simplicity, we pick:

$$\phi_{VEV} = \begin{pmatrix} 0 \\ \\ v \end{pmatrix} \tag{2.5}$$

If nature disagrees with this choice, we will just do a $SU(2)$ rotation to this one. The lowest energy configuration has $\phi(x) = \phi_{VEV}$. We can make a small perturbation $h(x)$ around this minimum and redefine our field as $\phi(x) = h(x) + \phi_{VEV}$. We can substitute this back into our Lagrangian to get the symmetry broken Lagrangian which describes small excitations around the vacuum. Plugging this in, we arrive at:

$$\mathcal{L} = -\frac{1}{4}F^{\mu\nu}F_{\mu\nu} - (D_\mu(h + \phi_{VEV}))^\dagger D^\mu(h + \phi_{VEV}) - \lambda(|(h + \phi_{VEV})|^2 - v^2)^2 \tag{2.6}$$

Instead of expanding all of the Higgs terms out, we only expand the following key term:

$$\mathcal{L} = ... - (D_\mu\phi_{VEV})^\dagger D^\mu\phi_{VEV}... \tag{2.7}$$

$$= ... - \phi^\dagger_{VEV}(ig_2W^\mu + i\frac{g_1}{2}B^\mu)(-ig_2W_\mu - i\frac{g_1}{2}B_\mu)\phi_{VEV}... \tag{2.8}$$

$$= ... - v^2 \left[g_2^2 W_{12}^\mu W_{\mu 21} + (g_2 W_{22}^\mu + \frac{g_1}{2})(g_2 W_{\mu 22} + \frac{g_1}{2} B_\mu) \right] ... \tag{2.9}$$

We can notice that all of the strong interactions dropped because they don't act on ϕ. After the expansion, it becomes clear that we have mass terms for W_{12}, W_{21} and some linear combination of W_{22} and B. We can perform a change of basis to get a more natural basis which gives us mass eigenstates. This basis is defined below as:

$$W_+^\mu = \sqrt{2} W_{12}^\mu = (W_x^\mu - i W_y^\mu)/\sqrt{2} \tag{2.10}$$

$$W_-^\mu = \sqrt{2} W_{21}^\mu = (W_x^\mu + i W_y^\mu)/\sqrt{2} \tag{2.11}$$

$$Z^\mu = -\frac{g_2 W_{22}^\mu + \frac{g_1}{2} B^\mu}{\sqrt{g_2^2/4 + g_1^2/4}} = \frac{g_2 W_Z^\mu - g_1 B^\mu}{\sqrt{g_2^2 + g_1^2}} \tag{2.12}$$

$$A^\mu = \frac{\frac{g_1}{2} W_{22}^\mu - g_2 B^\mu}{\sqrt{g_2^2/4 + g_1^2/4}} = \frac{g_2 B^\mu + g_1 W_Z^\mu}{\sqrt{g_2^2 + g_1^2}} \tag{2.13}$$

This is the particular basis for the $SU(2) \times U(1)$ Lie Algebra that was "selected" by the spontaneous symmetry breaking via the Higgs mechanism. As we know, $W^\pm$ and Z are the W and Z bosons while A is the photon. In this new basis, the mass term given previously in Equation 2.9 can be rewritten as:

$$\mathcal{L} = ... v^2 \left[\frac{g_2^2}{2} W^{+\mu} W_\mu^- + Z^2 \frac{g_2^2 + g_1^2}{4} \right] ... \tag{2.14}$$

Thus, we see that the Higgs gives mass to the three vector bosons, while A does not get a mass term.

2.1.3 Fermions

Next, we can also add fermions to the theory. The fermionic matter fields can be represented as follows:

$$q_L^i = \begin{pmatrix} u_L^{iR} & u_L^{iG} & u_L^{iB} \\ d_L^{iR} & d_L^{iG} & d_L^{iB} \end{pmatrix}_{+1/6}, \psi_L^i = \begin{pmatrix} \nu^i \\ l_L^i \end{pmatrix}_{-1/2} \tag{2.15}$$

$$u_R^i = \begin{pmatrix} u_R^{iR} & u_R^{iG} & u_R^{iB} \end{pmatrix}_{+2/3}, d_R^i = \begin{pmatrix} d_R^{iR} & d_R^{iG} & d_R^{iB} \end{pmatrix}_{-1/3}, (l_R^i)_{-1} \tag{2.16}$$

In this notation, the $SU(2)$ representation is the vertical "vector", and the $SU(3)$ representation is horizontal, and the $U(1)$ hypercharge is the subscript. R,G,B are the color charge which are the labels we give to the three components of a $SU(3)$ representation. The i index ranges from 1 to 3 for the 3 fermion generations in the Standard Model. The L and R notation is for the left and right handed components of the massive spinors. For simplicity, we left out massive neutrinos, but they can be introduced by adding a right-handed neutrino $(\nu_R^i)_0$ to the matter content.

Like with the gauge bosons, fermions also acquire mass through the Higgs boson. After electroweak symmetry breaking, there are new Higgs-fermion interactions and mass terms. When the value of the higgs is shifted by $\phi = h + \phi_{VEV}$, we get new mass terms with $\phi_{VEV} \times$ [fermion] $\times$ [fermion]. These terms look like the following:

$$\begin{aligned} \mathcal{L} = &+v\lambda_l l_L^\dagger l_R + \lambda_l^\dagger v^\dagger l_R^\dagger l_L \\ &+\lambda_d v d_L^\dagger d_R + \lambda_d^\dagger v^\dagger d_R^\dagger d_L \\ &+\lambda_u v u_L u_R^\dagger + \lambda_u^\dagger v^\dagger u_R u_L^\dagger \end{aligned} \tag{2.17}$$

As we have three generations, λ are actually matrices and not scalars. If we redefine some of the left (or right) handed fields by a phase to make the couplings real, this can be simplified down to the following:

$$\mathcal{L} = v\lambda_l \bar{l}l + v\lambda_d \bar{d}d + v\lambda_u \bar{u}u \tag{2.18}$$

2.1.4 CKM Matrix

Now, we look more closely at the last mass term above. If we define $M_u^{ij} = -v\lambda_u$, we get the following term:

$$M_u^{ij} \bar{u}_i u_j \tag{2.19}$$

In general, M_u^{ij} is not diagonal, but we can in fact diagonalize it to obtain

$$m_u \bar{u}u + m_c \bar{c}c + m_t \bar{t}t \tag{2.20}$$

where here u_i are the u, c, t quarks. However, the picture grows a bit more complex when we bring in the down type quarks. The left handed u_i particles form a $SU(2)$ doublet with the d_i particles so if we change the basis of M_u^{ij} in order to diagonalize the matrix, the interaction with d_i will no longer be diagonal. In other words, u_i will now be in a $SU(2)$ doublet with a linear combination of say, d and s quarks. A solution could be to change the basis of d and s, but the down type quarks have their own mass matrix equivalent to Equation 2.19.

$$M_d^{ij} \bar{d}_i d_j \tag{2.21}$$

Thus, fixing d and s to a new basis would make it impossible to simultaneously diagonalize M_d^{ij}. Hence, we must make a choice between diagonalizing both mass matrices versus keeping the interaction matrix diagonal. For quarks, the convention that was chosen is to diagonalize both mass matrices so the mass terms in the Standard Model Lagrangian are as one would expect:

$$\mathcal{L} = ... + \sum_i m_i \bar{q}_i q_i + ... \tag{2.22}$$

where i runs over the 6 quark flavours. The interaction terms however are not diagonal and u_i couples to a linear combination of down type quarks. The interaction terms look as follows:

$$\mathcal{L} = ... + \frac{e}{\sin\theta} W^+ \bar{u}_L^i V_{ij} d_L^j + ... \tag{2.23}$$

The unitary matrix V_{ij} is known as the CKM matrix and the fact that is nearly diagonal appears to just be a fluke of nature. Oddly enough, for leptons, a different convention was chosen. For the "up" type leptons, (the massive charged electrons, muons, and taus), we diagonalize the mass matrix. But we also diagonalize the interaction matrix. This means we get lepton mass and interaction terms that look like the following:

$$\mathcal{L} = ... + m_e \bar{e} e + m_\mu \bar{\mu} \mu + m_\tau \bar{\tau} \tau + ... \tag{2.24}$$

$$\mathcal{L} = ... + \bar{e} W^- \nu_e + \bar{\mu} W^- \nu_\mu + \bar{\tau} W^- \nu_\tau + ... \tag{2.25}$$

But this also means that the second lepton mass matrix, the one for neutrinos cannot be diagonalized so the neutrino mass terms looks like the following:

$$\mathcal{L} = ... + \begin{pmatrix} \bar{\nu}_e & \bar{\nu}_\mu & \bar{\nu}_\tau \end{pmatrix} \begin{pmatrix} M_\nu^{ij} \end{pmatrix} \begin{pmatrix} \nu_e \\ \nu_\mu \\ \nu_\tau \end{pmatrix} + ... \tag{2.26}$$

Thus, we can see how the Standard Model particles acquire mass through the Higgs mechanism and where many of the well known features of the model come from. While it is very successful at describing the spectrum of particles which have been discovered so far, the Standard Model unfortunately doesn't explain everything we know about Nature. In the next section, we will introduce an additional symmetry to try to fix some of these shortcomings.

2.2 Supersymmetry

While the Standard Model just described is a remarkably accurate description of Nature as observed in numerous particle physics experiments, it does have a couple major shortcomings. Notably, there is no explanation for dark matter. While the Standard Model neutrinos could be a dark matter candidate, they alone cannot account for the measured dark matter density. Furthermore, the gauge couplings do not naturally unify and the Higgs boson mass is unstable when radiative corrections are applied. Because of these shortcomings, starting from the mid-1960's, alternative theories were investigated. Among those new theories is Supersymmetry (SUSY) which was proposed in various guises starting from 1966 and onwards [49] [56] [51].

In this section, we take a closer look at the SUSY theory and put it in the context of contemporary experiments such ATLAS at the LHC.

2.2.1 The Hierarchy Problem

One of the main motivations for SUSY is the so called "hierarchy problem". Essentially, in the Standard Model, the Higgs doublet has a quadratically divergent self-energy correction. A good way to understand this is through analogy with electromagnetism. In electromagnetism, the observed mass of the electron can be thought of as

$$(m_e c^2)_{obs} = (m_e c^2)_{bare} + \Delta E_{coulomb} \tag{2.27}$$

where

$$\Delta E_{coulomb} = \frac{1}{4\pi}\frac{e^2}{r_e} \tag{2.28}$$

The bare mass is the mass of the electron without the contribution to the mass coming from the electron self energy. An electron in a vacuum has an electric field around it which has the energy given in Equation 2.28 where r_e is the "size" of the electron in the classical sense. Since the Coulomb self-energy is present for every electron, we can consider it as part of the electron rest energy, and as a result, it gives an additional contribution to the mass of the electron. Using the classical r_e, we find that $\Delta E_{coulomb} \approx 10$ GeV which means a remarkable amount of fine tuning is needed to get the observed electron mass of 0.511 MeV.

The resolution to this is that we know classical electromagnetism is not valid for short distances and that the electron has a partner, the positron. We also know that the world is quantum mechanical so there can be vacuum fluctuations which lead to e^+e^- pair production and these additional diagrams mostly cancel the $\Delta E_{coulomb}$ divergence leaving just a leftover term that is a *log*. A similar scheme can be applied to the Higgs as shown in Figure 2.3.

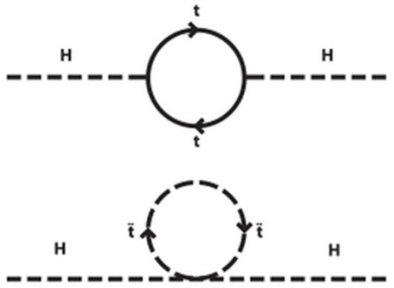

$$\Delta\mu_H^2 = -\frac{\lambda_f^2}{8\pi^2}[\Lambda_{UV}^2 + H.O.T]$$

$$\Delta\mu_H^2 = \frac{\lambda_s}{8\pi^2}[\Lambda_{UV}^2 + H.O.T]$$

Figure 2.3: Higgs loops with top and stops.

Λ_{UV}^2 is the ultraviolet cutoff (the scale up to which the Standard Model is valid), and H.O.T. is short for Higher Order Terms. When adding a stop to the model, we have a similar loop diagram. The different spins give a different sign while the couplings remain the same, which causes the leading pieces in $1/r_H$ to cancel between the top and stop contributions. The leftover H.O.T. is given below by Equation 2.29 [50].

$$\Delta\mu_{H,top}^2 + \Delta\mu_{H,stop}^2 = -C\lambda(m_{\tilde{t}}^2)log\frac{1}{r_H^2 m_{\tilde{t}}^2} \tag{2.29}$$

where C is some O(1) constant. We notice that for $\Delta\mu^2$ to be on the order of m_H^2, $m_{\tilde{t}}^2$ cannot be too large or otherwise the hierarchy problem motivation for SUSY becomes not as good. Ideally, we do not want $m_{\tilde{t}}^2$ too far above the electroweak scale (246

GeV, the VEV of the Higgs field and the typical energy of processes described by the electroweak theory).

2.2.2 An Extra Symmetry Between Bosons and Fermions

SUSY is a symmetry between bosons and fermions and hence it relates particles with different spins. It can be written down as an operator Q which transforms bosons into fermions, $Q|\text{Boson}\rangle = |\text{Fermion}\rangle$, and vice versa. Particles related by this transformation are known as superpartners and all particles in supersymmetric theories fall into supermultiplets which have both bosonic and fermionic components. Superpartners of SM Bosons are named with the suffix "ino" while superpartners of SM Fermions get a "s" prefix. Building off of the existing Standard Model, we get the particle spectrum shown in Table 2.1.

SM	spin	SUSY	spin	name
γ, Z^0, h^0	1,0	$\tilde{x}_1^0, \tilde{x}_2^0, \tilde{x}_3^0, \tilde{x}_4^0$	$\frac{1}{2}$	neutralino
$W^\pm$	1	$\tilde{x}_1^\pm, \tilde{x}_2^\pm$	$\frac{1}{2}$	chargino
$e^-, \nu_e, \mu^-, \nu_\mu, \nu_\tau$	$\frac{1}{2}$	$\tilde{e}_R, \tilde{e}_L, \tilde{\mu}_R, \tilde{\mu}_L, \tilde{\nu}_e, \tilde{\nu}_\mu, \tilde{\nu}_\tau$	0	slepton
τ^-	$\frac{1}{2}$	$\tilde{\tau}_1, \tilde{\tau}_2$	0	stau
u, d, s, c	$\frac{1}{2}$	$\tilde{u}_R, \tilde{u}_L, \tilde{d}_R, \tilde{d}_L, \tilde{s}_R, \tilde{s}_L, \tilde{c}_R, \tilde{c}_L$	0	squark
g	1	$\tilde{g}$	$\frac{1}{2}$	gluino
b	$\frac{1}{2}$	$\tilde{b}_1, \tilde{b}_2$	0	sbottom
t	$\frac{1}{2}$	$\tilde{t}_1, \tilde{t}_2$	0	stop

Higgs	h, A, H^0, H^+, H^-

gauginos	$\tilde{W}^+, \tilde{W}^-, \tilde{W}^3, \tilde{B}^0$
higgsinos	$\tilde{H}_u^0, \tilde{H}_d^0, \tilde{H}_u^+, \tilde{H}_d^-$

Table 2.1: Summary of Standard Model and SUSY particles.

There is actually a bit of subtlety to the description in Table 2.1 above, the main

one being that the neutralinos and charginos are actually the mass eigenstates that arise when you mix the gauginos and higgsinos. We will look at this in more depth in Section 2.2.3.

It is also worth noting that for the Spin-0 sfermions, L and R take on different meanings. In the Standard Model, left and right handed "particles" are just different representations under $SU(2)$. They have the same mass and we just flip the spin to go from one to another. In SUSY, the L and R states are not related in the same way and they can have different masses. For heavy sfermions, the L and R states mix as shown in Equation 2.30 and one needs to diagonalize M_{ij} in order to get the stop and sbottom states.

$$\begin{pmatrix} \tilde{t}_L^\dagger & \tilde{t}_R^\dagger \end{pmatrix} \begin{pmatrix} M_{11} & M_{12} \\ M_{21} & M_{22} \end{pmatrix} \begin{pmatrix} \tilde{t}_L \\ \tilde{t}_R \end{pmatrix} \tag{2.30}$$

The same is also true for the $\tilde{b}_1$ and $\tilde{b}_2$ states. Next, we will take a closer look at the Higgs sector in SUSY.

2.2.3 Supersymmetric Higgs Sector

In the Standard Model, we have a single Higgs doublet:

$$H = \begin{pmatrix} H^+ \\ H^0 \end{pmatrix} \tag{2.31}$$

In SUSY, we need two Higgs doublets, H_u and H_d in order to give mass to both down and up type quarks. As there are 4 degrees of freedom in each doublet, we have

a total of 8 degrees of freedom. This is also known as the two Higgs doublet model (2HDM). In this model, there are a total of 8 Higgs, but 3 are Goldstone bosons which are "eaten" by the gauge bosons to gain mass though the mechanism described in Section 2.1.2. As complex scalar fields have two real degrees of freedom, while massive abelian vector fields have three real degrees of freedom, the longitudinal polarization degree of freedom is provided by the Goldstone boson which is "eaten". This leaves us with a model that has 5 Higgs compared to 1 in the Standard Model. This is shown below in Table 2.2.

Electroweak symmetry breaking (EWSB) leads to a mixing between charged electroweak gauginos and charged higgsino while a combination of electroweak symmetry breaking and SUSY breaking lead to a mixing of neutral gauginos and neutral higgsinos. Like with Standard Model symmetry breaking, this comes from a change of basis. Table 2.2 shows this graphically.

We see that in addition to the SM gauge bosons, the 2HDM gives us 5 Higgs, three neutral and two charged. The supersymmetric gauginos and higgsinos also mix and the resulting mass eigenstates give us the neutralinos and charginos.

2.2.4 SUSY Breaking and R-parity

One obvious problem with what has been described so far is that we haven't seen any superpartners in experiments yet. This is troublesome because if SUSY is an exact symmetry, the superpartners should be mass degenerate with their Standard Model counterparts and be readily accessible in existing experiments. The conundrum is resolved using an old workaround - symmetry breaking. In the SUSY case however,

SM Particle	2HDM	2HDM before EWSB	SUSY	Mass Eigenstates
H	h^0 (1)	H_u^0	$\tilde{H}_u^0$	$\tilde{x}_1^0$
	H^0 (1)	H_d^0	$\tilde{H}_d^0$	$\tilde{x}_2^0$
	A (1)			$\tilde{x}_3^0$
γ	γ (2)	B	$\tilde{B}$	$\tilde{x}_4^0$
Z	Z (3)	W^3	$\tilde{W}^3$	
W^+	W^+ (3)	W^+	$\tilde{W}^+$	$\tilde{x}_1^+$
	H^+ (1)	H_u^+	$\tilde{H}_u^+$	$\tilde{x}_2^+$
W^-	W^- (3)	W^-	$\tilde{W}^-$	$\tilde{x}_1^-$
	H^- (1)	H_d^-	$\tilde{H}_d^-$	$\tilde{x}_2^-$

Table 2.2: Summary of the progression from Standard Model particles to 2HDM and SUSY particles shown previously in Table 2.1 The numbers in the () in the second column indicate the number of degrees of freedom. The intersecting lines represent mixing/change of basis.

it is not spontaneous symmetry breaking, but explicit symmetry breaking.

Effectively, we add SUSY breaking terms to the SUSY Lagrangian to increase the mass of the superpartners. This is called "soft" SUSY breaking as the new terms still prevent the quadratic divergence in the Higgs mass. One problem with this prescription is that if we were to add all SUSY breaking terms allowed by $SU(3) \times SU(2) \times U(1)$ gauge invariance, we would get baryon and lepton number violating terms which would contribute to proton decay. One possible way to resolve this is to introduce the concept of R-parity which is defined as:

$$R_p = (-1)^{2s+3B+L} \tag{2.32}$$

Here s is spin, B is baryon number, and L is lepton number. Hence all Standard Model particles have R=1 while all SUSY particles have R=-1. Forcing R-parity conservation excludes a lot of potential "soft" breaking terms and rids us of the proton decay problem. While R-parity is a sufficient condition, it is not by any means necessary. A stable proton can also be achieved by either B-parity or L-parity alone and there is actually an entire realm of R-parity violating theories.

R-parity conservation creates some interesting consequences. The first is that all SUSY particle interactions must occur in pairs. Hence, the lighest particle with odd R-parity must be stable. This particle is also sometimes called a Lightest Supersymmetric Particle, or LSP for short, and could be a potential candidate for Dark Matter.

2.2.5 The Minimal Supersymmetric Standard Model

Now we take a more precise look at a specific SUSY model. At ATLAS, one of the most commonly searched for model is the Minimal Supersymmetric Standard Model (MSSM). As the name suggests, the MSSM is a minimal SUSY model which has one partner for each Standard model particle and no "extra" particles. It assumes a minimal gauge group, e.g. the MSSM is based on the same $SU(3) \times SU(2) \times U(1)$ gauge symmetry as the Standard Model. It also is R-parity conserving and has soft SUSY breaking.

A fairly complete formulation of supersymmetric Lagrangians can be found in reference [48]. Here we just touch on a couple interesting parts which are most relevant

for understanding the Direct Gaugino search described in this thesis and help lead us to the pMSSM models which are discussed in Section 2.2.6.

For 4 dimensional SUSY models, the Lagrangian can be specified by three functions of matter fields, the superpotential W, the Kahler potential K, and the gauge kinetic function f. The most general superpotential that satisfies gauge invariance, R-parity conservation, and is also renormalizable can be written as:

$$W = \sum_{i,j=gen} Y^u_{ij}\tilde{u}^i_R \tilde{H}_u.\tilde{Q}^j + Y^d_{ij}\tilde{d}^i_R \tilde{H}_d.\tilde{Q}^j + Y^l_{ij}\tilde{l}^i_R \tilde{H}_u.\tilde{L}^j + \mu \tilde{H}_u.\tilde{H}_d \tag{2.33}$$

The first three terms are just generalizations of the Standard Model Yukawa interactions while the last term is the supersymmetric Higgs mass term. The MSSM soft susy breaking terms can thus be written as:

$$\mathcal{L}_{\text{gaugino}} = -\frac{1}{2}\left[M_1 \tilde{B}\tilde{B} + M_2 \sum_{a=1}^{3} \tilde{W}^a \tilde{W}_a + M_3 \sum_{a=1}^{8} \tilde{G}^a \tilde{G}_a \ + \ \text{h.c.}\right] \tag{2.34}$$

$$\mathcal{L}_{\text{sfermions}} = \sum_{i=gen} m^2_{\tilde{Q},i}\tilde{Q}^\dagger_i \tilde{Q}_i + m^2_{\tilde{L},i}\tilde{L}^\dagger_i \tilde{L}_i + m^2_{\tilde{u},i}|\tilde{u}_{R_i}|^2 + m^2_{\tilde{d},i}|\tilde{d}_{R_i}|^2 + m^2_{\tilde{l},i}|\tilde{l}_{R_i}|^2 \tag{2.35}$$

$$\mathcal{L}_{\text{Higgs}} = m^2_{H_u} H^\dagger_u H_u + m^2_{H_d} H^\dagger_d H_d + B\mu(H_u.H_d + \text{h.c.}) \tag{2.36}$$

$$\mathcal{L}_{\text{tril.}} = \sum_{i,j=gen} \left[A^u_{ij} Y^u_{ij} \tilde{u}_{R_i} H_u.\tilde{Q}_j + A^d_{ij} Y^d_{ij} \tilde{d}_{R_i} H_d.\tilde{Q}_j + A^l_{ij} Y^l_{ij} \tilde{l}_{R_i} H_u.\tilde{L}_j \ + \ \text{h.c.}\right] \tag{2.37}$$

$$V_{\text{soft}} = \mathcal{L}_{\text{gaugino}} + \mathcal{L}_{\text{sfermions}} + \mathcal{L}_{\text{Higgs}} + \mathcal{L}_{\text{tril.}} \tag{2.38}$$

Here, the abbreviation *h.c.* stands for Hermitian Conjugate. Looking closer at the SUSY breaking terms, we see that the first one (Equation 2.34) gives mass to gluinos, winos, and binos (The B is the bino, which is the superpartner of the Standard Model $U(1)$ gauge field). The second equation (Equation 2.35) gives mass to the scalar fermions. The third equation (Equation 2.36) are the Higgs mass terms and also a billnear coupling for B. Finally, the fourth equation (Equation 2.37) includes A which is a trilinear coupling between sfermions and Higges.

In total the soft SUSY breaking terms introduce 105 new parameters, which combined with the 19 from the Standard Model give us a model with a total of 124 free parameters. This is a huge amount and is a motivation for the pMSSM models which have a much reduced parameter space. Of the parameters in the model, there are a couple that are of particular interest which we define below.

- M_1, M_2 - Also commonly written as $M_{1/2}$, and called the Gaugino mass.
- μ - The Higgsino mass term.
- tanβ - The ratio of the Vacuum Expectation Value (VEV) of the two Higgs doublets.

We can see how these variables impact the physics by writing down in more detail the mass matrices for the neutral and charged inos. The 4×4 mass matrix for the neutral inos is given below in Equation 2.39.

(2.39)

$$(\tilde{B}\ \tilde{W}^3\ \tilde{H}_d^0\ \tilde{H}_u^0)\begin{pmatrix} M_1 & 0 & -m_Z s_W c_\beta & m_Z s_W s_\beta \\ 0 & M_2 & m_Z c_W c_\beta & -m_Z c_W s_\beta \\ -m_Z s_W c_\beta & m_Z c_W c_\beta & 0 & -\mu \\ m_Z s_W s_\beta & -m_Z c_W s_\beta & -\mu & 0 \end{pmatrix}\begin{pmatrix} \tilde{B} \\ \tilde{W}^3 \\ \tilde{H}_d^0 \\ \tilde{H}_u^0 \end{pmatrix}.$$

Here, the abbreviations $s_W = \sin\theta_W$, $c_W = \cos\theta_W$, $s_\beta = \sin\beta$, and $c_\beta = \cos\beta$. We notice that if $M_{1/2}$ and μ are large compared to m_Z, then the neutralinos are close to their weak eigenstates, bino and wino, but the higgsinos are mixed to form symmetric and anti-symmetric linear combinations. The mass matrix for the charged inos is given below in Equation 2.40.

$$\begin{pmatrix} \tilde{W}^- & \tilde{H}_d^- \end{pmatrix}\begin{pmatrix} M_2 & \sqrt{2}m_W s_\beta \\ \sqrt{2}m_W c_\beta & \mu \end{pmatrix}\begin{pmatrix} \tilde{W}^+ \\ \tilde{H}_u^+ \end{pmatrix} + h.c. \tag{2.40}$$

We see that this matrix is nearly diagonal in the regime where m_W is small compared to $M_{1/2}$ and μ and so the chargino states are close to the weak eigenstates winos and higgsinos.

2.2.6 Phenomenological MSSM

As we have seen in the previous section, the most general MSSM has a huge number of free parameters so in order to make the theory more tractable, we need to dramatically reduce the number of parameters. We do this through applying phenomenological constraints, and the resulting model is known as phenomenological MSSM, or pMSSM for short. Three new assumptions are made in order to constrain the model.

First, all new CP-violations are disallowed. In the Standard Model, CP-violations in the CKM matrix give a tiny electron electric dipole moment (EDM). Since the existing experimental EDM limits are very tiny, it is unlikely that SUSY will contribute any additional CP-violations as such an effect would have already been noticed in experiments.

We also apply the condition that there are no Flavour Changing Neutral Currents (FCNC). Like with CP-violation, FCNC is strongly constrained by existing experimental results, and in the Standard Model theory, they are killed by the GIM mechanism. Finally, we add the constraint of first and second sfermion generation universality. This has the consequence of setting the scalar masses the same for both the first and second generations. The universality constraint helps to cope with the constraints on Δm_k from kaon oscillation experiments. If we consider just the first two generations, we can pick a basis where the down-type Yukawa matrix, $\lambda_d^{ij} v_d$, is diagonal. However, if we pick this basis, the squark mass matrices can have off-diagonal terms as shown below.

$$\lambda_d^{ij} v_d = \begin{pmatrix} m_d & 0 \\ 0 & m_s \end{pmatrix} \qquad m_Q^{2ij} = \begin{pmatrix} m^2_{\tilde{d}_L} & m^2_{Q,12} \\ m^{2*}_{Q,12} & m^2_{\tilde{s}_L} \end{pmatrix}, \qquad m_D^{2ij} = \begin{pmatrix} m^2_{\tilde{d}_R} & m^2_{D,12} \\ m^{2*}_{D,12} & m^2_{\tilde{s}_R} \end{pmatrix}. \tag{2.41}$$

The off diagonal terms give the 2-point vertices that change squark flavour and thus SUSY gives a new contribution to kaon oscillation as shown in Figure 2.4.

This contribution can be eliminated by constraining the MSSM by making the

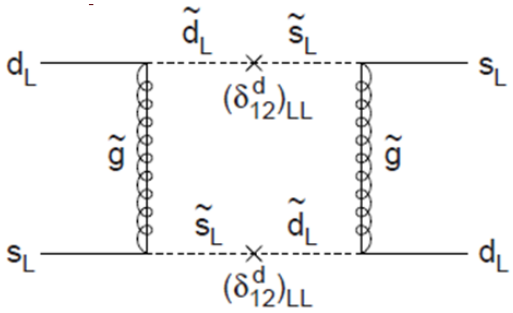

Figure 2.4: A Feynman diagram which gives rise to Δm_K.

squark mass matrices diagonal. After all these constraints are applied, we end up with a more tractable pMSSM model with just the 19 parameters listed below.

$\tan\beta$: ratio of the VEV of the Higgs doublets.

M_A: mass of pseudo-scalar Higgs.

μ: Higgs mass parameter.

M_1, M_2, M_3: bino, wino and gluino mass parameters.

$m_{\tilde{q}}, m_{\tilde{u}_R}, m_{\tilde{d}_R}, m_{\tilde{l}}, m_{\tilde{e}_R}$: first/second generation sfermion masses.

$m_{\tilde{Q}}, m_{\tilde{t}_R}, m_{\tilde{b}_R}, m_{\tilde{L}}, m_{\tilde{\tau}_R}$: third generation sfermion masses.

A_t, A_b, A_τ: third generation trilinear couplings.

2.2.7 Constraints on SUSY

In addition to the constraints applied by the pMSSM conditions on the number of free parameters, many of the SUSY parameters themselves are constrained in terms of the values that they can take. For instance, the condition $1.2 < \tan\beta < 65$ must be satisfied if we want the top and bottom quark Yukawa's to be more or less perturbative [48].

There are also additional constraints that come about as a result of the recent discovery of the Higgs boson at 125 GeV. A Higgs boson at 125 GeV is actually relatively heavy for most pMSSM models. In fact, at tree level, we get the constraint $m_h < m_Z \cos(2\beta)$. However, when we add in 1-loop stop corrections, we get

$$m_h^2 = m_Z^2 c_{2\beta}^2 + \frac{3m_t^4}{4\pi^2 v^2}(\log(\frac{m_{\tilde{t}_1} m_{\tilde{t}_2}}{m_t^2}) + \frac{X_t^2}{m_{\tilde{t}_1} m_{\tilde{t}_2}}(1 - \frac{X_t^2}{12 m_{\tilde{t}_1} m_{\tilde{t}_2}})) \tag{2.42}$$

where

$$X_t = A_t - \mu \cot \beta \tag{2.43}$$

One consequence of this is that the acceptable value of $\tan\beta$ is more constrained [28]. Values of $\tan\beta < 3.5$ are disfavored, and contemporary ATLAS SUSY searches are almost exclusively looking in the region of phase space with $\tan\beta > 10$. A relatively heavy 125 GeV Higgs also favors maximal mixing of stops (which yields large values of A_t), or very heavy stops. In general, even though large slices of parameter space are excluded with each additional GeV of m_h, as we see in Chapter 6, there are still ample room in phase space for MSSM to reside.

Finally, it is worth mentioning that if SUSY is not found at the LHC, the theory would become highly disfavoured, but it still cannot be ruled out conclusively as there are still places that SUSY could hide. For example, if the lightest squark is nearly degenerate with the LSP, there would be very soft jet signatures which could not be picked up by the LHC detectors. Whatever the case, it is certain that the now ongoing 13 TeV run at the LHC will be a very exciting time for SUSY searchers.

Chapter 3

The Large Hadron Collider and the ATLAS Detector

The Large Hadron Collider (LHC) is the world's largest and most powerful particle collider. Its completion marked the culmination of over 20 years of research and development by over 10,000 scientists from over 100 countries. With it came the capability to not only do precise measurements of the Standard Model, but also the ability to probe for new physics such as SUSY.

In this Chapter, we give an overview of the collider before focusing on the ATLAS detector which is used in all of the work presented in this thesis. The ATLAS detector is just one of four major experiments sitting at the four LHC particle beam intersection points. Two detectors, ATLAS and CMS are considered general purpose detectors while ALICE and LHCb are designed for studying heavy ion collisions and B-physics respectively.

3.1 The Large Hadron Collider

The LHC was first turned on in September 2008 and began collecting significant amounts of physics data in 2011. The collider itself is situated in the former LEP tunnel and is approximately 27 kilometers in circumference and situated between 50 and 150 meters underground. In its present form, the LHC is designed to run at 10^{34} $\text{cm}^{-2}\text{s}^{-1}$ for approximately 10 years. Some of the upgrade initiatives which are underway are discussed in more depth in Chapter 4. An aerial view of the LHC is shown in Figure 3.1.

Figure 3.1: Aerial view of the LHC collider with Geneva airport in the foreground. Photo Credit: CERN

3.1.1 LHC Magnets

The LHC features the world's largest cryogenic system which runs at 1.8 K using 96 tons of liquid helium. This is used to cool 1232 superconducting dipole magnets which are used for beam circulation, and 392 quadrupoles for beam focusing. The dipole magnets have a field of 8.33 Tesla which is used to bend the proton beams

around the ring. A cross section of one of the dipoles is shown below in Figure 3.2. There are two dipoles next to each other and two beam pipes, one for each beam which travel in opposite directions.

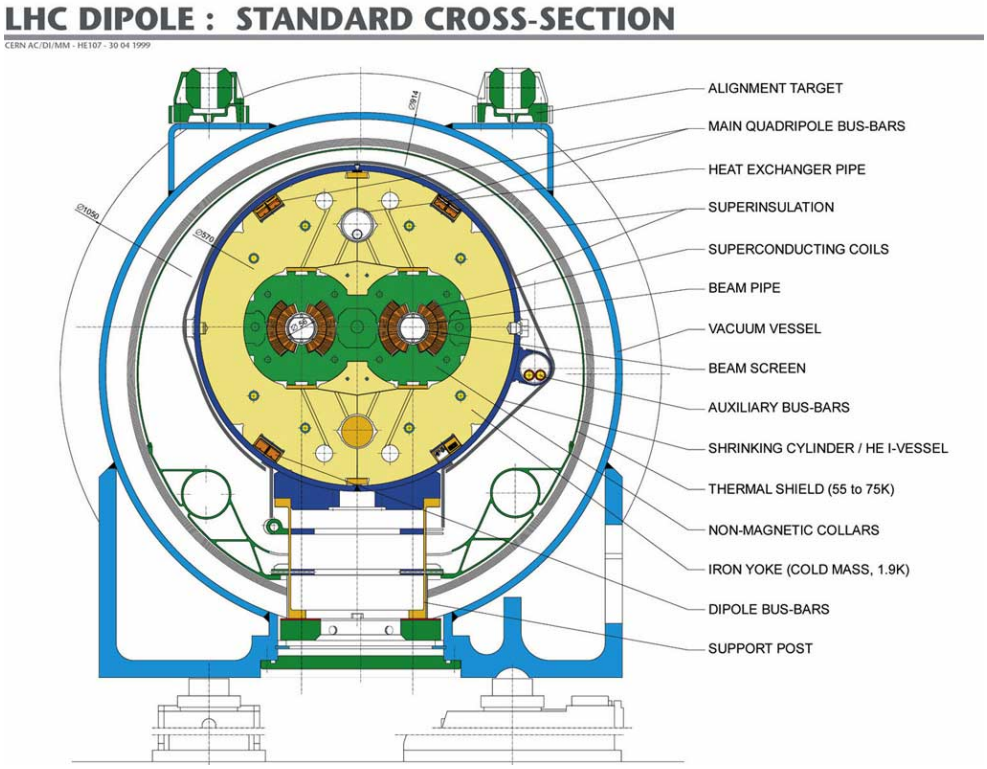

Figure 3.2: Cross section of a LHC dipole magnet [3].

The LHC also makes use of 4 RF cavity systems running at 400 MHz to accelerate the protons. The RF cavity systems accelerate the protons and keep them bunched together. Figure 3.3 shows now the RF cavities work.

Protons which are "slow" at arriving will get a lower energy kick and arrive later the next time. On the other hand, protons which arrive late will get a higher energy kick and arrive earlier the next time. As a result, the protons will bunch up. The periodicity of this bunching is determined by the length of the tunnel and the RF

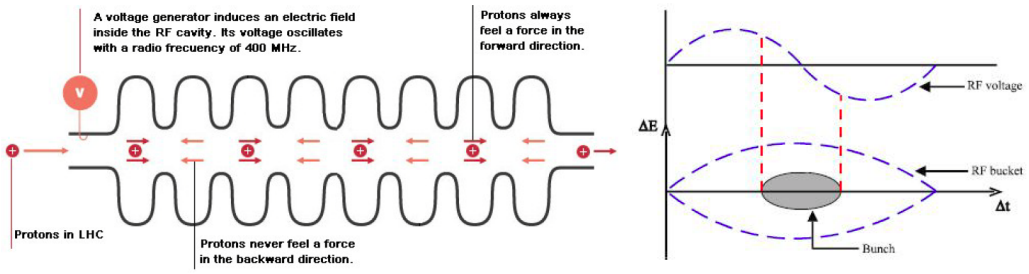

Figure 3.3: Operating principles of the LHC RF cavity system [4].

frequency. At the LHC, there are a total of around 3500 "buckets" and buckets which are filled with protons are known as bunches. A series of bunches are called a "train". The LHC was designed to have a total of 2808 bunches per beam with 25 ns of spacing, and an approximate beam lifetime of 10 hours. During the 2012 run which was used for the analysis presented in this thesis, we used half as many bunches with a spacing of 50 ns. Each bunch contains around 10^{11} protons which are focused down into an area of 16 μm^2 at the interaction points. Even so, the vast majority of protons actually pass through without colliding.

3.2 The ATLAS Detector

As mentioned earlier, the ATLAS experiment is one of the two general purpose detectors at the LHC. It derives its name from **A** **T**oroidal **L**HC **A**pparatu**S**. Together with CMS, it provides a good way for results to be cross checked at two independent detectors. General purpose here means that ATLAS is well equipped to perform a wide range of physics searches, ranging from searching for the Higgs to also searching for models like SUSY. A schematic of the ATLAS detector is shown below in Figure

3.4.

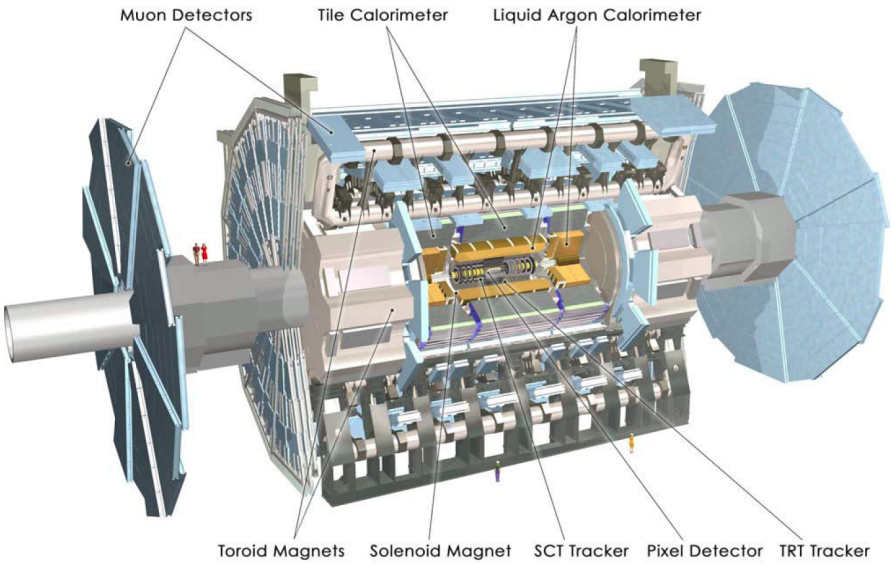

Figure 3.4: Cross sectional view of the ATLAS detector [22].

The detector can be separated roughly into two regions, barrel and endcap, with the switchover at approximately $|\eta| \approx 1.5$, where η is the psuedorapidity. The ATLAS detector is described at length in reference [22]. Here we give a briefer overview with a bigger focus on the muon detector technologies to allow for better comparison to the next generation muon detectors described in Chapter 4.

3.2.1 ATLAS Magnets

The ATLAS detector has a rather complex magnetic field system. The magnetic field is used in order to measure charged particles as charged particles will bend in the magnetic field and the direction and amount of bending allows us to determine the charge and the momentum of the particle. Figure 3.5 shows the layout of the

ATLAS magnets.

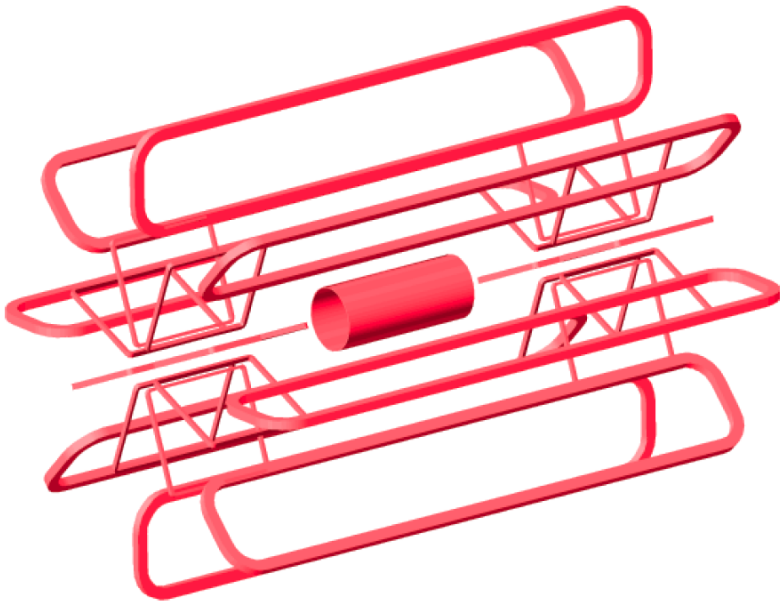

Figure 3.5: A view of the solenoid and toroid magnets used in ATLAS without the other detector components [21].

The center solenoid magnet provides a field of 2T and surrounds the tracking detectors. It has an extremely thin design which is only 0.66 radiation lengths (X_0, the radiation length, is the mean distance over which an electron loses 63% of its energy) to prevent too much energy loss or scattering prior to particles entering the calorimeters. In addition to the solenoid, the ATLAS barrel and endcap regions have toroid magnets (1 in the barrel, 1 for each endcap) which can provide a peak field of approximately 4 Tesla. The magnetic field throughout the detector is monitored at all times using a combination of NMR and Hall probes as uncertainty in the B field can be a large source of particle measurement error.

3.2.2 Inner Detector

The ATLAS inner detector (ID) consists of three types of detectors, Pixel detectors, SCT detectors (Si microstrips), and TRT detectors (transition radiation tracker). The ID detectors have a coverage region of $|\eta| < 2.5$. Figures 3.6 and 3.7 show schematically the ID detectors in both the barrel and endcap.

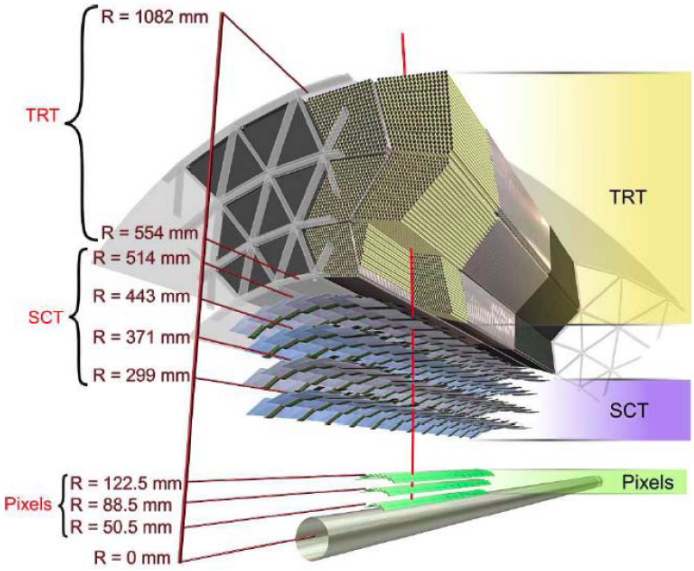

Figure 3.6: A cross sectional view of the barrel ID components.

The Pixel detectors are optimized for high resolution position measurements close to the beamline and consist of 3 layers in both the endcap and barrel. The pixels themselves are around 50 μm $\times$ 400 μm in size and the entire pixel system consists of 80.4 million readout channels. The SCT detectors consists of 4 layers in the barrel and 9 layers in the endcap. The SCT detectors are strip detectors with a pitch (strip width) of 80 μm. Each SCT layer has two semiconductor planes with strips placed at a 40 mrad angle to allow the measurement of the second coordinate. In total, the

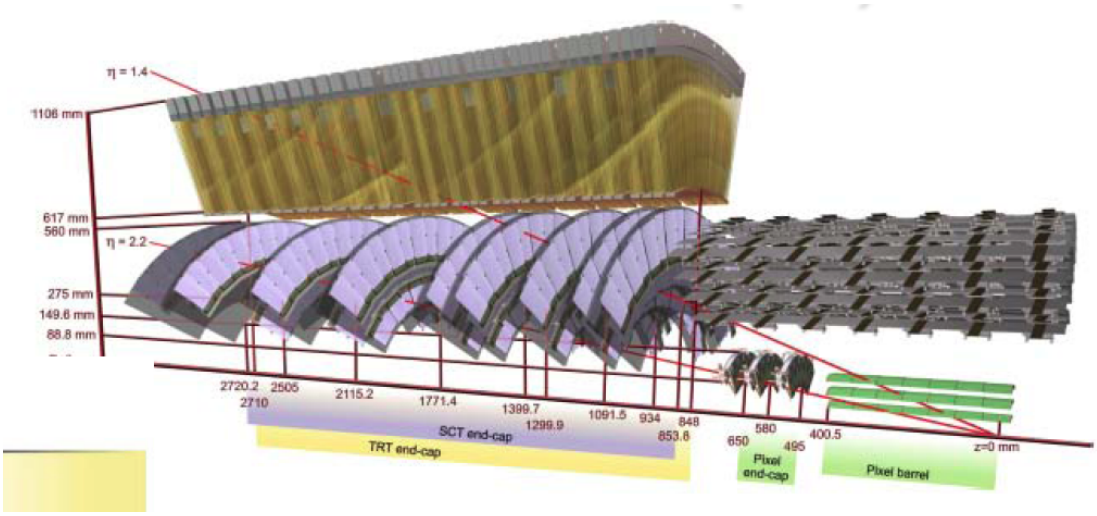

Figure 3.7: A cross sectional view of the endcap ID components.

SCT detectors have 6.3 million readout channels. Both Pixel and SCT detectors have readouts faster than 25 ns (the LHC bunch interval) so it is possible to differentiate hits from different bunch crossings.

Both Pixel and SCT detectors are silicon based detectors. These type of detectors consist of a bulk material that is made of a N-type Si semiconductor wafer. The operating principle of silicon based detectors is shown below in Figure 3.8.

When a charged particle passes through, the electrons from ionization drift to the n+ (positive charge carrier) as shown in Figure 3.8. As this detector can be miniaturized, this allows for a huge resolution improvement over previous detectors such as spark, cloud, bubble, or wire chambers. The downside is that Si detectors are much more expensive, need complex cooling, and are also more susceptible to radiation damage. They are also quite sensitive to B fields and thus require us to have precision B field measurement in the detector. This same susceptibility to B

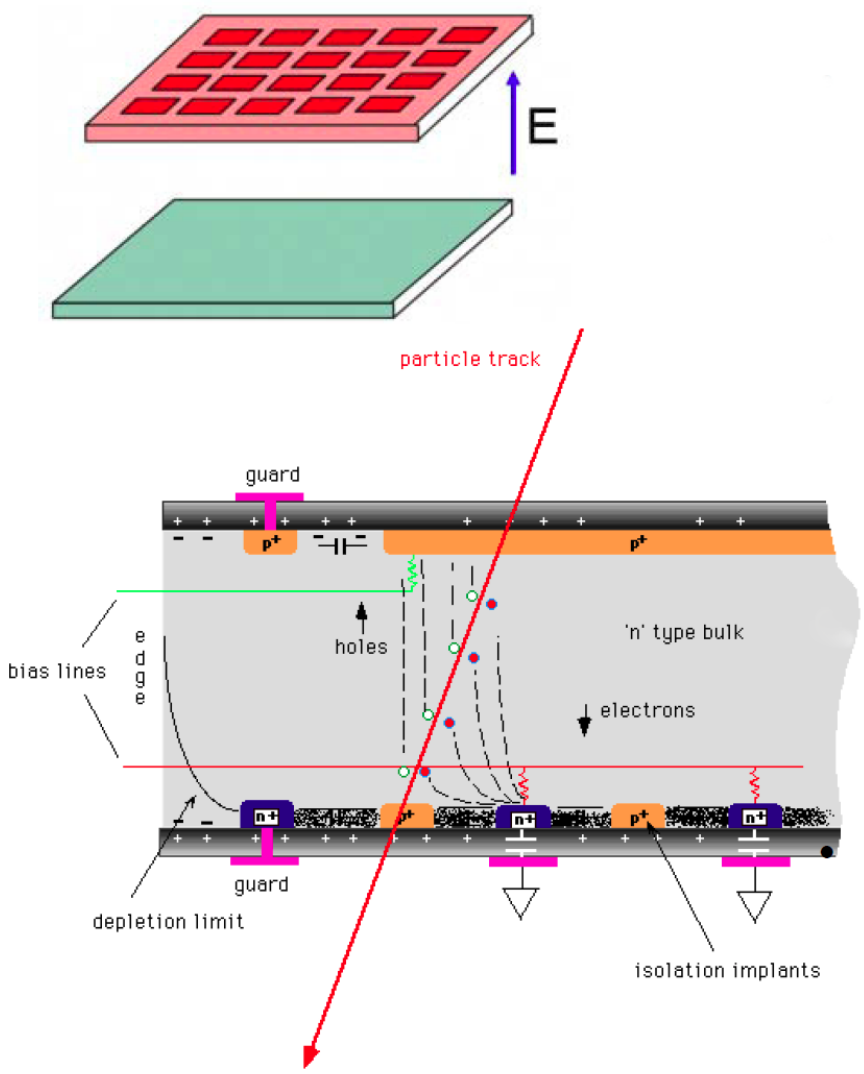

Figure 3.8: Silicon detector operating principles [5].

field also exists for the gaseous detectors discussed later since they also have ionized particles that drift. Figure 3.9 shows how a B field can impact the drift of ionized particles and lead to mis-construction of the incident particle path.

The third type of detector in the ID is the TRT. The TRT is a gaseous detector that consists of many tubes arrayed parallel to the beamline in the barrel and radially

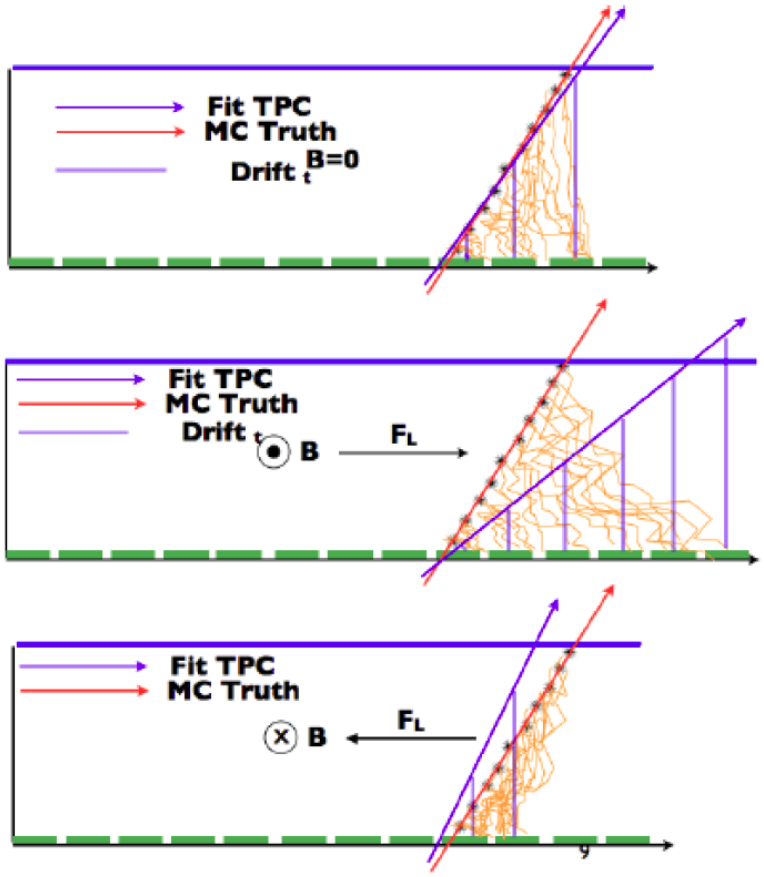

Figure 3.9: Ionized particle drift in varying B fields in a generic gaseous detector with readout strips. Different B fields can result in different fitted incident particle path [32].

in the endcap. Because of the number of tubes, the TRT makes a large number of measurements per track and is important for the track fits which help to establish charged particle momentum. The TRT also takes advantage of the transition radiation that is emitted when a charged particle goes through the boundary of two regions with different dieletric constants. This radiation causes ionization in the gas volume and the resulting cascade produces an ionization that is proportional to the amount

of energy lost in the transition radiation. The dE/dx (energy lost over distance travelled) measurement can be used for better particle identification. The TRT detector has 351,000 readout channels and a readout time of around 50 ns which is largely set by the time it takes ionization electrons to drift to the readout anode.

As gaseous detectors are also used in the ATLAS muon detectors (both existing and the upgraded detectors discussed in Chapter 4), we will quickly describe their operating principles here. Figure 3.10 below shows how gaseous tube detectors work.

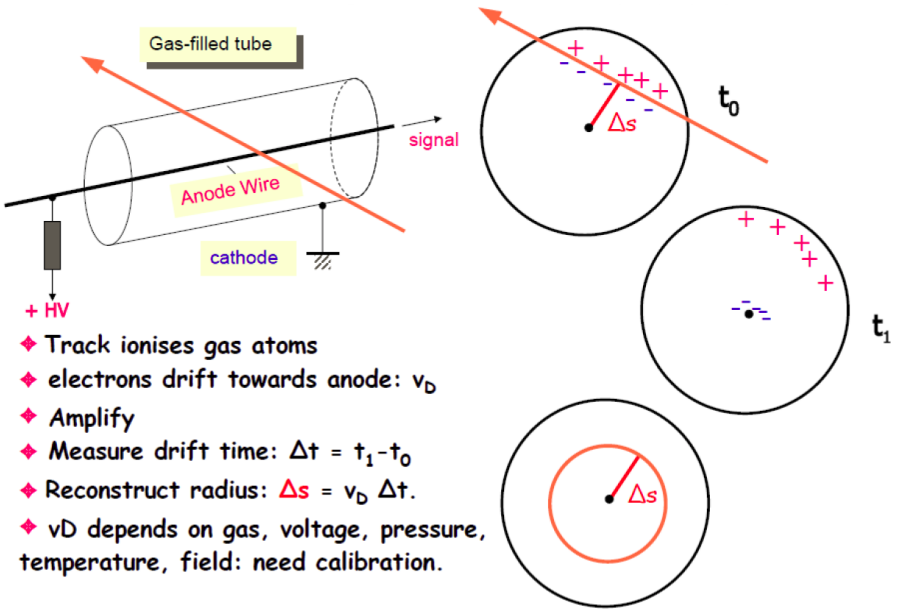

Figure 3.10: Operating principles of a gaseous drift tube detector [53].

After a charged particle track ionizes gas atoms, the electrons drift towards the anode wire. As they approach the anode, the field increases which causes an electron avalanche which amplifies the signal. By measuring the drift time, it is possible to reconstruct the radius at which the charged particle passed through the drift tube.

The choice of gas used in the drift volume is actually fairly important as it impacts the drift velocity.

A slower drift velocity typically allows for higher position resolution, but in a high rate environment, a faster gas is better. The gas mixture used is typically a combination of an active gas and a "quencher" gas. For the TRT detector, the combination used is 70% Xenon, 27% CO_2, and 3% O_2. The active gas is usually a noble gas (typically Argon because it is cheaper than Xenon) because their electrons are easier to ionize. As a result, you can get good amplification at lower voltages and also have a smaller energy loss with each ionization. The quencher gas is typically some complex molecule, popular choices are CH_4, CO_2, or CF_4 which contain rotational and vibrational modes which are good at absorbing UV photons. In ATLAS, CO_2 is typically used because it is demonstrated to be better in a high radiation environment.

3.2.3 Electromagnetic Calorimeter

The purpose of the ATLAS electromagnetic calorimeter (ECAL) is to measure the energy of electrons and photons. When passing through matter, photons will undergo pair-production and produce an electron and positron pair. Electrons (and pair-production products) will undergo a process called bremsstrahlung in which the electron interacts with the electric field of an atom and emits photons (which can also undergo pair-production). Through this cycle, both photons and electrons will produce an electromagnetic shower and this energy is then deposited in the ECAL and measured. In the ATLAS detector, the ECAL sits right outside the solenoid, which sits right outside the inner detector. Figure 3.11 is a cutaway view of a chunk

of the ATLAS ECAL.

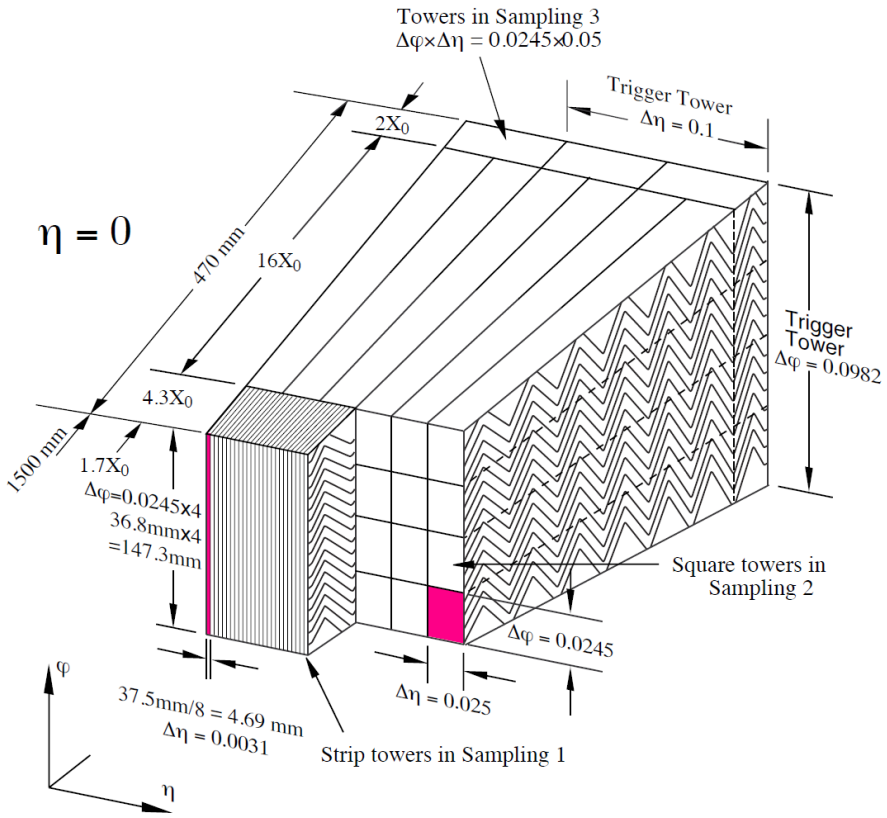

Figure 3.11: Cutaway view of the ATLAS ECAL showing the unique accordion geometry [21].

The ATLAS ECAL is made up of lead and liquid argon (LAr) and extends until $|\eta| < 3.2$. The LAr is the active medium where the signal is read out. LAr is very radiation hard, but it has a long readout time. The lead helps to make sure the ECAL will capture all of the energy from electromagnetic particles and reduce the amount of "punch through" to the hadron calorimeters.

The ECAL has an accordion geometry which provides a large acceptance and uniform response over the full azimuthal range without any gaps. Situated at the very

front of the ECAL, is a region called the presampler which is very finely segmented in η. This allows for a good determination of the shower shape at the entry point of the ECAL and helps with estimating how much showering has occurred before the particle got to the ECAL. This is particularly important for ATLAS, because unlike CMS, the solenoid is positioned in front of the ECAL, and the additional material makes it more likely for some showering to occur before the ECAL is reached.

3.2.4 Hadronic Calorimeter

Right outside the ECAL are the hadronic calorimeters which are designed to measure energy deposition by hadrons. ATLAS uses two different types of detectors for the hadron calorimeter. In the barrel region, the HCAL consists of scintillating tiles alternating with iron. The HCAL endcap is a LAr detector like the ECAL. This, combined with the LAr forward calorimeters gives coverage up to $|\eta| < 4.9$. Figure 3.12 is a cutaway view of a slice of the barrel HCAL.

Like the ECAL, the HCAL is a sampling calorimeter, and in the tile calorimeter, the steel sections act as an absorber to cause showering. The scintillating tiles are made of polystyrene (plastic) and the signal is sent via fiber to a photomultiplier readout. The ratio of steel to scintillator is 4.7:1 by volume.

3.2.5 Muon Spectrometer

ATLAS contains a comprehensive muon spectrometer which allows for precision measurements of muons. These detectors are located at the very outside of the detector as muons tend to pass through all detectors without stopping or interacting.

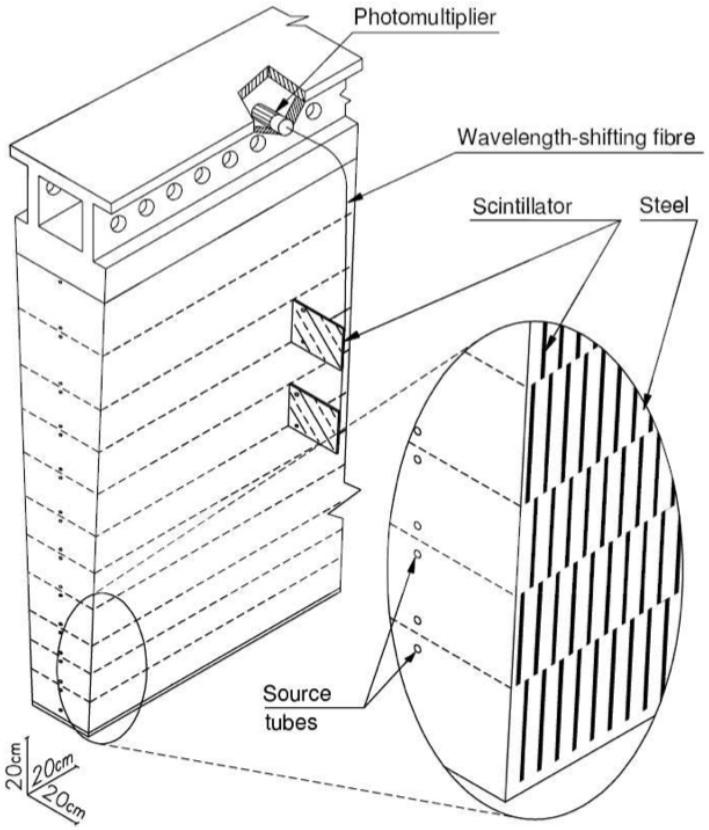

Figure 3.12: Cutaway view of the ATLAS tile HCAL showing the alternating layers of scintillator and steel [21].

The toroid magnets are located around the muon spectrometers because the only way to measure the muon momentum is by measuring the curvature of the muon track in a B field. A stronger field leads to more curvature which improves the momentum measurement.

ATLAS uses four different technologies in the muon systems. Two types of precision measurement detectors are used, the gaseous Muon Drift Tubes (MDT) and the Cathode Strip Chambers (CSC). However, the MDTs have limited rate ability because of the slow gas drift time so they are not the best detectors for triggering. Thus, the

ATLAS muon systems also use two types of gaseous detectors, the Resistive Plate Chambers (RPC) and the Thin Gap Chambers (TGC) for triggering in the barrel and endcap respectively. Figure 3.13 shows the location of most of the muon spectrometer detectors.

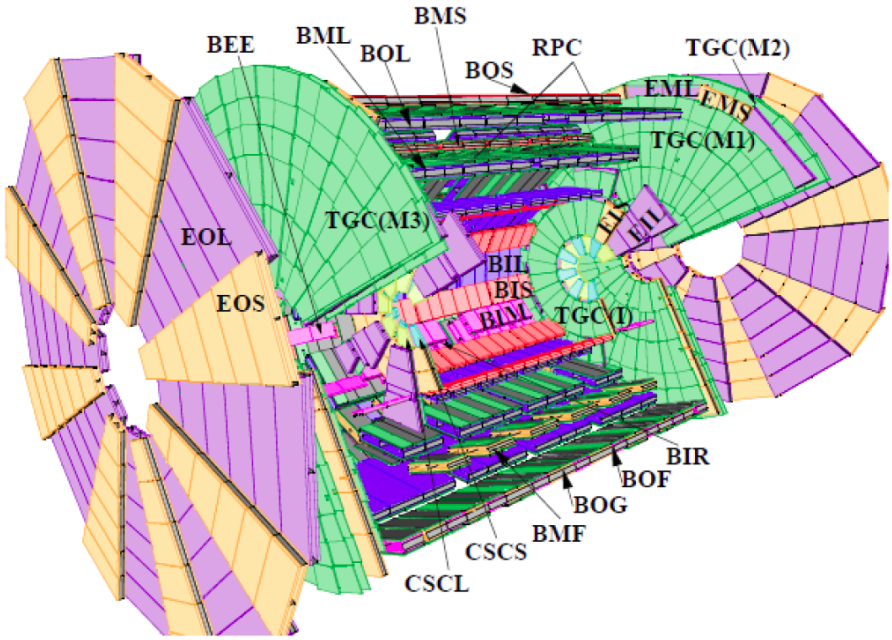

Figure 3.13: Cutaway view of ATLAS showing the various detectors which compose the muon spectrometer. The detectors are arrayed in three distinct sections: one barrel and two endcaps. The barrel chambers are composed of MDT chambers (indicated in the figure as BIS, BMS, BOS, BIL, BML, BOL, BMF, BOG, BOF, BIR) and RPC chambers. The Small Wheel (TGC(1), CSCS, CSCL, EIS, EIL), Big Wheel (TGC(M1), TGC(M2), TGC(M3), EMS, EML) and Outer Wheel (EOL, EOS) are composed of TGC, CSC and MDT chambers.

The detectors are arrayed in three distinct sections. The barrel section is composed of MDT and RPC detectors forming cylinders around the beam axis. The two endcap sections cover the higher rapidity region with the Small Wheel (closest to the interaction point), the Big Wheel and the Outer Wheel. The Big Wheel provides

the trigger information and it is composed of MDT and TGC chambers. The Small Wheel is composed of CSC, TGC and MDT chambers, while the Outer Wheel only has MDT chambers.

Muon Drift Tubes

The MDTs are gaseous wire chambers similar in operating principle to the TRTs described previously. The ATLAS MDTs use a gas mixture of 93% Argon and 7% CO_2. The tubes have a diameter of around 30 mm with a central wire held at an operating voltage of 3080 V. The MDTs have a maximum drift time of ≈700 ns. MDT tubes are arranged into chambers. Each chamber consists of two multi-layers and each multi-layer has 3 or 4 layers of tubes. In total, ATLAS contains 370,000 MDT tubes which are arranged in 1194 chambers.

Cathode Strip Chambers

In the very forward region of the muon spectrometer, the MDTs are replaced with CSCs (in the region $2.0< |\eta| <)2.7$. The CSCs are used in the very forward region because they are capable of handling the higher rates which occur in the forward regions. Figure 3.14 gives a schematic view of the CSCs.

The CSCs are also gaseous detectors, and like the TGCs, they fall into a category of detectors known as multiwire proportional chambers. Charged particles ionize the gas and electrons drift to the cathode readout strips. CSCs have one step of strips which run perpendicular to the anode wires while another one runs parallel to the wires. The anode operates at 1900 V and the gas mixture is 80% Argon and 20% CO_2. Strip pitch is around 1.5 mm and the typical drift time is less than 40 ns which

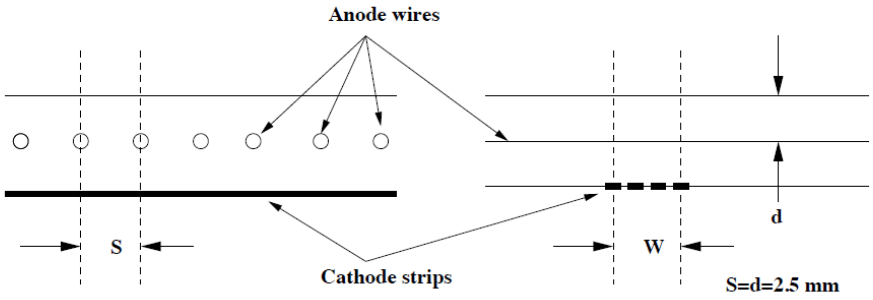

Figure 3.14: Schematic of an ATLAS CSC detector [21].

makes the CSCs suited for the high rate forward regions.

Resistive Plate Chambers

The RPCs are also a gaseous detector and is used for triggering in the barrel region. A cross section of the RPC detectors used in ATLAS is shown below in Figure 3.15.

An RPC detector consists of two layers, each with a gas volume. Each layer has two parallel resistive plates which are operated at a very high voltage of 9.8 kV. Due to the high voltage, the RPCs operate in avalanche mode. On each side of the gas gap, there are readout strips which are orthogonal to each other making it possible to measure both the η and ϕ coordinate. Because the RPCs operate in avalanche mode, they have very good time resolution. As it only takes 10 ns to get a signal, RPCs are well suited in their role as triggering chambers.

Thin Gap Chambers

Similar to CSCs, TGCs are also gaseous multiwire proportional chambers. Like the RPCs, they are used for muon triggering. A cross section of the TGC detectors

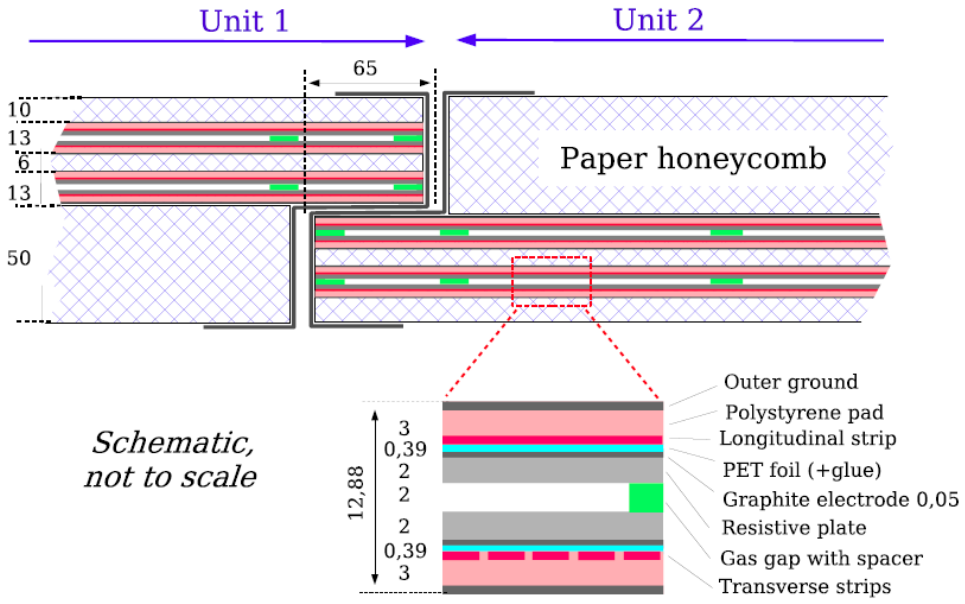

Figure 3.15: Schematic of an ATLAS RPC detector [21].

used in ATLAS is shown below in Figure 3.16.

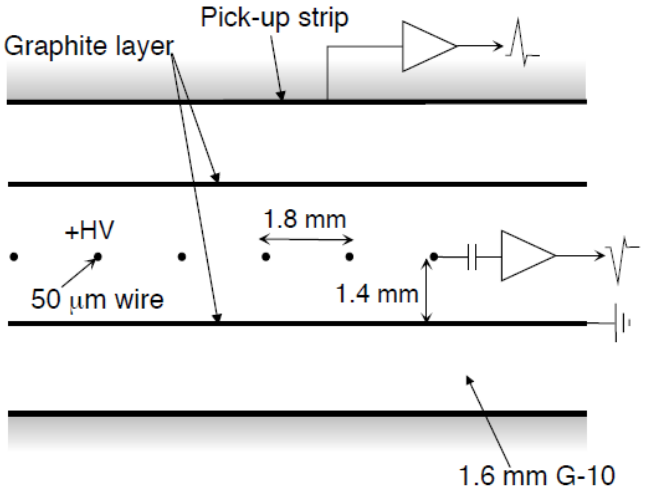

Figure 3.16: Schematic of an ATLAS TGC detector [21].

The readout strips are located at the top of the detector and are perpendicular to the anode wires. The distance between the anode wire is 1.8 mm while the distance from the wire plane to the cathode is 1.4 mm. The detector operates at a voltage of 2900 V using a gas mixture that is 55% CO_2 and 45% n-pentane and is capable of a 25 ns time resolution.

As we will discuss in the next chapter, the performance of the current ATLAS muon systems is not sufficient for running at the future High Luminosity LHC. To address these issues, the Small Wheel detector will be upgraded during the 2018 long shutdown. The TGCs are one of the technologies that will continue to be utilized in the New Small Wheel detector, while the MDTs and CSCs are being replaced. The modifications made to the TGC detectors for the New Small Wheel detector will be discussed in the next Chapter.

Chapter 4

The ATLAS New Small Wheel Detector

To better achieve the future physics goals of the LHC (such as searches for SUSY or other sorts of new physics involving heavy particles which have not yet been discovered), the current collider will be upgraded to the High Luminosity LHC. This upgrade will proceed in several steps. In the current run which began in 2015, luminosity is expected to reach the nominal value of $1 \times 10^{34}\,\mathrm{cm}^{-2}\mathrm{s}^{-1}$ at 13 TeV. This will be followed by a second long shutdown starting in 2018 where the luminosity will be increased to $2 - 3 \times 10^{34}\,\mathrm{cm}^{-2}\mathrm{s}^{-1}$. During subsequent shutdowns, the objective is to ramp the luminosity up to $5 \times 10^{34}\,\mathrm{cm}^{-2}\mathrm{s}^{-1}$ with the overall physics goal of collecting 3000 fb^{-1} of integrated luminosity over the next decade.

As an aside, it is interesting to note that the accelerator is actually capable of producing an instantaneous luminosity of $10^{35}\,\mathrm{cm}^{-2}\mathrm{s}^{-1}$, but this is beyond what the

detectors will be able to handle. The CERN Accelerator Division is presently working on something called a "crab crossing" which creates an angle that the beams cross when they collide. When the beam is first injected, it actually has an instantaneous luminosity that exceeds $5 \times 10^{34}, \text{cm}^{-2}\text{s}^{-1}$, but a wider angle is used to bring the luminosity down to that level. As the beam decays and the number of protons decreases, this angle is adjusted so that the instantaneous luminosity actually stays constant. This way, the integrated luminosity that is collected can be maximized by always running the collider at the maximum instantaneous luminosity that the detectors can handle.

In preparation for this ramp up in luminosity, components of the ATLAS detector will need to be improved if we want to maintain the performance that we have at lower luminosities. As discussed in the previous chapter, the Small Wheel muon detectors will need to be upgraded in order to ensure that ATLAS can continue to effectively search for new physics such as SUSY.

4.1 Upgrade Motivations

The proposed upgrade to the Small Wheel detector is known as the New Small Wheel, or NSW. The objective of the NSW is to address two primary issues. The first is the degradation of the performance of muon tracking chambers in the endcap region when there is an increase in the cavern background rate. Simulations extrapolating the cavern background rate out to the high luminosity LHC show a substantial degradation in both the efficiency and resolution of muon reconstruction.

The second issue is the Level 1 (L1) muon trigger rate in the endcap region. The L1 rate will increase proportionally with the instantaneous luminosity and at the higher luminosity LHC, it will exceed the limit on the total L1 rate. This issue is particularly acute in the endcap regions because of the high incident of fake triggers produced by low energy particles (primarily protons) which are generated in the material in front of the Small Wheel and hit the endcap trigger chambers at an angle that resembles real high P_T muons. In the 2012 data, it was found that approximately 90% of the muon triggers in the endcaps are fake [23]. Figure 4.1 shows the layout of the current ATLAS muon spectrometers and the location of the small wheel detector.

The trigger rate issue is made worse by the fact that in the present muon spectrometer, only the Big Wheel detector participates in the triggering. Without additional trigger hit information from the Small Wheel, it is difficult to map trigger hits on the Big Wheel back to particles originating from the interaction point. As a result, we have poor rejection of fake triggers. In hindsight, this is a design flaw of the current ATLAS detector and adding triggering capabilities to the NSW will provide a second hit position measurement which can be used to eliminate fakes.

Without a better small wheel detector, the only option to resolve the L1 muon trigger rate is to either increase the P_T thresholds or to prescale the trigger. Neither are good alternatives because it will lead to many physics events being lost and hurt the sensitivity of searches such as the one described in Chapter 6. To solve this problem, the current Small Wheel detector must be replaced with the NSW which will have higher precision tracking and trigger detectors which are capable of

working at higher rates while also providing improved spatial and time resolution. This will provide the angular resolution needed to enable the L1 trigger system to more accurately confirm that muon candidates actually originate from the IP and thus reduce the fake rate.

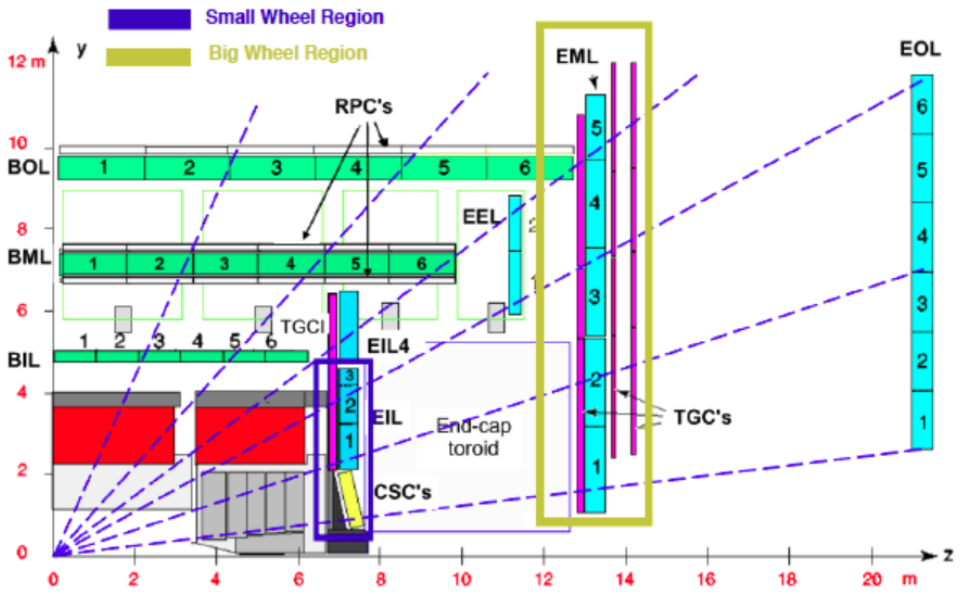

Figure 4.1: Cutaway view of the ATLAS detector in the z-y plane showing the position and composition of the current small wheel detector (in the blue box).

4.2 Requirements

The NSW should be able to handle luminosities up to the eventual target of $5 \times 10^{34}\,\mathrm{cm}^{-2}\mathrm{s}^{-1}$. By taking advantage of the proportionality between the hit rates and the luminosity, it is possible to extrapolate the hit rate out to $5 \times 10^{34}\,\mathrm{cm}^{-2}\mathrm{s}^{-1}$. These estimates are given below in Table 4.1.

We also need to account for the fact that the beam energy will be roughly dou-

Region	Hit Rate (Hz/cm^2)
CSC	7000
EIL1	3600
EIL2	1100

Table 4.1: Estimated hit rates at $5 \times 10^{34}\,\mathrm{cm}^{-2}\mathrm{s}^{-1}$ for various sections of the small wheel region. The regions are shown graphically in Figure 4.1.

bled (the rate increase is expected to be approximately 1.6 [23]) but the beam pipe will also be replaced with a lighter one which will decrease the cavern background (rate decrease of 1.2-1.3), thus to be safe, we apply a safety factor of 2 for our rate predictions, and take 15 kHz/cm^2 to be the maximum expected rate at $\sqrt{s}$=14 TeV.

In terms of detector ageing, the NSW is expected to be in operation for the full 3000 fb^{-1} expected to be collected at the LHC over the next decade. As an order of magnitude calculation, we can assume the detector will be operating for 10^8 seconds so the total number of hits in the hottest region will be at most 10^{12}/cm^2. If we assume 100 electrons are ionized per hit with a 10^4 amplification factor, the total collected charge would be 0.2 Coulomb/cm^2 so the detectors will need to be able to withstand this ageing effect or be designed in such a way that the most forward chambers can be replaced easily in subsequent shutdowns.

In order to have performance as good as the current Small Wheel detector did at lower luminosities, the NSW will need to be able to measure the P_T of muons with 10% precision for 1 TeV muons in the full η coverage of the current Small Wheel. In order to accomplish this, the NSW will need to have the following performance characteristics (which largely match the current MDT system):

- Reconstruct track segments with a position resolution in the bending plane better than 50 μm. This requires a segment position resolution result that is better than 100 μm per detector plane.
- Segment finding efficiencies better than 97% for muons with $P_T > 10$ GeV.
- Measure the second coordinate with a resolution of 1-2 mm in order to allow for good MS and ID track matching.

The NSW will also need to keep the Level-1 trigger rate for muons with $P_T > 20$ GeV to around 20 kHz. In order to accomplish this, the NSW requires the additional performance criteria:

- Track segment information should arrive at the muon trigger logic no later than 1 μs after the collision.
- Track segment reconstruction used for triggering should have an angular resolution better than 1 mrad RMS.
- Track segments need to have a granularity better than 0.04×0.04 in the $\eta - \phi$ plane.
- Online track segment reconstruction efficiency needs to exceed 95%.

4.3 Detector Technology and Layout

At the time I joined the NSW project in September 2011, the project was still in the planning phases and the choice of detector technologies and detector layout

had not been made yet. In addition to developing the simulation framework for NSW, I was part of the NSW Layout and Mechanics Working Group and responsible for implementing successive detector geometries as the final proposed layout was developed over the course of a year. In this section, a summary of the detector technologies selected is first presented, followed by a discussion of the layout work.

4.3.1 sTGC Detectors

The first new detector type used in the NSW are the sTGC detectors which are more advanced versions of the TGC detectors currently installed in the ATLAS muon systems and discussed previous in more detail in Chapter 3. Compared with the existing TGC detectors, the sTGC detectors have undergone a number of modifications for better performance in a high luminosity environment. This includes reducing the distance between the readout strips and the graphite layer (which improves the rate capability by allowing a muon to be read out faster), the addition of pad triggers (which reduce the number of strips which need to be considered for the L1 trigger), reducing the surface resistivity of the graphite layer, and decreasing the size of the readout strip pitch (in order to provide improved spatial resolution). A schematic of a NSW sTGC detector is shown below in Figure 4.2.

The sTGCs utilize an operating gas that is 55% CO_2 and 45% N-pentane with 2.7 mm readout strips and a pitch size of 3.2 mm. The wires are separated by 1.8 mm and are sandwiched with a separation of 1.4 mm from the cathode planes. The operating voltage of the chamber is 2.9 kV. The high voltage, combined with the small gas gap work together to ensure that the drift time for electrons is under 25

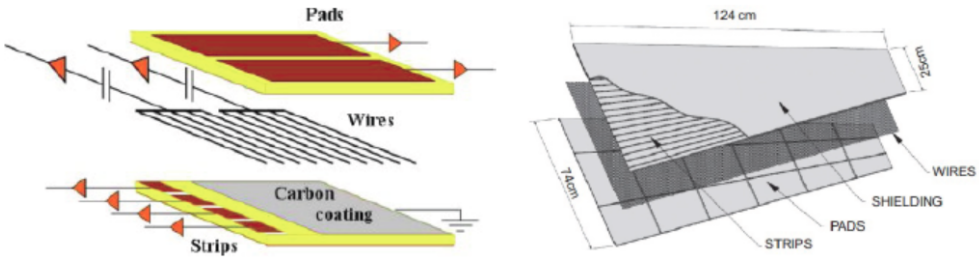

Figure 4.2: The New Small Wheel sTGC internal structure [23].

ns which gives us the rate performance that is required. The small pitch size for the strips also ensures that a per layer position resolution ranging from 60 μm to 150 μm can be achieved which is also sufficient to reach the resolution targets.

4.3.2 Micromegas Detectors

The second new detector type used in the NSW are Micromegas, which is short for MICRO-Mesh-GAseous-Structure, and will be sometimes abbreviated here as MM. Unlikely the sTGCs, Micromega detectors are an entirely new type of detector which has not been previously used at ATLAS. Micromegas are made up of a planar electrode, and a thin gas gap with a thin metallic mesh very close to the readout electrode. The metallic mesh divides the gas gap into two regions, a drift volume (where primary ionization occurs) and an amplification volume (where the amplification of primary ionizations occurs). A diagram showing the operating principles of MM detectors is shown below in Figure 4.3.

Charged particles traversing the drift space ionize the gas and the electrons liberated by the ionization process drift towards the mesh. The high voltage (HV)

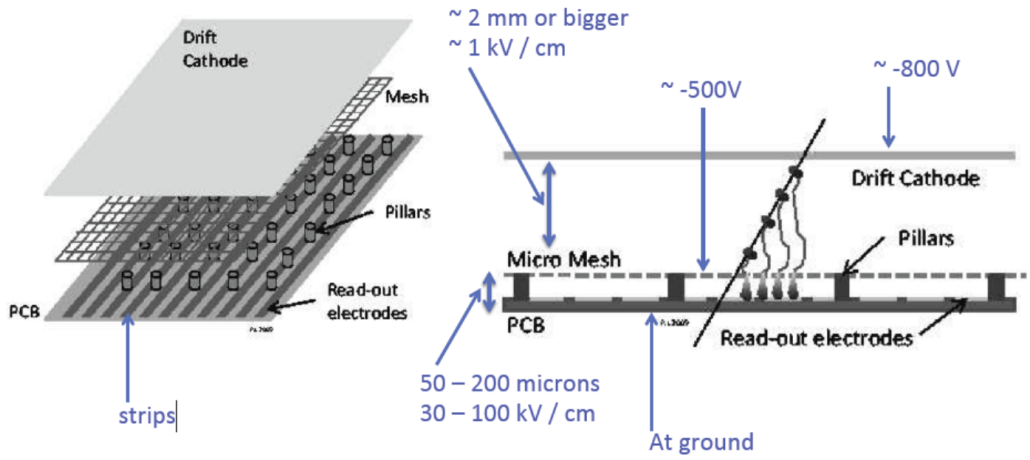

Figure 4.3: The New Small Wheel MicroMegas internal structure.

potentials are picked so that the electric field in the drift region is on the order of 1 kV/cm and increases to 30-100 kV/cm in the amplification region. The electron avalanche thus occurs in the thin amplification region immediately above the readout electrode.

The MM technology design exhibits several advantages. First the small size of the amplification region means that a lower HV can be used to give us a high electric field. Secondly, while the drifting of electrons in the drift volume is not any faster than in other gaseous detector designs, the amplification process is very rapid resulting in a fast pulse of electrons on the readout strip which gives a fast signal and good timing resolution. Finally, the positive ions produced in the avalanche drift in the opposite direction as the electrons and go back to the amplification mesh. In MicroMegas, this re-absorption of ions occurs much more rapidly which makes the technology capable of dealing with much higher rates.

The disadvantage of MicroMegas is that the very thin amplification region is susceptible to sparking which can occur when the total number of electrons in an avalanche reaches around 10^7 [58]. The NSW MM detectors are designed with a spark protection system that adds a layer of resistive strips on top of a thin insulator directly above the readout electrode. This makes the readout electrode no longer directly exposed to the charge created in the amplification region, instead the signals are capacitively coupled to it [23].

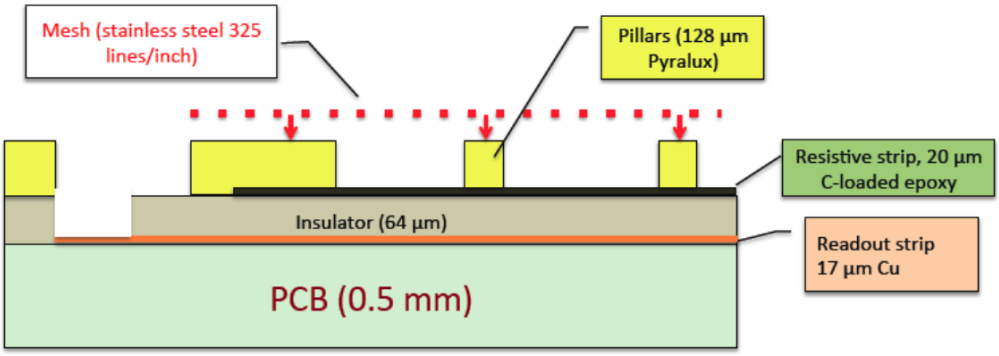

Figure 4.4: The New Small Wheel MicroMegas readout internal structure.

The proposed MM detectors for the NSW will use a gas that is 93% Ar and 7% CO_2 with a readout strip pitch of 0.425-0.445 mm which will allow for sufficiently high position coordinate precision. The amplification gap will be 128 μm with a 5 mm drift region which will yield an amplification and drift field of 40 kV/cm and 600 V/cm respectively.

4.3.3 Layout

Starting in Spring 2012, the NSW Layout and Mechanics Working Group was formed to determine the optimal layout for the NSW. At a high level, the constraints are set by the existing Small Wheel detector, it is required that the NSW be able to fit into the existing space occupied by the Small Wheel detector and furthermore have the same η coverage as the existing Small Wheel detector. Work was also done to ensure that the total weight, including the mechanical support structure does not become excessive. The layout shown here is the latest as of Fall 2012, and does not reflect some updates which have been made since that time.

Multiple detector proposals were evaluated, including an all MicroMega proposal and proposals with Small MDT detectors. At the end, it was decided to use a combination of sTGC and MM detectors for the NSW. Within the geometric constraints, it was possible to fit in 16 detector planes in two multilayers. Each multi-layer is composed of 8 detector layers, 4 sTGC and 4 MM. The multi-layers are arranged so that from small to large z, the detectors are arranged as sTGC - MM - MM - sTGC. Since the sTGCs are the primary trigger detectors, maximizing the distance between the sTGCs will lead to improved online track segment angle reconstruction. Figure 4.5 shows a cross sectional view of the NSW [54].

The layout of the entire NSW detector is very similar to the current Small Wheel with detector modules arrayed radially and going out in the r direction. Figure 4.6 shows how the detector modules are arrayed when fully assembled [54].

For all simulation work on the NSW, it is necessary to define a common and

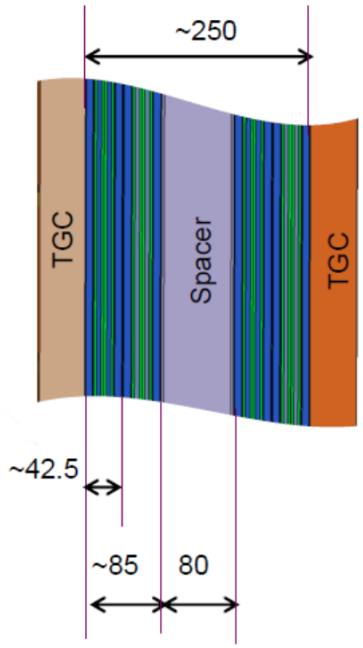

Figure 4.5: A cross sectional view of the 2012 NSW in the z-axis showing the sTGC - MM - MM - sTGC layout [54].

consistent naming scheme. To assist with this, the following identification scheme is used on the chamber level. First chambers are separated based on whether they are on the A or C side of the ATLAS detector. Then there are a set of 5 additional identifiers that look like the following:

`[M/T] [0-3] [L/S] [P/C] [0-3]`

These have the following meaning:

- **[M/T]** - This indicates whether the chamber is a MM (M) or sTGC (T).
- **[0-3]** - The first integer can run from 0 through 3 and it specifies the module in the r direction where 0 is the chamber closest to the beamline (the red chamber in Figure 4.7).

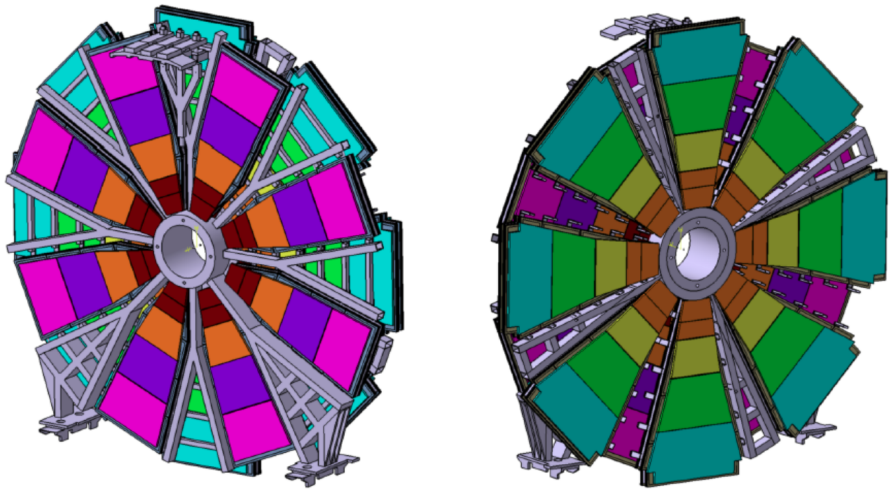

Figure 4.6: The detector module layout of the NSW. This diagram was produced in mid-2012 before all support structures are finalized but it nevertheless well represents the layout of the detector modules [54]. The inner most detector in red is actually one detector, the dividing line is to show the extent of the staircase geometry discussed at the end of this section.

- **[L/S]** - This specifies whether the chamber is in a large or small sector, the small sectors are the ones that are visible to the left of Figure 4.6 while the large sectors are the ones visible in the right diagram of Figure 4.6.

- **[P/C]** - This specifies which side of the sector the chamber is on (either facing the interaction point or facing the tunnel).

- **[0-3]** - This specifies the specific chamber number in each sTGC and MM quadruplet, with 0 being the chamber with the smallest z-axis value (e.g. closest in position to z=0).

We define modules to be an assembly of sTGC and MM quadruplets at the same r axis value. As we can see from Figure 4.7, the use of separate modules means that there will necessarily be gap regions between modules. For the higher η regions,

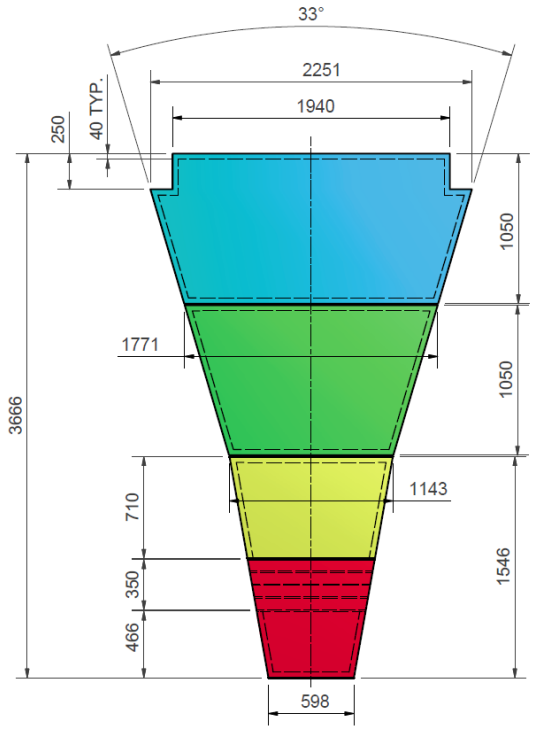

Figure 4.7: A single sector of the 2012 NSW where a sector is defined as 1/16 of the NSW on either side A or C comprised of sTGC and MM wedges [52].

the impact of this is less pronounced as particles will be impacting the detectors at larger angle of incidence so even if they pass initially through the gap region, they are likely to strike a chamber on the way out. However, this is not the case closer to the beamline so the sTGC geometry is modified between module 0 and 1.

As we see in Figure 4.8, the sTGC chambers are staggered in a staircase geometry so that a particle passing through the detector will not encounter a dead zone where there's no possibility of registering hits. This allows for nearly complete recover of the efficiency.

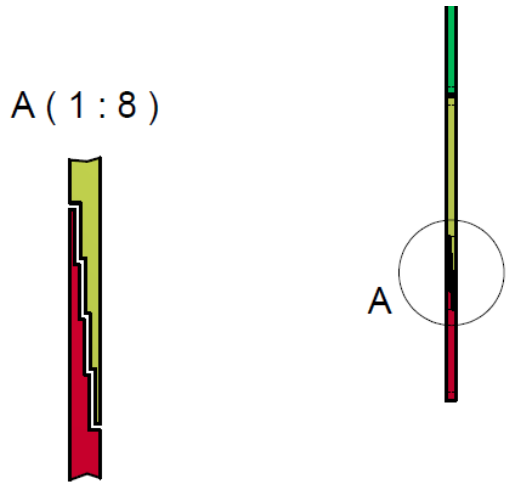

Figure 4.8: A close up view of the sTGC chambers between module 0 and 1. The sTGCs are arrayed in an overlapping staircase geometry so that no detector gaps are present [52].

As the NSW detector is not planned to be installed until 2018-2019, the layout here is still very much a work in progress and could vary significantly from the final design that is eventually built and installed in ATLAS.

4.4 Detector Simulation

A full detector simulation is required in order to get a realistic idea about the expected performance of the proposed New Small Wheel. The two technologies selected for the NSW, Micromegas and sTGCs are significantly different from existing small wheel technologies so existing detector descriptions cannot be easily adapted. Furthermore, most of the current muon simulation software was developed approximately 15 years ago and without the benefit of hindsight, it was not designed in a way that can readily adapt to new detector technologies. Thus, it is necessary to come up with

a new framework for carrying out NSW simulations.

On the other hand, to avoid un-necessarily reinventing the wheel, an overarching design objective is to maintain compatibility with the Athena software framework so that improvements made through Athena are automatically passed onto the NSW simulation, and a better comparison can be made with the existing small wheel detector. Figure 4.9 below shows the various steps that are required to fully simulate the NSW detector and produce samples which can be used for performance studies.

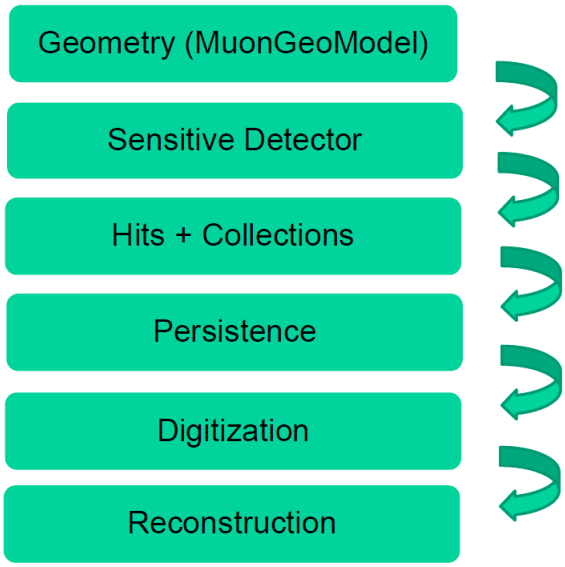

Figure 4.9: An overview of the different stages for simulating the NSW detector. These steps are similar to the existing workflow for Small Wheel simulation, but many of these steps need to be modified and extensively customized to suit the different NSW simulation requirements.

4.4.1 Modelization of NSW Geometry

One of the main requirements for the NSW geometry is that it be easy to modify because simulation will play a role in determining the optimal layout. A large degree

of flexibility is also required because the NSW layout is expected to change frequently and the objective is to have some sort of simulation available even if the layout is not finalized. The need to be able to change the geometry frequently and without too much effort means the Oracle database system (AMDB) currently used to store the geometry in the existing small wheel simulation cannot be used.

The current geometry description for the Small Wheel detector is frozen in AMDB (which knows nothing about MM or sTGC) and then translated into Oracle tables, from which the MuonGeoModel representation is built. This system is far from ideal for a simulation that requires frequent layout changes as the layout group iterates. The alternative we developed for the NSW instead uses the XML markup language that is currently used for the dead material geometry. This allows the entire geometry to be encapsulated into a single XML file which can be easily swapped out to switch between geometries. The NSW chamber dimensions are encoded in plain text in the XML file and can be easily changed as well.

```
<micromegas type="sMD1-1-1" tech="MM_1" subType="M0LP0"
sWidth="NSW_MM_FrontDisk_baseWidth" lWidth="NSW_MM_FrontDisk_layer2Width"
Tck="NSW_MM_DiskThickness" Length="NSW_MM_FrontDisk_standardPlateLength" />
```

Figure 4.10: An example code XML code snippet showing how an individual MM chamber is represented in XML scheme for describing the NSW geometry.

In Figure 4.10 above, an example XML code snippet is shown. Shown in bold is also the unique chamber identifier which uses the naming convention that was developed and described in the previous section. To support the XML description of the NSW geometry, the MuonGeoModel (MGM) software package in Athena was extensively modified. First, the ability to disable existing chambers and stations

was added. This allows the existing small wheel chambers to be removed from the geometry. The following Small Wheel chambers were removed from the geometry:

- **MDT** - EIS1, EIS2, EIL1, EIL2, EIL3
- **CSC** - CSL, CSS
- **TGC** - T4F

Next, MGM was modified to handle the new shapes required for the proposed NSW geometry. Notably, the 2012 layout includes a hexagonal micromega and square cutouts for the outermost sTGC and MM chambers. As shown in Figure 4.11, the new version of MGM for NSW simulation can now understand custom XML tags which allow for two different types of "corner cutting", thus allowing for a wide range of chamber shapes to be implemented. Furthermore, the new MGM is also able to build the staircase geometry between the first two sTGC modules. This rather complicated geometry can now be implemented with a single line of XML code.

Using this method, the entire NSW layout with both MM and sTGC has been implemented via the XML description. This layout is accurate down to the chamber level and uses the exact dimensions from the latest NSW engineering diagrams. The complete NSW geometry as visualized in the VP1 software is shown in Figure 4.12. Due to the flexible design of the XML system, this geometry can be easily modified and updated as new iterations of the layout become available.

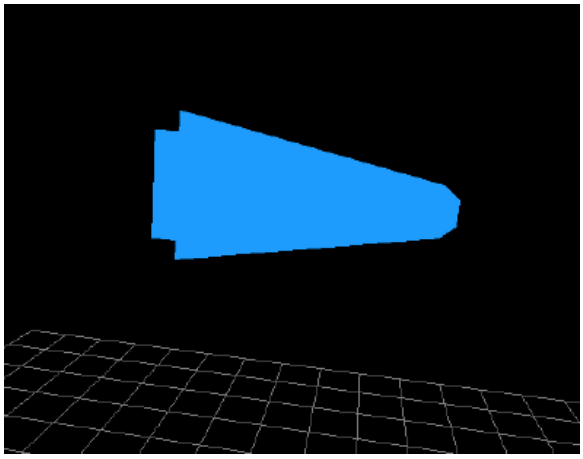

Figure 4.11: A VP1 software visualization of a single NSW chamber with geometry described using the XML scheme and built with MuonGeoModel, showing the complex shapes which can be modelled using our modified version of MGM designed for NSW simulation.

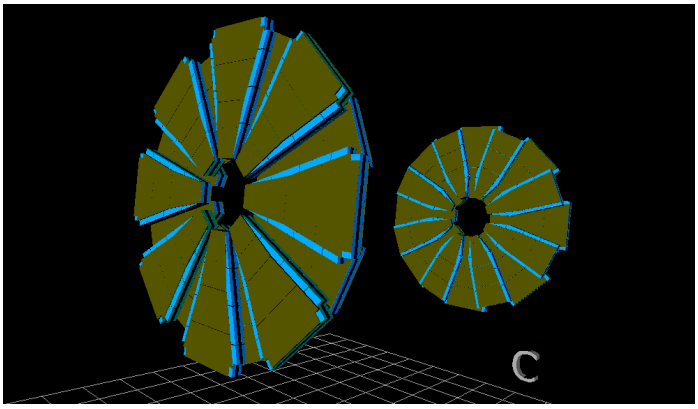

Figure 4.12: A VP1 software visualization of the entire NSW detector constructed on a chamber level using the XML scheme and NSW version of MuonGeoModel.

4.4.2 Production of N-tuples for Preliminary Analysis

After developing a way to implement the NSW geometry, it is possible to proceed to the next steps in the simulation chain. Like with the geometry, extensive modification of the existing Athena Framework was also required, but not to the extent of completely re-architecting the existing implementation. In this section, the subsequent

simulation steps and our modifications are described.

Hits are detected in the geometry by linking them to sensitive volumes. Within the muon spectrometer code in Athena, two new types of sensitive volumes are created, one for MM and one for sTGC. These sensitive volumes linked to the geometry form a sensitive detector which can detect hits. Built into MGM is also the material used for each detector (the gas mixture of sTGC and MM and G10 for the spacer). Geant4 is used to propagate particles through the geometry built by MGM and as particles pass through the sensitive detectors, hits are recorded. Figure 4.13 is a visualization of hits recorded by a dummy NSW geometry.

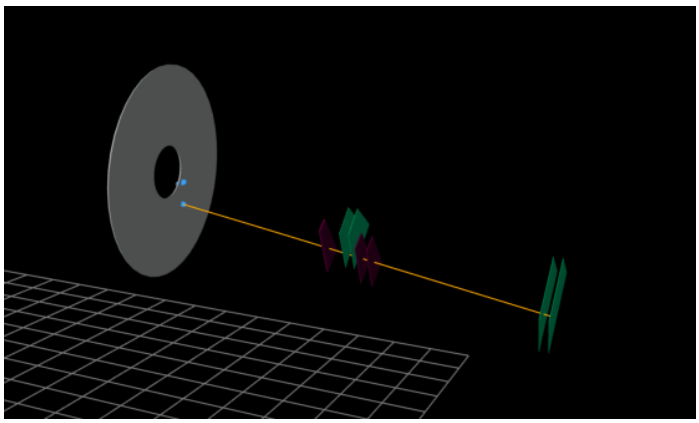

Figure 4.13: Hits on the NSW sensitive volume. Because this was first implemented before the NSW geometry was finalized, a circular disk is used in place of the actual NSW geometry shown in the last section. The blue dots shows that we have successfully transformed an XML based geometry object into a sensitive volume capable of recording hits in Athena.

Because the full simulation chain with digitization, trigger, and reconstruction will take quite some time to complete and involve the efforts of multiple groups, we first produced a simplified set of simulated events. These hit n-tuples were generated using the full NSW geometry and made available to the NSW community for early

performance studies. Hits recorded on the NSW sensitive volumes can in principle store any Geant4 variable. The first NSW simulated events contained the following variables:

- Global Position
- Global Direction
- Global Time
- PDG code
- Step Length
- Energy Deposited
- Kinetic Energy
- Local Position

The local position is the coordinates of the hit relative to the center of the chamber. Using the identification scheme described previously, it is possible to identify which chamber a hit occurred on. These variables are saved in a newly created Athena object called GenericMuonSimHit. The muon spectrometer Athena packages were then modified so that GenericMuonSimHit along with its associated Geant4 variables are saved into the output POOL ROOT file generated by Athena. Compatibility with Athena is maintained and the output can be obtained by running a fairly standard Athena job options file. N-tuples with events from a single muon gun were generated to support early NSW performance studies.

While by no means complete, this is an important first step in developing a full simulation framework for the NSW. This is an area of ongoing work by the New Small Wheel team and will continue to be the area of much development over the next couple years.

Chapter 5

ATLAS b-jet Energy Measurement and Systematic Uncertainties

Jets are the key ingredients to a whole host of measurements at the LHC and in order to reach the ATLAS experiment's physics goals, it is essential to have good jet detection, simulation, and reconstruction performance. In ATLAS, jets are typically reconstructed by searching for groups of topologically related energy deposits in the ATLAS calorimeters that also have associated charged particle tracks in the inner detector. Reconstruction is typically done using the anti-k_t algorithm [35] and this reconstruction is calibrated using Monte Carlo simulations.

Systematic uncertainties related to jet energy measurements are among some of the largest sources of experimental uncertainties for many ATLAS analyses, and this is particularly acute for analyses that depend heavily on b-jets such as the analysis described in this thesis. The b-jet energy scale uncertainty also can impact the b-

tagging calibration and give an additional contribution to the uncertainties on the final measurement.

In this chapter, an analysis done with the ATLAS Jet/EtMiss Working Group on studying the JES and systematic uncertainties related to b-jets is described. This work was done between Fall 2011 and Summer 2012 using data collected at ATLAS in 2011. This is one of the first validations of b-jet reconstruction performance at ATLAS using the full 2011 dataset and is key to better understanding b-jets in ATLAS. In section 5.1, we first discuss the motivation and goals of the study. Then in section 5.2, the MC and data samples used are described. Section 5.4 describes the analysis setup and the selection cuts and object definition. Finally, the results are shown in section 5.7.

5.1 Motivation and Goals

The purpose of this analysis is to validate the JES in b-jet decays. This is important because in a semi-leptonic b-jet decay, the muon (and the neutrino) actually carries a substantial portion of the total momenta, and the calorimeter response will be different because the jet has different characteristics. We need to establish that the JES scale factors and corrections applied to jets in fact also work reasonably well for b-jets. This can be done through studying two different types of samples: Dijets and Z+Jet. The Dijet balance studies were conducted by K. Mercurio [10] and require that two jets be b-tagged and the probe jet is required to have a selected reconstructed muon within ΔR <0.4.

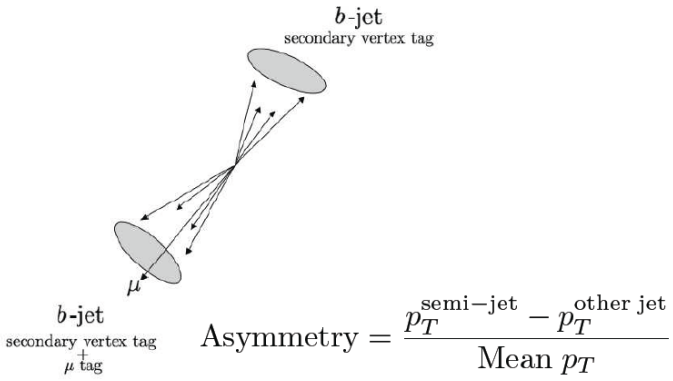

Figure 5.1: Diagram of Dijet balance studies and asymmetry.

However, the Dijet triggers do not give enough statistics at low P_T. Thus, the analysis described in the next sections looks at the Z+Jet samples in order to validate the corrections in b-jets at lower P_T and then the results are combined with the results from Dijets to validate over the entire P_T spectrum. Also, in the Z+Jet samples, unlike in Dijets, the absolute neutrino effect can be probed. Figures 5.2-5.4 show diagrammatically the process which we utilize.

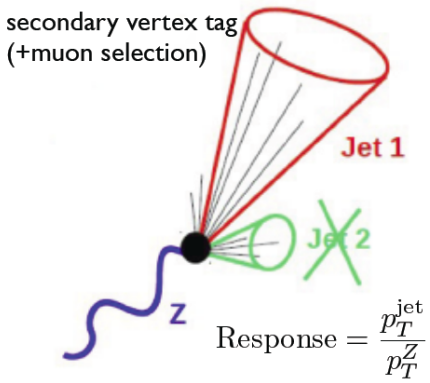

Figure 5.2: Diagram of Z+Jets balance studies and response.

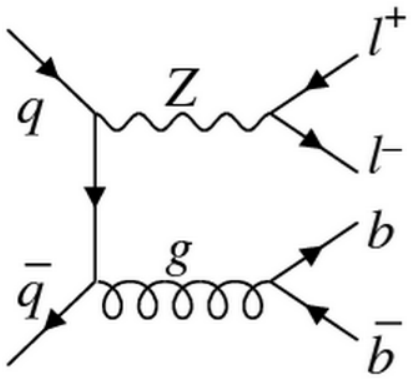

Figure 5.3: Diagram of Z+Jets production.

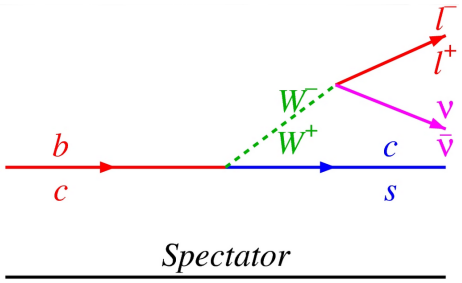

Figure 5.4: Semi-leptonic b-jet decay.

5.2 Data Samples and Definitions

All of the data and Monte Carlo samples used in this analysis are processed using Release 17 of the ALTAS software. For the data, we use the $\sqrt{s} = 7$ TeV data from the 2011 ATLAS run corresponding to an integrated luminosity of 4.7 fb^{-1}. An overview of the data and Monte Carlo samples are given below in Table 5.1.

In the analysis, we use the following definitions:

Data (2011, Period D-M [8])
data11_7TeV.periodM.physics_JetTauEtmiss.PhysCont.NTUP_JETMET.grp09_v02_p766/ data11_7TeV.periodL.physics_JetTauEtmiss.PhysCont.NTUP_JETMET.grp09_v02_p766/ data11_7TeV.periodF.physics_JetTauEtmiss.PhysCont.NTUP_JETMET.grp09_v01_p766/ data11_7TeV.periodE.physics_JetTauEtmiss.PhysCont.NTUP_JETMET.grp09_v01_p766/ data11_7TeV.periodD.physics_JetTauEtmiss.PhysCont.NTUP_JETMET.grp09_v01_p766/ data11_7TeV.periodG.physics_JetTauEtmiss.PhysCont.NTUP_JETMET.grp09_v01_p766/ data11_7TeV.periodI.physics_JetTauEtmiss.PhysCont.NTUP_JETMET.grp09_v01_p766/ data11_7TeV.periodH.physics_JetTauEtmiss.PhysCont.NTUP_JETMET.grp09_v01_p766/ data11_7TeV.periodK.physics_JetTauEtmiss.PhysCont.NTUP_JETMET.grp09_v01_p766/ data11_7TeV.periodB.physics_JetTauEtmiss.PhysCont.NTUP_JETMET.grp09_v01_p766/ data11_7TeV.periodM.physics_JetTauEtmiss.PhysCont.NTUP_JETMET.grp09_v01_p766/ data11_7TeV.periodL.physics_JetTauEtmiss.PhysCont.NTUP_JETMET.grp09_v01_p766/ data11_7TeV.periodJ.physics_JetTauEtmiss.PhysCont.NTUP_JETMET.grp09_v01_p766/
MC11c (Alpgen+Herwig)
mc11_7TeV.*ZeeNp*p833/ mc11_7TeV.*ZeebbNp*p833/ mc11_7TeV.*ZmumuNp*p833/ mc11_7TeV.*ZmumubbNp*p833/
MC11b (Pythia)
mc11_7TeV.106047.PythiaZmumu_no_filter.merge.NTUP_SMWZ.e815_s1272_s1274_r2920 _r2900_p801/ mc11_7TeV.106046.PythiaZee_no_filter.merge.NTUP_SMWZ.e815_s1272_s1274_r2920_r2900 _p801/

Table 5.1: An overview of the Data and Monte Carlo samples used in the Z+Jet analysis. For the MC11c, there are many individual datasets so the '*' are wildcards.

- **Inclusive** - All Z+Jet events in the sample passing our selection cuts.

- b**-tagged** - Z+Jet events where the selected jet is b-tagged. The b-tagger used is the JetFitterCOMBNN algorithm at the 80% and the 57% operating points.

- b**-tagged + muon** - Z+Jet events which are b-tagged and also have a STACO combined muon within $\Delta R < 0.4$ of the b-jet. The presence of the muon suggests that the b decayed semileptonically and that there is a neutrino present in the decay.

5.3 Jet Reconstruction and Calibration

Jets are reconstructed using the Anti-k_t algorithm [35] with a distance parameter of R = 0.4. Anti-k_t jets with distance parameter of R = 0.6 are also available but the b-tagging algorithms at the time this study was performed were only calibrated to the R = 0.4 Anti-k_t jets. The energy deposits in the ATLAS calorimeters are first reconstructed at the so called EM scale, which has correctly calibrated the energy deposited by electromagnetic showers in the calorimeters [12]. This scale is established by using test-beam measurements of electrons and muons in the barrel and endcap, and then also validating with cosmic rays.

The jet energy scale is derived as a calibration factor that varies according to η and P_T and is derived from an inclusive jet Monte Carlo sample. Applying the JES then gives us "EM+JES" calibrated jets. The additional energy from pileup is also added as a correction constant. In-time pileup (pileup from additional proton-proton collisions occurring in the same bunch crossing) will lead to additional energy in the reconstructed jet while out-of-time pileup (pile-up from additional proton-proton collisions occurring in bunch-crossings just before and after the collision of interest) actually decreases the measured energy due to the undershoot of calorimeter pulses from preceding bunch crossings [12].

A Local Cluster Reweighting (LCW) calibration [13] is also applied. The LCW calibration takes advantage of the fact that electromagnetic and hadronic showers have different energy deposition topologies. For example, electromagnetic showers are more concentrated than hadronic ones at the same energy. Input clusters are

classified as either electromagnetic or hadronic and different dedicated corrections are applied to those clusters to improve jet energy resolution and reduce the jet flavor dependence. The resulting jets are known as "LCW+JES" jets.

5.4 Event and Object Selection

An initial set of cuts are used on the data and MC to prepare the datasets for use. For the data, we require that events pass the 2011 7 TeV data Good Run List (GRL). For the Alpgen+Herwig MC11c samples, we apply a HFOR cut. The purpose of the HFOR tool is to remove overlap of heavy flavor conponent between light jet inclusive and heavy flavor jet samples generated by Alpgen.

We use the following electron and muon triggers which are period dependent.

Period D-K

- Electron - EF_2e12_medium
- Muon - EF_mu15_mu10_EFFS

Period L-M

- Electron - EF_2e12Tvh_medium
- Muon - EF_mu15_mu10_EFFS_medium

We also require at least 3 tracks to be coming from the primary vertex. Prior to the selection, we also apply a number of corrections. These include reweighting of Monte Carlo for cross section and pileup reweighting.

We also apply the following jet corrections using the ApplyJetCalibration-00-00-08 tool developed by the ALTAS JetEtMiss Working Group. These corrections include:

- Pile-up Correction - Modifies the EM scale based on $< \mu >$, the average number of interactions per bunch crossing, and the number of primary vertices
- Origin Correction - Changes the jet direction to point to the primary vertex
- AbsoluteEtaJES - Corrects jet 4-vectors using a JES factor derived from Dijet events

These corrections work to bring jets from periods D-K and L-M into better agreement. Finally, we also use an Electron EnergyRescaler correction package. This package applies an energy scale correction to data electrons by using a data/MC derived scale factor. For Monte Carlo, this package applies a smearing to electrons that is derived from a fit of the Z peak.

5.4.1 Lepton Selection

For the analysis, we require that events either have a muon or electron pair. The electron and muon candidates are defined as follows:

Electrons

- Medium electron
- $|\eta| < 2.47$
- Reject gap electrons ($1.37 < |\eta| < 1.52$)

- $P_T > 20$ GeV

Muons

- Require STACO Combined Medium Muons
- $|\eta| < 2.47$
- $P_T > 20$ GeV

We exclude the electrons in the gap region between barrel and endcap where electrons are poorly reconstructed and require that leptons have a minimum P_T of 20 GeV.

5.4.2 Jet Selection

For the jet selection, we use AntiKt4TopoEM jets which are reconstructed using the anti-k_t algorithm with a cone size of R = 0.4 [35]. Then we also apply the following requirements:

- Require $P_T > 10$ GeV
- Reject if within $\Delta R < 0.1$ of one of the selected leptons

We further define the leading jet as the highest P_T jet which passes the above requirement and the sub-leading jet as the next highest P_T jet that passes the above requirements and also has a JVF > 0.5. JVF stands for Jet Vertex Fraction. JVF is the fraction of summed track P_T for all tracks matched to a given jet and associated with the primary vertex, relative to the total summed P_T for all tracks matched to the

jet [11]. A cut on JVF can be used to reject spurious calorimeter jets resulting from local fluctuations in pile-up activity, as well as real QCD jets origination from single pile-up interactions, resulting in improved stability of the reconstructed jet against pile-up.

5.4.3 Event Selection

To select candidate Z+Jet events, we first require at least 2 leptons passing our lepton selection (both electrons or both muons). If there are more than 2 leptons, we take the two leptons that have the highest P_T. Then, we apply the following cuts:

- The two opposite sign electrons or muons must have 66 GeV $< m_{ll} <$ 116 GeV, so that the selected di-lepton pair is consistent with a Z boson.
- One selected leading jet with JVF > 0.75 and $|\eta| < 1.20$
- A sub-leading jet veto which rejects the event if the P_T of the subleading jet is greater than 20% of the P_T of the Z boson candidate, OR, if the P_T of the subleading jet is greater than 10 GeV for events where the P_T of the Z boson candidate is less than 50 GeV.
- We require that the ΔR between the leading jet and both leptons be at least 0.35.
- Reject if the $\Delta\phi$ between the leading jet and the Z boson candidate is less than π - 0.2

Events that survive these requirements are considered to constitute the inclusive sample defined previously in Section 5.2. We perform some truth level studies

to establish which is the optimal b-tagging operating point to use. We use AntiKt4TruthWZ truth jets and match to b quarks within a ΔR cone of 0.3. Figure 5.5 shows the purity of selected b-jets and c-jets from the 57% and 80% JetFitterCOMBNN operating points. As we can see, the purity is much better for the 57% operating point so we use this operating point despite the lower statistics.

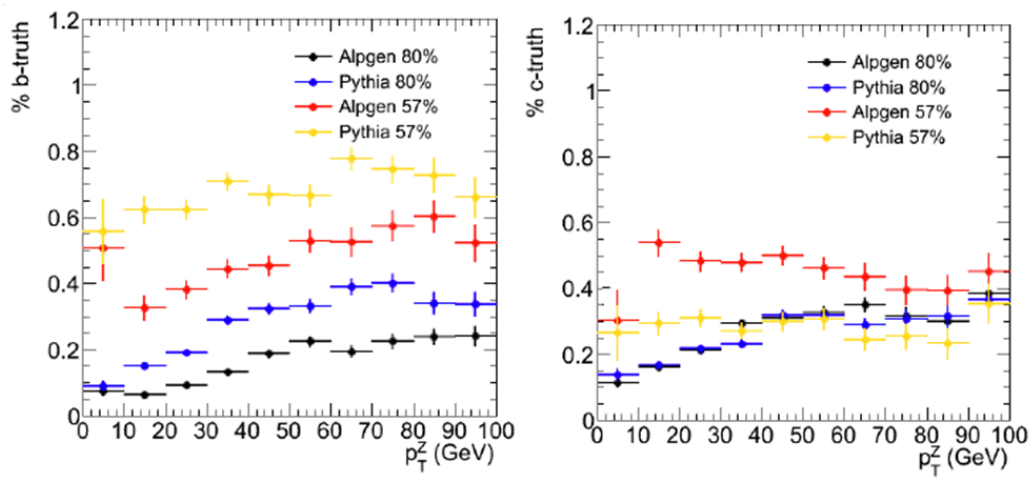

Figure 5.5: The percentage of b-tagged jets which are matched to truth b-jets (left) or truth c-jets (right) for both Alpgen and Pythia Z+Jet samples at the 57% and 80% JetFitterCOMBNN operating points as a function of b-tagged jet P_T.

5.5 Balance Studies

Before showing the results from the balance studies, it is necessary to first define a couple additional quantities.

SumPtTrk

The SumPtTrk is the vector P_T sum of all selected tracks associated with a selected jet. A ΔR cone size of 0.4 is used, which matches the cone size used by the anti-k_t algorithm. The following track selection is used:

- $P_T > 1$ GeV
- nPixel ≥ 1
- nSCT ≥ 6
- nTRT ≥ 0
- $|trk_{d0}| < 1.50$ mm (transverse impact parameter)
- $|trk_{z0} \times \mathrm{Sin}(trk_{\theta})| < 1.50$ mm (longitudinal impact parameter)

Now, we can define our balance quantities:

RZPt = JetPt/Z_{P_T}

RTRK = SumPtTrk/PtCalo

The PtCalo quantity is given by the variable jet_AntiKt4TopoEM_pt which is basically the selected jet P_T measured in the calorimeters only.

These are the two balance quantities we are primarily concerned with in this analysis. On top of these definitions, we also need to apply a couple corrections for the muon effect in b-jets which decay semi-leptonically:

PtTrk = SumPtTrk - muon_ID_pt (subtracted vectorially)

PtCalo = jet_AntiKt4TopoEM_pt - muon_Eloss_Pt

We subtract the muon from SumPtTrk because it doesn't deposit much energy in the calorimeter so this subtraction is necessary to get a meaningful RTRK ratio. We also remove the little bit of energy that the muon does deposit in the calorimeter (muon_Eloss_Pt is the energy lost by the muon in the calorimeter). We also correct JetPt by adding back in the P_T that is carried by the muon in the jet as shown below:

JetPt = jet_AntiKt4TopoEM_pt + Muon_STACO_Pt - muon_Eloss_Pt

By subtracting out the muon contribution to the calorimeter energy, we ensure that that portion of the muon P_T is not counted twice.

5.5.1 Poisson Fits

Special care must be taken when determining the RZPT for a particular Z_{P_T} bin. The most obvious way to do it to calculate the RZPT for each event which falls within a certain Z_{P_T} bin and take an arithmetic mean of all the events. However, when this is done, the resulting distribution of RZPT vs Z_{P_T} is shown in Figure 5.6.

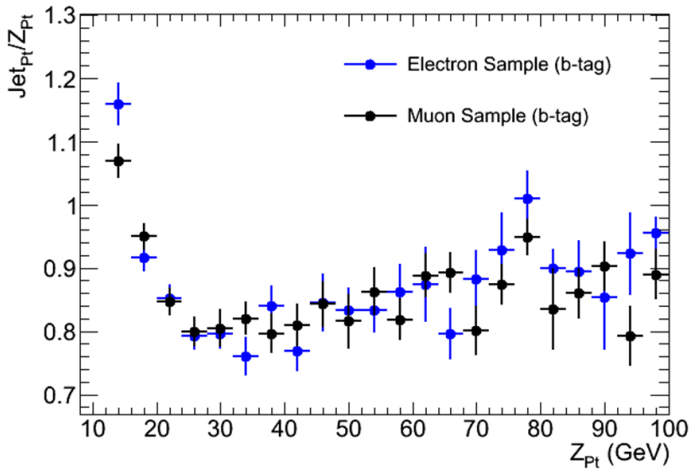

Figure 5.6: RZPT as a function of Z_{P_T} in Monte Carlo where the value of RZPT in each bin is determined by taking the arithmetic mean of all measurements.

This distribution exhibits an unphysical rise in RZPT at lower values of Z_{P_T}. We can understand this by looking closer at the RZPT distribution in a single Z_{P_T} bin. An example of such a bin is shown in Figure 5.7.

The presence of a high RZPT tail skews the arithmetic mean upwards. The RZPT distribution is skewed upwards in the lower P_T bins due to the 10 GeV Jet P_T

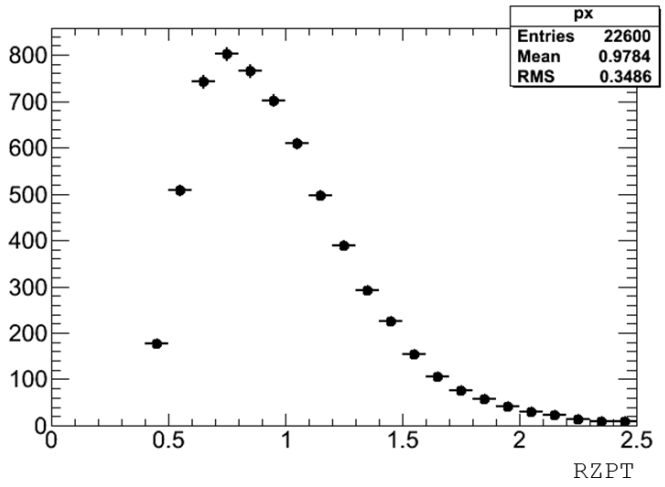

Figure 5.7: RZPT distribution in the 20 GeV $< Z_{P_T} <$ 30 GeV bin in Monte Carlo. The y-axis gives the number of events.

threshold from Section 5.4.2. The solution is to fit the distribution with a generalized Poisson distribution to derive the mean. This distribution is given by Equation 5.1 below

$$P(x; a, \lambda) = \frac{\lambda^{ax} e^{-\lambda}}{\Gamma(ax + 1)} \tag{5.1}$$

where Γ is the Euler's Gamma function. However, we also need to account for the jet P_T threshold cutoff. This is done by multiplying Equation 5.1 by a function $f(x)$ defined as:

$$\begin{aligned} f(x) &= 1 \text{ for } x > 10/Z_{P_T}\text{\_min} \\ f(x) &= 0 \text{ for } x < 10/Z_{P_T}\text{\_max} \\ f(x) &= \text{ Linear Function in Between} \end{aligned} \tag{5.2}$$

where x is the value of RZPT. This accounts for the fact that for a given Z_{P_T} bin,

it is not possible to have a value of RZPT less than $10/Z_{P_T}$_max. It also accounts for the fact that RZPT measurements above $10/Z_{P_T}$_min are not susceptible to being impacted by the 10 GeV minimum jet P_T threshold. Figure 5.8 below shows an example of such a fit in the 20 GeV $< Z_{P_T} <$ 30 GeV bin.

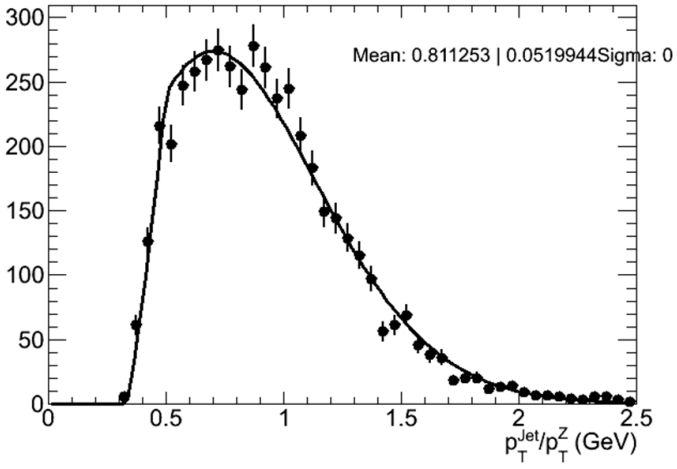

Figure 5.8: The fitted RZPT distribution in the 20 GeV $< Z_{P_T} <$ 30 GeV bin in Monte Carlo.

In the higher P_T bins, the distributions become fairly Gaussian so we revert to taking the arithmetic mean for bins with $Z_{P_T} > 40$. The impact of this fit in correcting the lower P_T RZPT values can be seen in the lowest P_T bin of Figure 5.14.

5.6 Systematic Uncertainties

In this analysis, we consider several systematics for RTRK and RZPT. The systematics used for each measurement is described below:

RTRK

- Jet Energy Resolution - Here we use the Jet Correction Tool developed by the

Jet/ETMiss working group with the default settings which smears the JER by 1σ.

- Monte Carlo Tune - We compare Pythia versus Alpgen+Herwig samples.
- Dead Material - During the SumPtTrk calculation, we artificially decrease the track reconstruction efficiency by 2%.
- Jet Fragmentation - We assume this to be a constant 1%.

RZPT

- Jet Energy Resolution - Here we use the Jet Correction Tool developed by the Jet/ETMiss working group with the default settings which smears the JER by 1σ.
- Monte Carlo Tune - We compare Pythia versus Alpgen+Herwig samples.
- $\Delta\phi$ - We vary the cut on $\Delta\phi$ between the leading jet and Z boson candidate by +/- 0.01 around the central cut value of π-0.2.
- Second Jet P_T Veto - We vary the cut +/- 0.05 around the central value of 0.2.
- JVF - We vary the cut by +/- 0.05 around the central value of 0.75.
- Electron Resolution/Scale - We use the upwards and downwards shift provided by the Electron EnergyRescaler package.

5.7 Results

In validating the JES and other jet calibrations in the 2011 ATLAS data and checking the agreement with Monte Carlo, one of the first things we look at is whether data periods D-K and L-M are in agreement with each other after all jet corrections have been applied. It is necessary to take a closer look at this because the two sets of periods have different pileup conditions which could impact the JES. Figures 5.9 and 5.10 below show the comparison of RZPT and RTRK for the two sets of data periods.

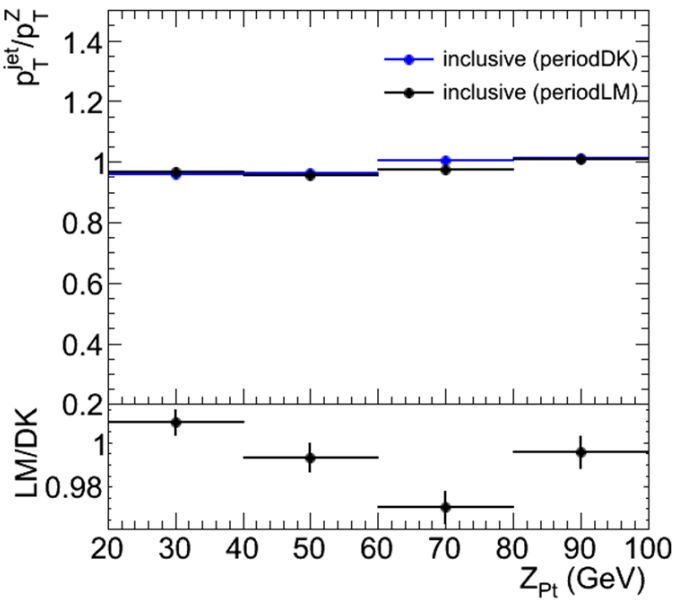

Figure 5.9: Comparison of RZPT for ATLAS 2011 data periods D-K and L-M.

We found that the agreement is relatively good which means that it is safe to combine the data from period D-K with L-M to get more statistics for our studies. It also means the JES corrections used in the two data periods are consistent and are

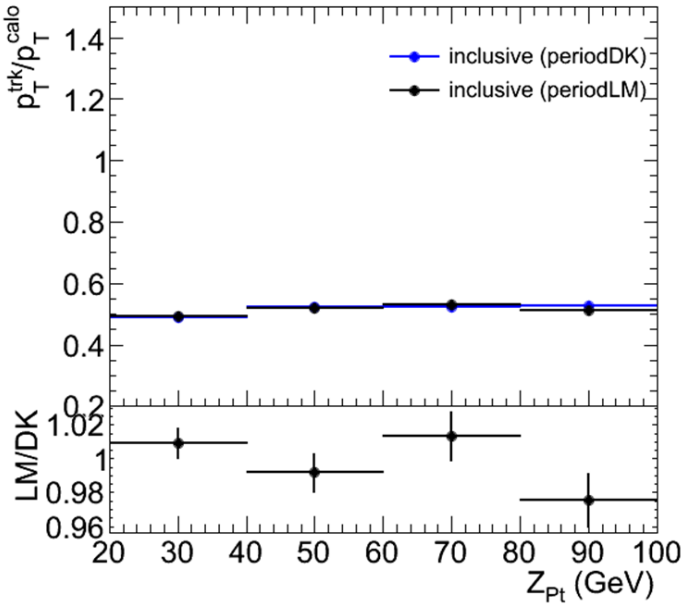

Figure 5.10: Comparison of RTRK for ATLAS 2011 data periods D-K and L-M.

properly handling the differences in pileup conditions.

First, we look at the result for the RTRK ratio which helps us to validate the calorimeter jet energy measurements. The two Monte Carlo datasets we are using are generated using Pythia and Alpgen and Figure 5.11 shows the comparison to data for those two generators.

The immediate observation is that Pythia has much better agreement with data and is approximately 2% higher compared to Alpgen. This is actually not the first time issues were observed with Alpgen as this was also spotted in other analyses using these samples. As a result, we use only Pythia for the RTRK studies. In Figure 5.12 and Figure 5.13 below, the RTRK and associated systematic uncertainties are shown for the inclusive sample and b-tagged samples.

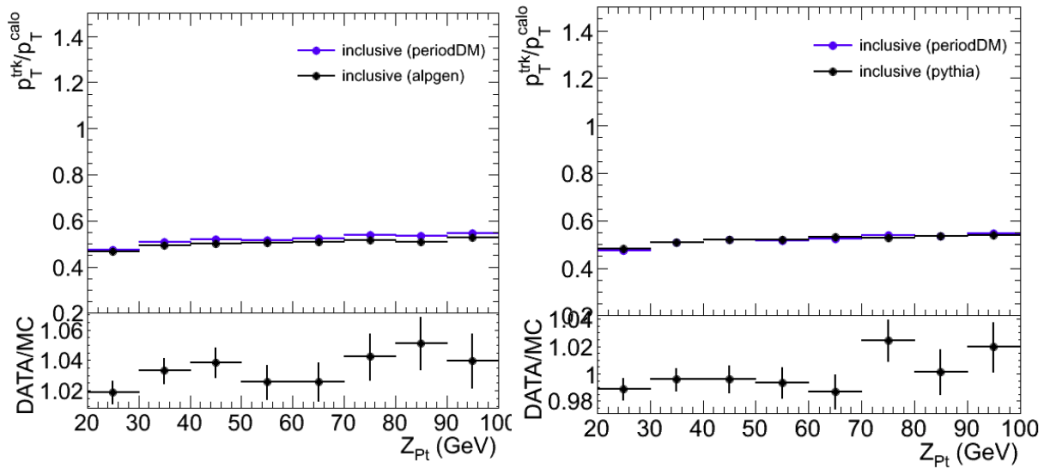

Figure 5.11: Comparison of Z+Jets RTRK for Alpgen and Pythia MC with ATLAS 2011 data periods D-M, plotted as a function of Z_{P_T}.

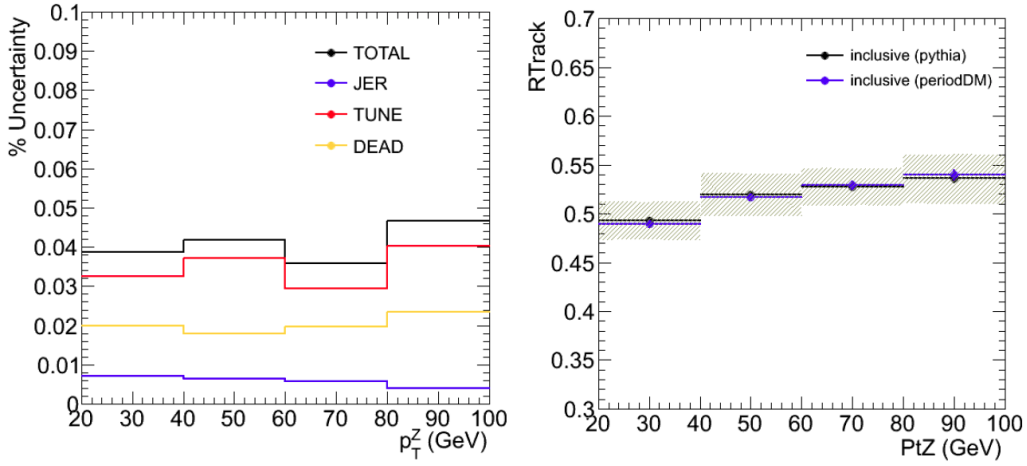

Figure 5.12: Comparison of Z+Jets RTRK for Pythia and ATLAS 2011 data periods D-M, plotted as a function of Z_{P_T}, along with the estimated systematic uncertainty, for the inclusive selection.

We notice that the dominant source of systematic uncertainty for the inclusive selection actually comes from the MC tune, and this actually improves when we go to the b-tagged selection. The overall systematic uncertainties are 4% and 3% for the inclusive and b-tagged selections respectively. For both inclusive and b-tagged selec-

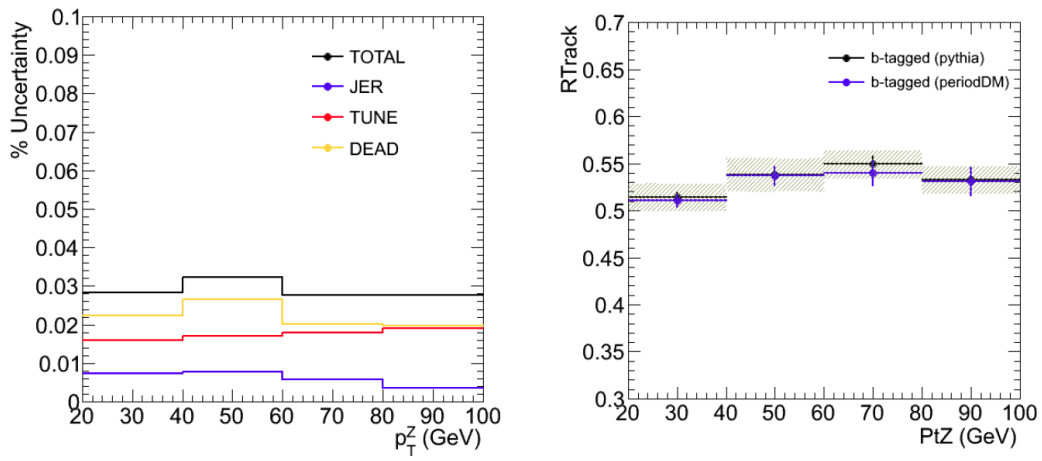

Figure 5.13: Comparison of Z+Jets RTRK for Pythia and ATLAS 2011 data periods D-M, plotted as a function of Z_{P_T}, along with the estimated systematic uncertainty, for the b-tagged selection.

tions, we have excellent data and Monte Carlo agreement within the uncertainties. This is the first validation of the calorimeter jet energy measurements for b-jets going down to 20 GeV.

Next we look at the results for the RZPT balance ratio. First we look at the agreement between data and MC, along with the agreement between the two generators, Alpgen and Pythia. The results for the inclusive sample are shown below in Figure 5.14.

The agreement in the first bin is a bit off because of low statistics in that bin in the MC sample causes the fit to be a bit skewed. To handle this, we increase the size of the binning in the subsequent results. Because value of that first bin is determined via a fit, the ROOT software package does not handle the error properly and outputs zero for the error in the plots. Shown below in Figure 5.15 is the data and MC comparison with Alpgen and Pythia for the b-tagged sample.

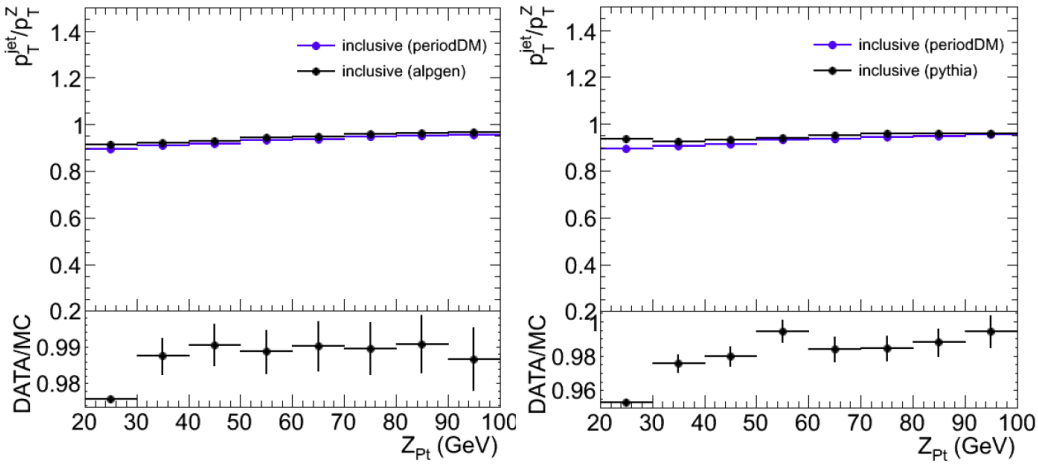

Figure 5.14: Comparison of RZPT for ATLAS 2011 data periods D-M with Alpgen (left) and Pythia (right) Monte Carlo datasets with the inclusive selection.

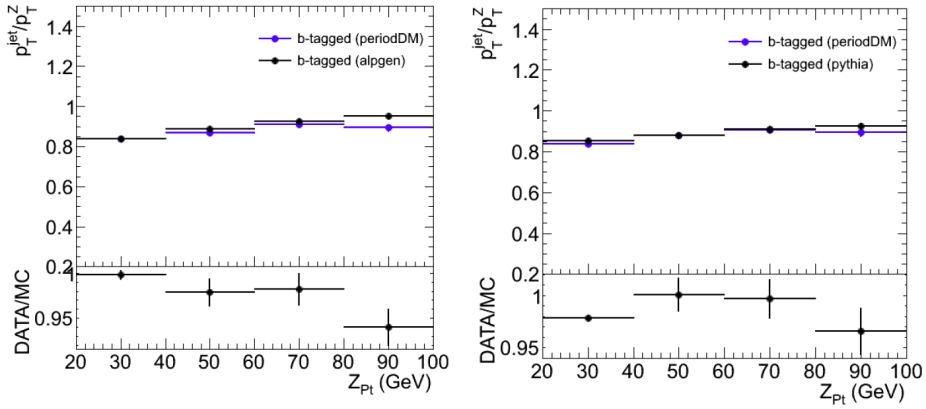

Figure 5.15: Comparison of RZPT for ATLAS 2011 data periods D-M with Alpgen (left) and Pythia (right) Monte Carlo datasets with the *b*-tagged selection.

A couple trends can be seen in Figures 5.14 and 5.15. First is that differences between Alpgen and Pythia seem to be quite minor, on the order of 1%. Secondly, we see that the MC tends to be between 1-2% higher than the data which is within the systematic uncertainties shown next, but implies that perhaps some of the jet corrections could be improved to compensate for this. The systematic uncertainties on RZPT are shown below in Figure 5.16. We see the total systematic on RZPT is

on the order of 2% all the way down to 20 GeV.

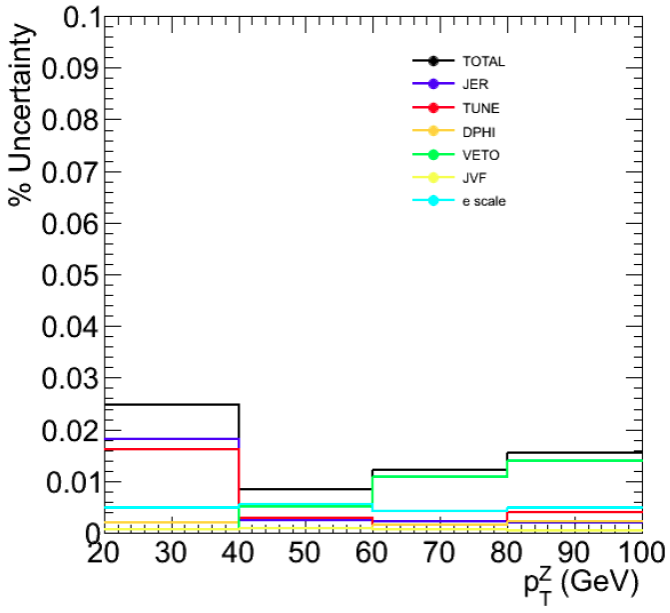

Figure 5.16: The total systematic on the inclusive RZPT balance broken down into individual components.

Next, we want to probe the neutrino effect in b-jets. This is done by using a ratio of the RZPT ratio, as shown in equation 5.3.

$$\frac{RZPT_{b-tagged}}{RZPT_{inclusive}} \tag{5.3}$$

This ratio is plotted below in Figure 5.17 for both Pythia and Periods D-M. The uncertainties which are used to set the error bars in Figure 5.17 come from the systematics which are shown in Figure 5.18.

We observe that the ratio of RZPT is at around 0.95 indicating a 5% shift from the neutrino effect. This effect comes from the fact that about 40% of b-jets will decay semileptonically and thus have a non-negligible amount of their energy carried

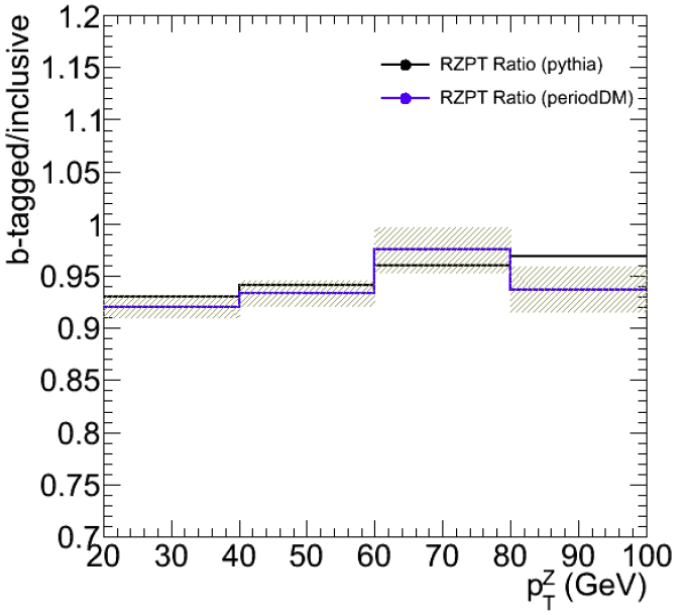

Figure 5.17: The ratio of RZPT for inclusive and b-tag selections for both Pythia and Periods D-M.

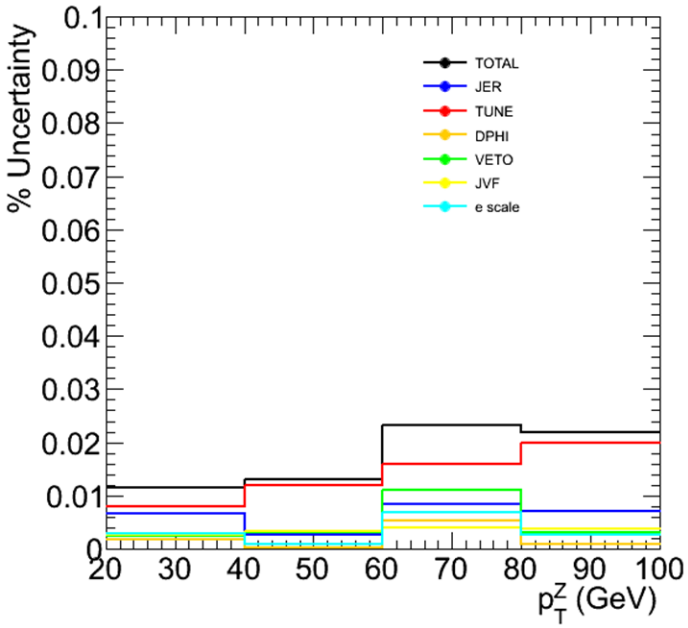

Figure 5.18: The total systematic on the ratio of RZPT for inclusive and b-tag selections for both Pythia and Periods D-M.

by the neutrino. The total systematic uncertainty on the ratio between the b-jet and light jet balance is derived by adding in quadrature the individual components shown in Figure 5.18. The uncertainty is actually dominated by the uncertainty from the generator tune. This is because many of the systematic uncertainties entering both the numerator and denominator of the ratio are correlated and thus approximately cancel, resulting in a reduced systematic uncertainty of around 2%.

We have agreement within our systematic uncertainties between the data and Monte Carlo simulation which validates the description of the process. As part of the ongoing work in the JetEtMiss Working Group, this process will be used to derive a correction that can be used to improve the reconstruction of b-jets identified as semileptonic by correcting the response of semileptonically decaying b-jets to that of the inclusive b-tagged jet sample. This process will also be repeated again in 2015 on the new 13 TeV datasets.

The results presented here are the first comprehensive study done on the Z+Jet balance and RTRK with b-jets in the 2011 ATLAS data. For the first time, the associated systematic uncertainties are estimated and the data and Monte Carlo agreement is validated down to 20 GeV. The various b-jet scale factors and corrections used in the SUSY analysis described in this thesis were derived from studies like this one. These results along with follow up performance studies done with the 2012 ATLAS data have played an important role in improving the ATLAS b-jet reconstruction performance and leading to better sensitivity in analyses with b-jets such as the one described in the next chapter.

Chapter 6

Search for Weak Gaugino Production in $\tilde{\chi}_2^0\tilde{\chi}_1^\pm \to 1l2b + \not{E}_T$

In this section, a search for SUSY using the $\tilde{\chi}_2^0\tilde{\chi}_1^\pm \to 1l2b+\not{E}_T$ channel is described. Figure 6.1 shows the Feynman diagram for the process of interest. A $\tilde{\chi}_1^\pm$ and $\tilde{\chi}_2^0$ are directly produced and the $\tilde{\chi}_2^0$ decays via a Higgs boson. This analysis was conducted at CERN from 2012 through 2014, and the results published in European Physics Journal C in combination with several other decay channels which were investigated by other teams in the ATLAS SUSY Working Group [24]. From this analysis, two ATLAS Internal Notes, ATL-COM-PHYS-2013-1640 and ATLAS-COM-PHYS-2014-965 and one ATLAS Conference Note, ATLAS-CONF-2013-093 were also produced. As numerous improvements were made after the publication of ATLAS-CONF-2013-093, that Conference Note is a bit outdated compared to the most up to date results presented here.

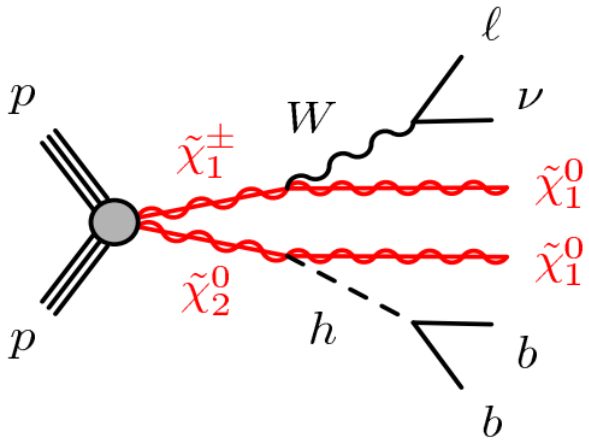

Figure 6.1: Feynman diagram for $pp \to \tilde{\chi}_2^0\tilde{\chi}_1^\pm \to W^\pm(\to l^\pm\nu)\tilde{\chi}_1^0 + h(\to b\bar{b})\tilde{\chi}_1^0$.

Due to the shortcomings of the Standard Model (SM) of particle physics, searches for new physics are a core part of the physics programme at the LHC. Among the Beyond Standard Model (BSM) theories, Supersymmetry is a leading candidate and has been the focus of much research at both the CMS and ATLAS experiments.

A lot of the recent searches have focused heavily on the production of sparticles via strong interactions and have failed to find any signs of SUSY. These results suggest that the mass of the gluino and the first and second generation squarks are quite heavy and in the multi-TeV range [31], while third generation squarks are also disfavored below 1 TeV (but not yet entirely excluded)[18][26]. A summary of the current (at time of writing) ATLAS SUSY Search results is given below in Figure 6.2.

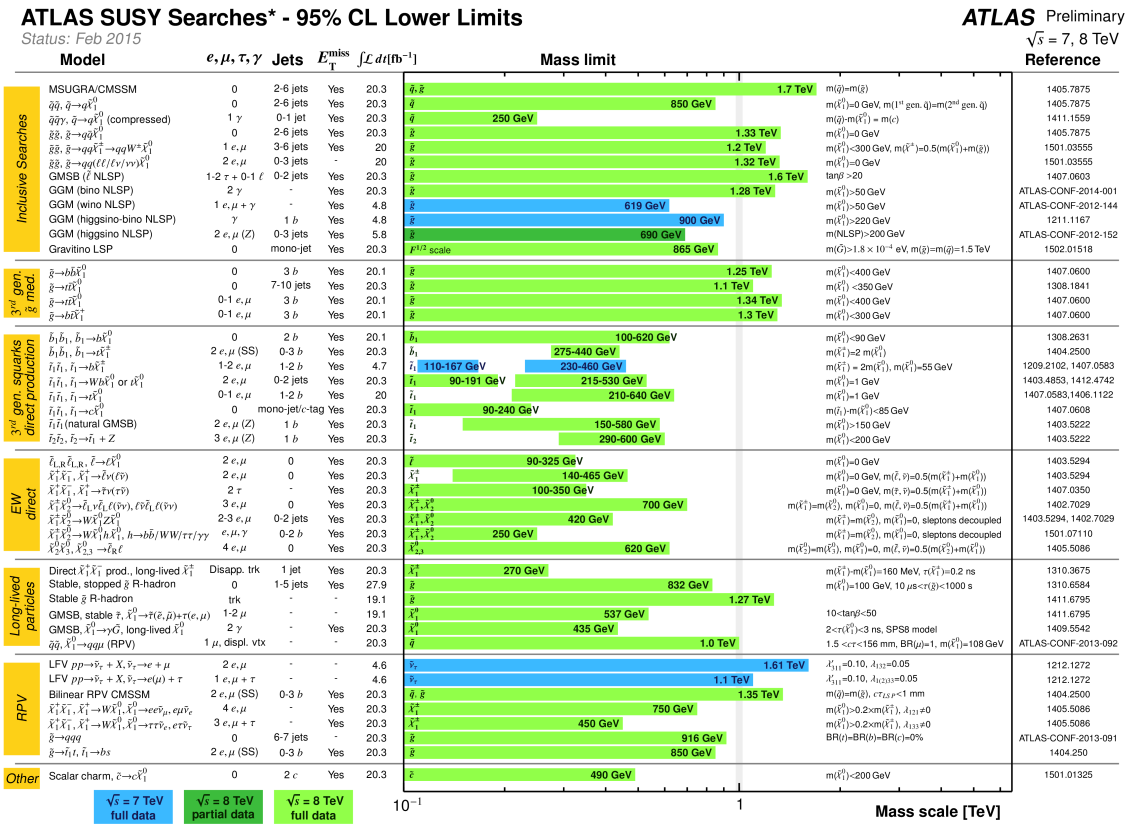

Figure 6.2: A summary of ATLAS SUSY searches 95% CL exclusion lower limits as of February 2015 [39].

6.1 Theoretical Motivation

In the very likely scenario where squarks are multi-TeV and inaccessible to ATLAS searches done at $\sqrt{s}$=8 TeV, then perhaps SUSY is "split". In such a split-SUSY scenario, all scalar superparticles are in the multi-TeV range with a 2-3 TeV gluino and somewhat lighter Higgsinos/Gauginos with $\mu \approx$ 500 GeV - 1 TeV. Then, there is one light h^0 that is slightly tuned. In such a scenario, the most likely LHC discovery mode is through direct gaugino and not strong searches.

Given the promise of direct gaugino searches, both ATLAS and CMS have already performed a number of searches for the production of $\tilde{\chi}_1^\pm - \tilde{\chi}_2^0$ through a wide variety of decay modes [16][15][19][25]. Some of these decay modes and corresponding Feynman diagrams are provided below in Table 6.1 and Figure 6.3.

Production	Decay	Signal Region
$\tilde{\chi}_2^0\tilde{\chi}_1^\pm$	$(l^+l^-\tilde{\chi}_1^0) + (l^\pm\nu\tilde{\chi}_1^0)$	3 lep
	$(l^+l^-_{\text{miss}}\tilde{\chi}_1^0) + (l^\pm\nu\tilde{\chi}_1^0)$	2 lep (OS or SS) + jet veto
	$(l^+l^-\tilde{\chi}_1^0) + (qq\tilde{\chi}_1^0)$	OS 2 lep + jets
$\tilde{\chi}_1^+\tilde{\chi}_1^-$	$(l^+\nu\tilde{\chi}_1^0) + (l^-\nu\tilde{\chi}_1^0)$	OS 2 lep + jet veto
$\tilde{\chi}_2^0\tilde{\chi}_2^0$	$(l^+l^-\tilde{\chi}_1^0) + (l^+l^-\tilde{\chi}_1^0)$	4 lep

Table 6.1: Summary of multi-lepton channels for Direct Gaugino searches. OS and SS stand for Opposite Sign and Same Sign where lep is short for lepton.

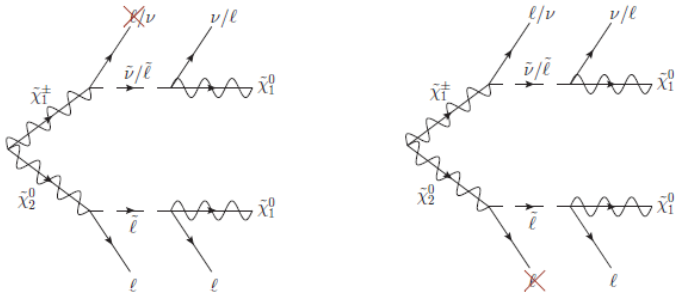

Figure 6.3: Diagrams for 2 and 3 lepton Gaugino decays where one lepton is not properly reconstructed.

Prior to this analysis, most ATLAS and CMS searched for gauginos via decays into 2 or 3 leptons. However, if sleptons are heavy similar to squarks, then all of these decays will be heavily suppressed and decays via gauge bosons and Higgs will dominate. In this scenario, the decay of gauginos via Standard Model bosons can be the dominant SUSY decay channel accessible at the LHC.

In this thesis, we look specifically at the process where the $\tilde{\chi}_2^0$ decays via the Standard Model Higgs which is shown in Figure 6.4. While $\tilde{\chi}_2^0 \to Z\tilde{\chi}_1^0$ is also another

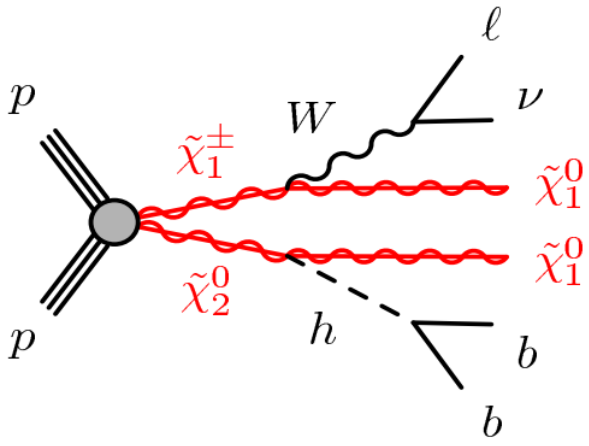

Figure 6.4: Feynman diagram for $pp \to \tilde{\chi}_2^0\tilde{\chi}_1^\pm \to W^\pm(\to l^\pm\nu)\tilde{\chi}_1^0 + h(\to b\bar{b})\tilde{\chi}_1^0$.

possible channel, there are large regions of phase space where $BR(\tilde{\chi}_2^0 \to h\tilde{\chi}_1^0)$ is dominant by far, in particular when the mass splitting is sufficient ($\Delta m = m_{\tilde{\chi}_2^0} - m_{\tilde{\chi}_1^\pm} > m_h$) and when $\tilde{\chi}_2^0$ is mostly neutral wino and $\tilde{\chi}_1^0$ is mostly bino. Table 6.2 gives an example of a set of pMSSM parameters which yield $BR(\tilde{\chi}_2^0 \to h\tilde{\chi}_1^0) = 82\%$.

Parameter	Value (GeV)	Parameter	Value (GeV)
M_1	100	m_{q_L}	2000
M_2	250	m_{Q_L}	4000
M_3	1000	m_{e_L}	2000
$tan(\beta)$	20	m_{e_R}	2000
A_t	100	m_{u_R}	2000
A_b	100	m_{d_R}	2000
A_τ	100	m_{τ_L}	2000
μ	500	m_{τ_R}	2000
M_A	250	m_{t_R}	2000
		m_{b_R}	2000

Table 6.2: A sample set of pMSSM parameters that yields $BR(\tilde{\chi}_2^0 \to h\tilde{\chi}_1^0) = 82\%$.

This set of parameters has characteristics of much of the pMSSM space that we

explore in this analysis. For example, we provide sufficient spacing between M_1 and M_2 so an on-shell $\tilde{\chi}_2^0$ can decay into h^0 and $\tilde{\chi}_1^0$. Furthermore, we need to tune the model to be compatible with m_h=125 GeV and for this, we need to set a larger value of $tan(\beta)$, a large value of A_t, and a rather massive stop (so large value for m_{Q_L}). We also need to disallow $\tilde{\chi}_2^0$ and $\tilde{\chi}_1^\pm$ decays to sleptons and squarks and we achieve this by setting the sparticle masses to 2 TeV. Finally, because a light gluino is already largely excluded, we set M_3=1 TeV.

6.2 SUSY Signals

For this analysis, we focus on the final state which consists of 1 lepton, 2 b-jets, and large $\not{E}_T$. The $h \to b\bar{b}$ channel is selected because the cross section for SUSY production is already quite low so picking the Higgs channel with the largest cross section improves our odds of having sensitivity with 20.3 fb^{-1} of 8 TeV data. The large $\not{E}_T$ should allow us to have fairly good background suppression.

As this is a new channel that has never been studied before, there were no existing data samples which can be used and it was necessary to do the full SUSY Monte Carlo sample generation using the ATLAS framework. The general SUSY Monte Carlo sample generation process is shown schematically in Figure 6.5.

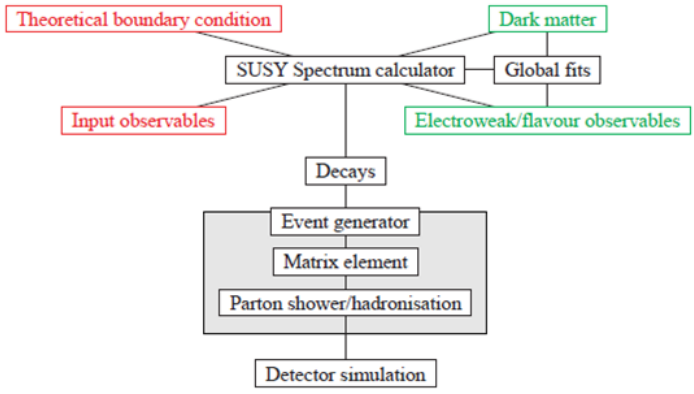

Figure 6.5: Schematic showing the steps for producing SUSY Monte Carlo samples.

The first step is to use SOFTSUSY 2.0.5 [7] to generate a spectrum for our pMSSM model. Following this, we perform some customizations on the spectrum, largely to make it a split-SUSY scenario with heavy sparticles. The resulting spectrum is then fed to HERWIG++ 2.5.2 [27] which is the event generator used. For efficiency and performance reasons we apply several filters on the generator level. First, we disable all strong W decays at the generator level and set $BR(\tilde{\chi}_2^0 \to h\tilde{\chi}_1^0) = 100\%$. Furthermore, we also apply the *topAlg.MultiElecMuTauFilter* which excludes hadronic taus and also requires at least 1 lepton with $|\eta| < 2.7$ with $p_T > 15$ GeV. We find that this filter is approximately 66-72% efficient.

For the ATLAS full detector simulations, we use the ATLFAST II software package which employs a number of simplifications to dramatically speed up the hadronization and event reconstruction routines. We used Evgen tag $e1864$, Simul tag $a188$, Atlfast tag $a171$, and Atlfast_merge tag $r3549$ to produce files in the standard ATLAS AOD format [38]. The AOD files are further processed into SUSY NTUP D3PD format

using the $p1512$ tag. This dramatically reduces the size of the AODs and discards raw hits data which is not necessary for the analysis and pre-calculates some common used SUSY analysis variables.

In addition to the pMSSM signal points, we also generate Simplified Model samples where the sleptons and squarks are very massive and are effectively decoupled and play no role in the physics. We also assume the $\tilde{\chi}_2^0$ and $\tilde{\chi}_1^\pm$ are mass degenerate.

In total, we generate nearly 8 million ATLFAST II events for 150 separate grid points (75 for positive chargino and 75 for negative chargino), in a grid that was intentionally selected to be identical to the ones used in the multi-lepton Direct Gaugino SUSY analyses [17]. The grid used for this analysis is shown in Figure 6.6.

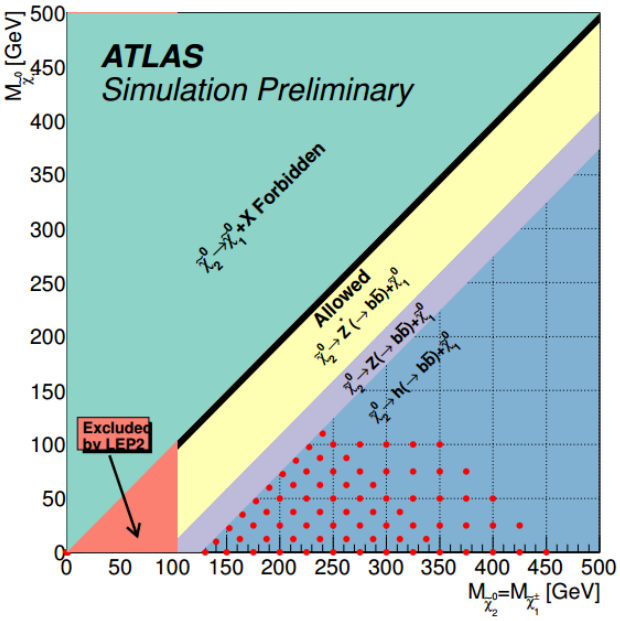

Figure 6.6: The SUSY Simplified Model grid points used in this analysis. Due to the low production cross section, the grid is limited to $m_{\tilde{\chi}_2^0}, m_{\tilde{\chi}_1^\pm} < 450$ GeV and $m_{\tilde{\chi}_1^0} < 100$ GeV.

The corresponding ATLAS dataset numbers are provided in Table 6.3.

Type	Dataset Numbers
$\tilde{\chi}_2^0\tilde{\chi}_1^+$	177282-177316, 179865-179878, 183829-183854
$\tilde{\chi}_2^0\tilde{\chi}_1^-$	177317-177351, 179879-179892, 183855-183880

Table 6.3: ATLAS dataset numbers for the Simplified Model SUSY grid used in this analysis.

Uncertainties on the SUSY signal cross sections are calculated using the SUSYSignalUncertainties tool [44] built by the ATLAS SUSY Working Group. This software package is run on our signal points in order to estimate the theoretical uncertainties on the cross section through the following approach.

- Vary CTEQ[55] PDFs
- Vary MSTW[47] PDFs
- Vary renormalization/factorization scale with CTEQ central value PDF
- Vary renormalization/factorization scale with MSTW central value PDF
- Vary strong coupling using CTEQ PDFs

The uncertainties are found to range from 5-8% with the largest contribution coming from the CTEQ PDFs.

6.3 Standard Model Backgrounds

We use a large number of ATLAS Monte Carlo samples produced as part of the MC12 campaign in order to derive our background estimates for this analysis. The

samples are simulated using either ATLFAST II or the full simulation based on GEANT4 [6]. The Standard Model background in this analysis can be categorized into irreducible (final state identical to the signal) and reducible, some of which are listed below.

Irreducible Backgrounds

- W+jets
- Single top
- WZ
- WH

Reducible Background

- $t\bar{t}$
- Z+jets
- WW
- $Z \to \tau\tau$

The dominant background is $t\bar{t}$, followed by Single Top and W+jets which have a very similar event topology compared to the signal. Some Feynman diagrams for these process are given in Figure 6.7.

Table 6.4 gives an overview of all background samples used in this analysis, including the samples used for evaluating the systematic uncertainties. It is worth noting a couple peculiarities regarding the SHERPA W+jets and Z+jets samples which are

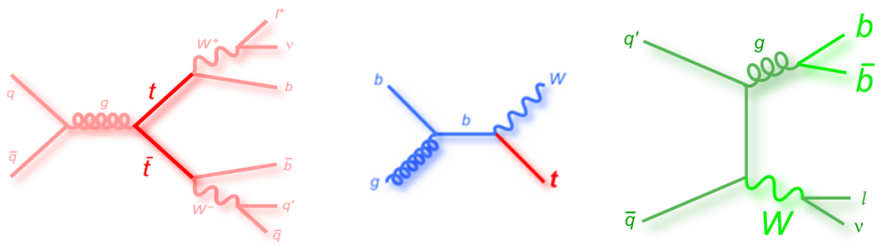

Figure 6.7: Feynman diagrams for the dominant Standard Model backgrounds, $t\bar{t}$, Single top, and W+jets.

produced with massive c and b quarks. These samples are produced over multiple vector boson P_T ranges. The lowest P_T sample is inclusive so we run an overlap removal on the truth level. In order to further boost the heavy flavor statistics, these samples are produced with three exclusive flavor types (b filter, b veto + c filter, b and c veto).

6.4 Data Samples and Triggers

For this analysis, we use the 8 TeV data from the 2012 ATLAS collisions data. All data was processed using the ATLAS Athena framework version 17 using the p1542 data tags. The data collection periods used are periods A through L [8], all from 2012, with a total integrated luminosity of 20.3 fb^{-1} with an uncertainty of 2.8%. The data is derived from the Egamma and Muons physics data streams.

We utilize different sets of triggers for the electron and muon data streams. For the electron channel, we use EF_e24vhi_medium1 or EF_e60_medium1 single electron triggers. For muons, we use the analogous EF_mu24i_tight and EF_mu36_tight single muon triggers. The lower threshold triggers are selected as they are the lowest non-

Process	Generator + fragmentation/hadronisation	Cross-section	Tune	PDF set
Top				
$t\bar{t}$	POWHEG-r2129 + PYTHIA-6.426	NNLO+NNLL	PERUGIA2011C	CT10
	* MC@NLO-4.06 + HERWIG-6.520	NNLO+NNLL	AUET2B	CT10
	* POWHEG-r2129 + HERWIG-6.520	NLO	AEUT2B	CT10
	* ACERMC-38 + PYTHIA-6.426	NNLO+NNLL	AUET2B	CTEQ6L1
Single Top				
t-channel	ACERMC-38 + PYTHIA-6.426	NNLO+NNLL	AEUT2B	CTEQ6L1
s-channel	POWHEG-r2129 + PYTHIA-6.426	NNLO+NNLL	PERUGIA2011C	CTEQ6L1
	* MC@NLO-4.06 + HERWIG-6.520	NNLO+NNLL	AEUT2B	CT10
Wt-channel	POWHEG-r2129 + PYTHIA-6.426	NNLO	PERUGIA2011C	CTEQ6L1
	* ACERMC-38 + PYTHIA-6.426	NLO	PERUGIA2011C	CTEQ6L1
	* MC@NLO-4.06 + HERWIG-6.520	NNLO+NNLL	AEUT2B	CT10
	* POWHEG-r2129 + HERWIG-6.520	NNLO+NNLL	AEUT2B	CT10
Top+Boson				
$t\bar{t}W$, $t\bar{t}Z$	MADGRAPH-5.0 + PYTHIA-6.426	NLO	AEUT2B	CTEQ6L1
$t\bar{t}WW$	MADGRAPH-5.0 + PYTHIA-6.426	NLO	AEUT2B	CTEQ6L1
tW	MC@NLO-4.06 + HERWIG-6.520	NNLO+NNLL	AEUT2B	CT10
tZ	MADGRAPH-5.0 + PYTHIA-6.426	NLO	AEUT2B	CTEQ6L1
Single Boson				
W, Z	SHERPA	NLO	–	CT10
Diboson				
WW/WZ/ZZ	SHERPA-1.4.1	NLO (MCFM)	–	CT10
Single Boson + Higgs				
WH and ZH	PYTHIA8B	LO	AU2	CTEQ6L1

Table 6.4: MC samples used in this analysis for background estimates, the generator type, the order of cross-section calculations used for yield normalisation, names of parameter tunes used for the underlying event generation and PDF sets. Samples marked with asterisks are used for systematic uncertainties.

prescaled single electron and muon triggers. For the matrix method QCD background estimate discussed later in this chapter, it is required to relax our requirements somewhat and we utilize the less isolated lower threshold triggers (EF_e24vh_medium1 and EF_mu24_tight). As the lower-threshold triggers are prescaled in the 2012 runs (only a fraction of the events which pass the trigger are actually written out), events which only pass the lower-threshold trigger are normalized (weighted) by the corresponding trigger prescale.

6.5 Object Definition

In order to do the physics analysis, we must first define the various physics objects that we will cut on or combine to form other variables. For the final state we are considering, there are predominantly electrons, muons, jets, b-tagged jets, and $\not{E}_T$. To do this efficiently, we make use of an existing tool already developed by the ATLAS SUSY Working Group, called SUSYTools-00-03-14 [45], which incorporates many recommendations for ATLAS SUSY analyses.

6.5.1 Electrons

Electron classification and reconstruction is ATLAS is done using a procedure developed by the Egamma Performance Group. For this analysis, the electrons we consider are electron candidates which pass the *medium+* selection [40]. In order to be classified as *medium+*, electron candidates need to meet a stringent set of criteria for ECAL shower shape, HCAL energy leakage, and certain track and cluster matching requirements. On top of this, we apply several selection cuts to obtain our so called "preselected" electrons which are used in the next step of our object definition. In particular, we require $E_T > 10$ GeV and $|\eta| < 2.47$. We also require that the electron reconstruction algorithm used be one that is optimized for higher E_T electrons, so the algorithm *author* must be either 1 or 3. We also use SUSYTools to apply a couple corrections to make the reconstructed result more closely resemble the data. We use the "OQ" object quality flag to remove electrons which are located in areas of the ATLAS detector where there are known issues such as ECAL problems or broken optical transmitters. We also smear the electron energy and rescale it in

order to match the electron resolution that is derived from data. Further E_T and η dependent scale factors are also applied.

From the "preselected" electrons, signal electrons can be selected by using another series of cuts which are motivated by our signal topology which are detailed below in Table 6.5.

Cut	Value
Preselected Electron	
AuthorElectron	1 or 3
Acceptance	$E_T > 10$ GeV, $\lvert\eta^{cl}\rvert < 2.47$
Quality	MediumPP
Cleaning	cut on quality flag el_OQ
Overlap	Accept if $\Delta R(e, jet) > 0.4$ Accept highest E_T electron if $\Delta R(e, e) < 0.1$
Signal Electron	
Quality	Tight++
Acceptance	$E_T >$25 GeV, $\lvert\eta^{cl}\rvert < 2.47$
Isolation	$p_T^{cone}(0.3)/E_T <$0.16 $E_T^{cone,corr}/E_T <$0.18 if $E_T > 30$ GeV, $E_T \equiv$30 GeV
Prompt	$\frac{\lvert d_0\rvert}{\sigma(d_0)} < 5$ $\lvert z_0 \sin\theta\rvert <$ 0.4 mm

Table 6.5: A summary of the electron object definition cuts.

For the isolation requirement, $p_T^{cone}(0.3)$ is the transverse momentum of all other tracks with $P_T >$1 GeV within a code of radius $\Delta R < 0.3$ around the electron track. $E_T^{cone,corr}(0.3)$ is defined as $E_T^{cone}(0.3) - A \times N_{vtx}$ where A = 20.15 MeV in data and 17.94 MeV in Monte Carlo and N_{vtx} is defined as the number of vertices with at least 5 tracks. $E_T^{cone}(0.3)$ is defined similarly to the P_T equivalent. Note, if the E_T in the denominator exceeds 30 GeV, we actually cap it to 30 GeV.

6.5.2 Muons

For muons, we use the recommendations published by the ATLAS Muon Combined Performance Group [42]. For this analysis, we exclusively use muons reconstructed using the STACO algorithm [9]. Both combined and segment tagged muons are used and the P_T of the muon spectrometer and inner detector tracks in MC simulations are smeared before the combination in order to match the muon resolution that is observed in data. We use "loose" quality muons for the preselection with several additional cuts. First, $P_T > 10$ GeV and $|\eta| < 2.40$. Then we require tracks to have at least one hit in the b-layer, at least one Pixel detector hit, and at least 5 hits in the SCT detector. Tracks also must have less than 3 holes in the Pixel and SCT. Lastly, we require a successful TRT extension where applicable using the following technical recommendation:

- $(0.1 < |\eta| < 1.9)$: require $n > 5$ and $n_{TRT}^{outliers} < 0.9 \times n$,
- $(|\eta| < 0.1$ or $|\eta| > 1.9)$: require $n \leq 5$ or $n_{TRT}^{outliers} < 0.9 \times n$,

where $n = n_{TRT}^{hits} + n_{TRT}^{outliers}$, with n_{TRT}^{hits} ($n_{TRT}^{outliers}$) is the number of TRT hits (outliers) on the muon track. As with the electrons, we apply several extra cuts below in Table 6.6 to get the signal muons we use for our event selection.

For the muons, $E_T^{cone,corr}(0.3) = E_T^{CONE}(0.3) - A \times N_{VTX} - B \times N_{VTX}^2$ where A = 64.8 MeV in data and 69.2 MeV in Monte Carlo and B = 0.98 MeV in data and 0.76 MeV in MC.

Cut	Value
Preselected muon	
Algorithm	STACO, combined or segment-tagged muon
Acceptance	$P_T > 10$ GeV, $\|\eta\| < 2.4$
Quality	Loose
ID track quality	$\geqslant 1$ b-layer hit when it can be expected $\geqslant 1$ Pixel hit or crossed dead Pixel sensor $\geqslant 5$ SCT hits or crossed dead SCT sensor Pixel holes + SCT holes < 3 $0.1 < \|\eta\| < 1.9$: $n > 5$ and $n_{TRT}^{outliers} < 0.9 \times n$ $\|\eta\| < 0.1$ or $\|\eta\| > 1.9$: $n \leq 5$ or $n_{TRT}^{outliers} < 0.9 \times n$
Overlap	Accept if $\Delta R(\mu, jet) > 0.4$
Signal muon	
Acceptance	$P_T > 25$ GeV, $\|\eta\| < 2.4$
Quality	Loose
Isolation	$p_T^{cone}(0.3)/E_T < 0.12$ $E_T^{cone,corr}/E_T < 0.12$ if $E_T > 30$ GeV, $E_T \equiv 30$ GeV
Prompt	$\frac{\|d_0\|}{\sigma(d_0)} < 3$ $\|z_0 \sin\theta\| < 0.4$ mm
Cosmic muon veto	$\|z_\mu - z_{PV}\| < 1$ mm, $d_0 < 0.2$ mm

Table 6.6: A summary of the muon object definition cuts.

6.5.3 Jets

To reconstruct jets, topological calorimeter clusters are used with the anti-k_t algorithm [35] with a radius of R = 0.4. Both the Jet Energy Resolution (JER) and Jet Energy scale (JES) are calibrated to correct the calorimeter response to the true jet energy. We use a very basic selection to determine our "baseline" jets:

- $P_T > 20$ GeV

- $|\eta| < 4.5$
- Reject if $VeryLooseBad$ jet in event

$VeryLooseBad$ jets are typically jets which have a poor HEC energy fraction (fraction of energy in ECAL vs HCAL) and low jet quality determined based on the LAr pulse shapes. The removal of events with these jets help to suppress backgrounds from instrumental noise and cosmic muons. The baseline jets are broken down into two categories of signal jets. There are central jets which must meet the criteria:

- $P_T > 25$ GeV
- $|\eta| < 2.4$
- $|JVF| > 0.5$ for jets with $P_T > 50$ GeV

As we have seen previously, the JVF cut is effective at suppressing pileup jets. We use the following definition for forward signal jets:

- $P_T > 30$ GeV
- $2.4 < |\eta| < 4.5$

6.5.4 *b*-jets

For *b*-tagging jets, we use a neural network algorithm known as MV1 which is developed by the ATLAS Flavour Tagging Combined Performance Group. The MV1 algorithm takes as input the output weights from the other flavour tagging algorithms:

- $JetFitter + IP3D$

- $IP3D$
- $SV1$

Based on the multivariate analysis studies done in Section 6.7, we use the 70% efficiency operating point for this analysis which corresponds to a MV1 weight of $>$ 0.7892. These b-tagged jets are reweighted and corrected using data-to-simulation scale factor calibrations for b-jets, c-jets, and mistag rates. The scale factors are used to determine a weight to apply to each jet in an event with $P_T > 20$ GeV and $|\eta| <$ 2.5, and subsequently, a weight for the event as a whole. The weight applied to the whole event is obtained by the product of all the weights of the individual jets in that event. This weight helps to correct the tagging rate in MC simulations to that in data.

6.5.5 $\not{E}_T$

$\not{E}_T$ is calculated using the *MissingETUtility* as recommended by the SUSY Working Group. This package can handle the rescaling and searing of P_T of the objects which are used in the $\not{E}_T$ calculation and can also propagate the systematic uncertainties of these corrections. $\not{E}_T$ is computed using contributions from the energy deposits in the ECAL and HCAL in addition to the MS. These energy deposits are calibrated to their most likely associated physics object. Cells in clusters associated with soft jets (7 GeV $< P_T <$ 20 GeV) are also added and cells not associated with any objects and the P_T of tracks passing track quality criteria (like number of hits and the quality of track fit) but are not otherwise associated with any cluster in the

calorimeters are added into a $\not{E}_T^{CellOut}$ term. The $\not{E}_T$ is then defined as the modulus of the vector sum of the transverse momentum of all of these components.

6.5.6 Overlap Removal

It is necessary to implement overlap removal because sometimes a single object can fall into more than one category. A common example is that most isolated electrons will end up in both the electron and the jet collections where in reality it can only be one or the other. We apply the following rules for removing overlaps in this analysis.

1. $\Delta R(e_1, e_2) > 0.1$: If any two baseline electrons (e_1 and e_2) lie within a distance $\Delta R < 0.1$ of each other, the electron with the lowest cluster E_T (e_1) is rejected.

2. $\Delta R(j, e) > 0.2$: If the distance in ΔR between any baseline jet (j) and any baseline electron (e) surviving Step 1 is less than 0.2, the baseline jet is rejected.

3. $\Delta R(j, e) > 0.4$: If the distance in ΔR between any baseline jet (j) surviving after Step 2 and any baseline electron (e) is less than 0.4, the baseline electron is rejected.

4. $\Delta R(j, \mu) > 0.4$: If the distance in ΔR between any baseline jet (j) surviving after Step 2 and any baseline muon (μ) is less than 0.4, the baseline muon is rejected.

6.6 Analysis Variables

In order to separate SUSY signal from SM background, a number of special analysis variables are computed using the physics objects defined above. These are briefly described here. One of the first variables is $\not{E}_T$ which we directly use, using the $Egamma10NoTau\_RefFinal$ definition. As we can see in Figure 6.8, the $\not{E}_T$ for the signal is much more highly distributed compared to the typical backgrounds. Because we have a $h \to bb$ decay in our signal, it is also possible to reconstruct m_{bb} and cut on that resonance since it is a feature that does not appear on any of the dominant backgrounds.

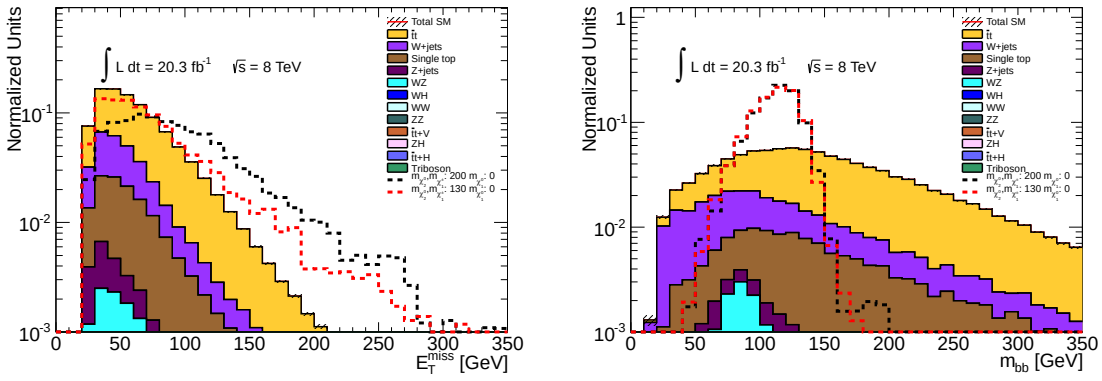

Figure 6.8: Distributions of $\not{E}_T$ and m_{bb} after baseline selection with the integrated distributions normalized to 1.

Another very useful variable we use, m_{CT}, also known as the contransverse mass [59], is particularly effective at eliminating the $t\bar{t}$ background. Originally, this variable was invented to measure the masses of pair-produced semi-invisibly decaying heavy particles at hadron colliders. m_{CT} is defined as:

$$m_{CT}^2(v_1, v_2) = [E_{\mathrm{T}}(v_1) + E_{\mathrm{T}}(v_2)]^2 - [\mathbf{p}_{\mathrm{T}}(v_1) - \mathbf{p}_{\mathrm{T}}(v_2)]^2 \tag{6.1}$$

Here, v_1 and v_2 are the visible particles which in our case are the b-quarks originating from the Higgs decay. At the energies we are working at, the b-quarks can be approximated as massless in which case equation 6.1 simplifies to:

$$m_{CT}^2(v_1, v_2) \approx 2P_T(v_1)P_T(v_2)(1 + \cos\,\Delta\phi) \tag{6.2}$$

If we consider the case of our $t\bar{t}$ background, we find that there is an approximate kinematic endpoint in m_{CT} given by:

$$m_{CT}^{max} = \frac{m_{heavy}^2 - m_{invis}^2}{m_{heavy}} \tag{6.3}$$

In the case of the $t\bar{t}$ background, we find that $m_{heavy} = m_t$ and the two visible particles are the b-tagged jets and $m_{invis} = m_W$, the remainder of the top decay.

$$m_{CT}^{max} = \frac{m_t^2 - m_W^2}{m_t} \approx 135\,\text{GeV} \tag{6.4}$$

Of course, ISR and FSR can smear out this endpoint so a higher cut value needs to be used. In the case of our signal, the distribution of m_{CT} will extend much higher in comparison. In addition to m_{CT}, we also use the transverse mass m_T which is used to used suppress the W+jets background where the jets are $b\bar{b}$. m_T for our decay products is defined as:

$$m_T = \sqrt{2p_T^l \not{E}_T(1 - cos\Delta\phi(l, \not{E}_T))} \tag{6.5}$$

m_T also has an endpoint which works out to be the mass of the semi-leptonically decaying particle. In the case of our W+jets background, this is approximately 80 GeV although again there is a tail due to experimental error and W bosons which are

produced off-shell. In Figure 6.9, the distributions for m_{CT} and m_T are shown after the baseline selection (discussed in section 6.10), showing the discriminating power of these two variables.

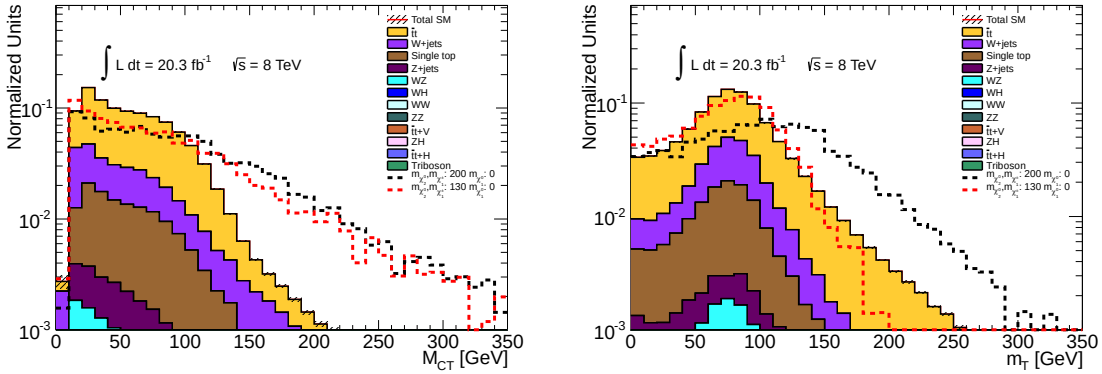

Figure 6.9: Distributions of m_{CT} and m_T after baseline selection with the integrated distributions normalized to 1.

6.7 Multivariate Analysis Studies

Multivariate techniques have become increasingly popular in ATLAS and CMS analysis in the past couple years and can often provide significant benefits over standard cut based analyses. For many analyses, it is difficult to find very powerful discriminating variables and in these cases, considering the variables together is more powerful. Multivariate techniques used generally fall into several categories. The two most commonly used approaches are neutral networks (NN) and boosted decision trees (BDT). In this analysis, we performed some studies using BDTs.

6.7.1 Motivation

While this analysis was ultimately done using a cut-based approach, a multivariate approach was first explored and even though it was not used in the final analysis, the results from the multivariate studies proved to be instructive for guiding the final cut based analysis. While the analysis variables discussed in the previous section do show significant differences between the background and the signal, the analysis is still difficult because at $\sqrt{s}$=8 TeV, the production cross sections for the signals are tiny. A couple representative cross sections are given below in Table 6.7.

$M_{\tilde{\chi}_1^+}$	$M_{\tilde{\chi}_1^0}$	xsec (pb)
130	0	2.458
200	0	0.484
250	0	0.200

Table 6.7: Cross sections for various $\tilde{\chi}_1^+\tilde{\chi}_2^0$ production (positive only).

While a cut based analysis is limited to "square" regions of phase space, using a BDT can better optimize to pick out more signal because it is not subject to such a constraint. The BDT approach can also provide some valuable insight even for a cut based analysis. For example, the TMVA software package provided by ROOT to perform BDT analyses has the ability to rank variables by their discriminating power. This gives useful insight into which variables should be used in a cut-based analysis, although this is sometimes not entirely accurate because it doesn't properly account for highly correlated variables.

For this particular analysis, we are also somewhat sensitive to the b-tagger operating point that is selected. The BDT results can help shed some light on which is the best tagger operating point to use. Finally, doing the BDT analysis gives us a sense of how well our cut based analysis is doing. For example, if the sensitivity is comparable for both, then it makes sense to pursue a cut based approach which is easier to understand and debug.

6.7.2 Boosted Decision Trees

A decision tree is a binary tree where at each node, a yes/no decision is taken on a single variable until a stop criterion, such as the tree depth limit, is reached. A training dataset is used to construct the trees. At each node, the most powerful discriminating variable is selected (so it is possible for the same variable to appear at more than one node in a single tree), and the cut value which gives the best separation between signal and background is used. In each subsequent node, this procedure is repeated. Each ending node is then classified as either signal or background depending on whether the majority of events in that end node is in reality signal or background. A schematic layout of a decision tree is shown in Figure 6.10 [57].

In order to give better stability in the decision trees with regards to fluctuations in the training dataset, a strategy known as boosting is used to enhance the performance compared to a single tree. This is done by giving a higher weight to signal events which are improperly categorized into a background end node. This weighting gives rise to a new training dataset which is then used to generate a new tree. This procedure is repeated over and over again to get a set of trees which is called a forest.

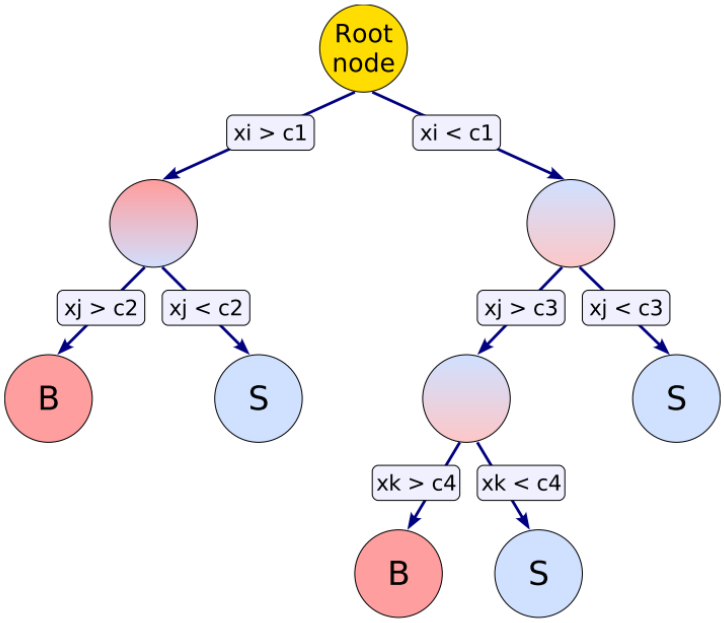

Figure 6.10: A decision tree with a depth of 3. At each node, a binary split is made based on a certain cut value of the most discriminating variable at that step of the event separation.

In a boosted decision tree, the entire forest is used to categorize an event. A single event is run through every decision tree in the forest and a likelihood estimator is constructed based on how often the event ends up in a signal or background end node. The value of this estimator is then cut on to differentiate signal from background events. This procedure improves the classification performance and also gives improved stability against statistical fluctuations.

6.7.3 BDT Analysis Setup

For the BDT Analysis, three representative pMSSM grid points were used. These specially produced datasets had ATLAS dataset numbers 172007-172009 and corre-

spond to M1 and M2 values of {50 GeV, 200 GeV}, {0 GeV, 200 GeV}, and {0 GeV, 150 GeV}. All the background samples are used although in practice, only $t\bar{t}$, W+jets and Single Top significantly contribute. Everything is normalised to 20.3 fb^{-1} with individual event weights applied.

Each signal point is trained individually although we focus on the 172009 point since it has the highest cross section. The testing and training datasets are formed by randomly splitting in half the datasets on an event by event basis. The *Adaboost* boosting technique [60] is used with the following decision tree settings:

- MaxDepth = 4
- PruneStrength = -1
- ForestSize = 100
- Minimum events per node = 10

The MaxDepth means trees can have a maximum of four 'levels' while PruneStrength=-1 means we use the automatic pruning built into TMVA to do the removal of statistically insignificant branches in our trees. The forest size of 100 means when we boost, we only generate 100 trees and the minimum of 10 events per node means we only create a branch at a node when there are at least 10 events that pass through to that node, otherwise we consider it to be an end node.

Over 20 variables are considered originally but over subsequent iterations, we removed the ones which are highly correlated and also ones which have less discriminating power. The variables that we eventually settle on are:

- leadb - A boolean that is true if the leading jet is also a b-jet
- baselepveto - A boolean that is true if there is an extra lepton that passes the baseline selection
- njets - The number of jets that pass the baseline jet selection
- nbjets - The number of jets that pass the baseline jet selection and are also b-tagged
- MET - The $\not{E}_T$ in the event
- b1b2_dR - The ΔR between the two b-jets in the event.
- mHiggs - The invariant mass of the reconstructed bb pair.
- mt - The m_T of the event.
- MetHiggs_dphi - The $\Delta\phi$ between the $\not{E}_T$ and the reconstructed h.
- mct - The m_{CT} in the event.
- WHiggs_dphi - The $\Delta\phi$ between the reconstructed h and the reconstructed W candidate where the W candidate is defined as the $\not{E}_T$+lepton.

The analysis is performed with the b-tagger set at 60%, 70%, and 80% operating points.

6.7.4 Results and Interpretation

The ROOT TMVA package has the ability to rank the input variables by their power for separating signal and background. The ranking of these variables is given below in Table 6.8.

```
: TMVAtest.root:/InputVariables_Id/CorrelationPlots
:
: Ranking input variables (method unspecific)...
: Ranking result (top variable is best ranked)
: ------------------------------------
: Rank : Variable      : Separation
: ------------------------------------
:    1 : mHiggs        : 3.116e-01
:    2 : njets         : 2.798e-01
:    3 : WHiggs_dphi   : 1.731e-01
:    4 : mct           : 1.078e-01
:    5 : leadb         : 7.805e-02
:    6 : b1b2_dR       : 7.178e-02
:    7 : mt            : 4.463e-02
:    8 : MET           : 4.071e-02
:    9 : MetHiggs_dphi : 3.915e-02
:   10 : nbjets        : 2.099e-02
:   11 : baselepveto   : 8.658e-04
: ------------------------------------
```

Table 6.8: The separating power of variables input into the TMVA BDT, with larger value denoting more separating power.

We see the strongest separating variable is the reconstructed Higgs mass which makes a lot of sense because this is something that does not appear even in our irreducible backgrounds. Based on this information, we use this variable and most of the other ones listed above in our cut based analysis which is described in the next section.

In order to do a comparison against cut based approaches, the metric Z_N is utilized. We calculate Z_N using the following RooStats function:

```
double myZn = RooStats::NumberCountingUtils::BinomialExpZ(nsig,nbkg,0.3);
```

Formally, Z_N is defined as

$$Z_N(N_s, N_b, \delta_b) = \sqrt{2}\mathrm{erf}^{-1}(1-2p) \tag{6.6}$$

where p is computed with BinomialExpP which is given by:

```
Double_t BinomialExpP(Double_t signalExp,
             Double_t backgroundExp,
             Double_t relativeBkgUncert)
{
Double_t mainInf = signalExp+backgroundExp;
Double_t tau = 1./backgroundExp/(relativeBkgUncert*relativeBkgUncert);
Double_t auxiliaryInf = backgroundExp*tau;

return = TMath::BetaIncomplete(1./(1.+tau),mainInf,auxiliaryInf+1);
}
```

BetaIncomplete is actually a regularized beta function so

$$p(N_s, N_b, \delta_b) = I(\frac{1}{1+1/(N_b\delta_b^2)}; N_s+N_b; \frac{1}{\delta_b^2}+1) \tag{6.7}$$

The regularized beta function can also be expressed as the CDF (cumulative probability function) of the binomial distribution:

$$I(x; a, b) = \sum_{j=a}^{a+b-1} B(j; a+b-1, x) \tag{6.8}$$

therefore equation 6.7 can be re-expressed as:

$$p(N_s, N_b, \delta_b) = \sum_{j=N_s+N_b}^{N_s+N_b+\frac{1}{\delta_b^2}} B(N_s + N_b + \frac{1}{\delta_b^2}, \frac{1}{1+1/(N_b\delta_b^2)}) \tag{6.9}$$

This could be understood to mean the probability of getting at least $N_s + N_b$ after conducting $N_s + N_b + \frac{1}{\delta_b^2}$ trials where the probability of success for each trial is $\frac{1}{1+1/(N_b\delta_b^2)}$. The quantity $N_s + N_b$ can be understood to be the number of signal and background events in our signal region. The number of events in the control region is extrapolated. If we assume that δ_b arises solely from the statistical uncertainty, then the number of events in the CR is roughly $1/\delta_b^2$ so the total number of trials (adding SR and CR) is as determined above, $N_s + N_b + \frac{1}{\delta_b^2}$. Now if we go to the background only hypothesis (no signal), then the probability for an event to end up in the signal region is $(N_s + N_b)/(N_s + N_b + 1/\delta_b^2)$, and when we set $N_s = 0$, we get $\frac{1}{1+1/(N_b\delta_b^2)}$ which is the probability of success used above.

Thus, Z_N is tied to the approximate probability of finding at least $N_b + N_s$ events in the SR and is a reasonable value to use for analysis optimization. Higher values of Z_N indicate more sensitivity to the signal hypothesis we are trying to test. However, to test the performance of the BDT, we do not solely concentrate on maximizing Z_N because we need to take into account the fact that a high Z_N with a miniscule N_s doesn't make so much sense because from an experimental standpoint, we can't measure a fraction of an event (and also because equation 6.8 actually assume a and b are integer values). Thus, we calculate Z_N after optimizing cut on the BDT output value to give us around 10 signal events.

Using the 70% b-tagger operating point and assuming $\delta_b = 30\%$ (this is a rough estimate of the total uncertainties we expect from this analysis after looking at other comparable ATLAS SUSY analyses), we are able to obtain the results given in Table 6.9.

Sample	Number of Events
172009 (Signal)	10.03
Single Top	2.89
$t\bar{t}$	6.00
W+jets	1.70
WW	0.35
Z+jets	0
Higgs	0.70
Total Background	11.65
$Z_N = 1.54$	

Table 6.9: The Z_N achieved by the basic BDT analysis.

This is a quick result that was accomplished without going through all of the optimization steps typical in a BDT analysis, but nevertheless it gives a good sense of what is possible if this analysis is done using a BDT approach. The Z_N that was achieved turns out to be quite similar to the results from the initial cut based approach that was developed in parallel to the BDT analysis. As a result of the similar results, a decision was made to do the full analysis using the cut based approach due to the increased familiarity with the methods and a better understanding of the proper rigorous statistic treatment for a standard cut based analysis.

However, the BDT approach was instructive in determining which are the most interesting variables to look at and it also helped to quickly demonstrate that relatively

good sensitivity should be possible for this analysis. We were also able to use the BDT analysis to guide us regarding which b-tagger operating point should be used for the cut based analysis. To do this study, we relaxed the cut on the BDT output variable (to avoid issues with low statistics fluctuations and the BDT becoming overtrained) and computed Z_N for the 60%, 70%, and 80% b-tagger operating points, again keeping the number of signal events after BDT cut constant. The results are shown below in Table 6.10

b-tagger operating point	Z_N
60%	0.498
70%	0.509
80%	0.451

Table 6.10: The Z_N at different b-tagger operating points.

We see that the results for 60% and 70% are comparable but we do get a decrease in performance when moving to 80%. Based on this information, the 70% b-tagger operating point is the obvious choice because it has equivalent sensitivity to the 60% b-tagger but has the benefit of having more statistics.

6.8 Analysis Strategy

Our analysis strategy is a cut-based approach and in this and the following sections, we discuss how this analysis is carried out starting with the analysis framework and software, the event selection, the method of Standard Model background estimation, and finally the systematic uncertainties that we need to consider.

On a high level, the first step of the analysis strategy is to define signal regions (SR) which are regions of the kinematic phase space which are signal enriched. Such regions can be derived by closely investigating the unique aspects of the event kinematics of the signal process in question. Ideally, one wants to get a SR which only contains signal. However, it is not possible to get a 100% pure SR, thus it becomes important to estimate the background contamination in the SR.

To do this in a data driven way, control regions (CR) must be defined. A control region is a region of kinematic space which is enriched in one of the dominant background processes. The best CRs are designed to have high purity in just one type of background and should be as purely background as possible (i.e. free of signal contamination). The way SRs and CRs are used to estimate the background is described in more detail in Section 6.14.2.

6.9 Analysis Framework and Software

This analysis was done using the ProofANA analysis framework [46] which provides a robust development environment for producing analyses that run over ntuples such as the SUSY D3PDs [20] that we use. A chief advantage is its object-oriented event data model which allow the same analysis to be run over various different data sources (which may have different format and variable names) without needing to rewrite the core analysis code. Through a series of configuration files, filelists, and run scripts, all processing is "scheduled" in advance and automatically parallelized across multiple cores. ProofANA is also portable and the same code that is run locally on local

CPU cores can also be run on clusters or even on the Grid. A schematic of a typical ProofAna analysis chain is shown below in Figure 6.11.

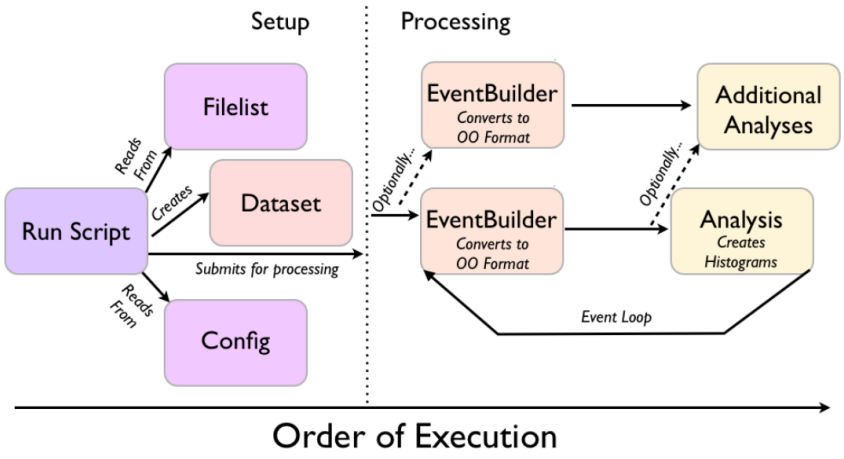

Figure 6.11: ProofANA components and how they interface to run a complete analysis.

In this analysis we also make use of the SUSYTools package that is developed by the ATLAS SUSY working group [45]. This tool serves as an interface to many common C++ classes and functions which implement many of the important corrections, bug fixes, and tweaks which are provided by the various ATLAS physics performance groups. SUSYTools is used extensively by almost all SUSY searches within ATLAS and is a way of ensuring a consistent treatment of corrections among all analysis groups.

6.10 Event Preselection

Before we begin the signal selection, we apply a number of cleaning and quality cuts in order to establish a good baseline dataset prior to cutting to sort events into the SRs, CRs, and VRs. The list below gives a summary of the cuts which are used for this analysis.

- Data Quality Good Run List - We use the data12_8TeV_DetStatus-v61-pro14-02 Good Run List (GRL) in order to reject events from luminosity blocks where problems were reported in one or more ATLAS detector.
- Trigger - We use the triggers described previously in Section 6.4
- Vertex Quality - We only use reconstructed events which have a good primary vertex, the requirement is at least 5 tracks must be associated with the primary vertex of the event.
- LAr and Tile Cleaning - We reject events with $larError == 2$ or $tileError == 2$. These are the standard recommendations to compensate for LAr detector noise burst and data corruption in the Tile calorimeters.
- Tile trip - We reject events with the bad tile cal flag.
- TTC resets - Incomplete events which are caused by a TTC problem preventing the event from being fully written to the buffer are removed by vetoing coreFlags&0x40000! = 0.
- Dead Tile Cells - We veto events that have jets which satisfy the following conditions: $P_T > 40$ GeV, $B_{jet}^{corr} > 0.05$ and $\Delta\phi(j,\not{E}_T) < 0.3$. This is effi-

cient at removing events that are impacted by non-operational cells in the tile calorimeter and events where the $\not{E}_T$ come from the HEC hole.

- Jet Cleaning - Events are rejected if any of the jets with $P_T > 20$ GeV satisfy the VeryLooseBad jet definition [41].

- Muons Cleaning - Events are rejected if they contain preselected muons with $\frac{\sigma_{q/p}}{|q/p|} > 0.2$ (q is charge, p is momentum) in order to veto events where the $\not{E}_T$ potentially comes from fake muons or mismeasured muons.

- Cosmic Muons - Events are discarded if there is a preselected muon (after overlap removal) with a longitudinal impact parameter $|z_0| > 1$ mm or a transverse impact parameter $|d_0| > 0.2$ mm in order to suppress potential cosmic background.

- Electron/muon overlap - Events with preselected electrons and muons which survive the overlap removal detailed in Section 6.5.6 are also vetoed if $\Delta R(e, \mu) < 0.1$

- Muon/muon overlap - Events with preselected muons which survive the overlap cuts of Section 6.5.6 and the above cut are vetoed if $\Delta R(\mu, \mu) < 0.05$.

- Trigger-matched lepton - At least one lepton in each event should be matched to the trigger within a cone of $\Delta R < 0.15$.

6.11 Signal Selection

Our signal grid actually varies widely and there is a large range of different $\tilde{\chi}_2^0$ and $\tilde{\chi}_1^0$ mass splittings which leads to different kinematic properties in the low and high splitting regions. Therefore, two separate signal regions are utilized in order to optimize for each type of kinematics, these are discussed in more detail in Section 6.11.2.

To help define these signal regions and ensure that they are as pure as possible with little background contamination, the following cut variables are used:

- $\not{E}_T$ - This is used to reduce all backgrounds, in particular QCD and $t\bar{t}$.
- Exactly 2 b-tagged jets - This is used to reduce W+jets.
- Leading jets are b-tagged jets - This is used to reduce $t\bar{t}$.
- Veto additional leptons - This is used to reduce $t\bar{t}$ which decays dileptonically.
- Fourth jet veto - This is used to reduce $t\bar{t}$ that decays semileptonically or completely hadronically.
- m_{CT} - As discussed earlier this is effective at reducing $t\bar{t}$ due to the kinematic endpoint which exists at ≈ 135 GeV.
- m_T - This is used to reduce semi-leptonic W backgrounds.
- m_{bb} - This is used to reduce all backgrounds that contain $b\bar{b}$ which are not from Higgs.

6.11.1 Optimization Strategy

We define two signal regions, SRA and SRB which are optimized for different $\tilde{\chi}_2^0$ and $\tilde{\chi}_1^0$ mass splittings. The low mass splitting region is SRA and it is optimized for $m_{\tilde{\chi}_2^0} - m_{\tilde{\chi}_1^0} < 175$ GeV while SRB is the high mass splitting region that is optimized for $m_{\tilde{\chi}_2^0} - m_{\tilde{\chi}_1^0} > 175$ GeV.

To optimize the signal regions, we again used the metric Z_N which was also used in our BDT studies. As before, an uncertainty of 30% is applied as the uncertainty on the Standard Model background prediction. To perform the optimization, the cut value of the above variables are varied to maximize the value of Z_N. In this optimization procedure, different signal grid points are selected in order to separately optimize both low and high $\tilde{\chi}_2^0$ and $\tilde{\chi}_1^0$ mass splitting regions.

6.11.2 Signal Regions

For the signal regions, the main variables for optimization are m_{CT}, m_T, and $\not{E}_T$. We find that for both signal regions, the fourth jet veto is helpful along with requiring exactly two b-tagged jets and just a single signal lepton. Using the $105 < m_{bb} < 135$ GeV window also helps to increase sensitivity. Due to smearing of the m_{CT} kinematic endpoint by ISR and FSR, we cut well above the 135 GeV kinematic endpoint at 160 GeV. $\not{E}_T > 100$ GeV is found to be optimal for both signal regions. We differentiate SRA and SRB with different m_T cuts which are made to be orthogonal so there is no overlap between the two SRs. For SRA, we require $100 < m_T < 130$ GeV and for SRB we use $m_T > 130$ GeV. The summary of the SR definitions is shown below in

Table 6.11 and Figure 6.12.

Cut	SRA	SRB
Number of b-jets	Exactly two b-tagged jets (MV1 @ 70%)	
Jet kinematics	b-tagged jets are leading jets	
Jet Veto	No fourth-leading jet with P_T 25 GeV	
Lepton	Exactly one signal and baseline lepton	
$\not{E}_T$	> 100 GeV	
m_{CT}	> 160 GeV	
m_{bb}	$105 < m_{bb} < 135$ GeV	
m_T	$100 < m_T < 130$ GeV	> 130 GeV

Table 6.11: The final selection cut values for SRA and SRB after optimization. All preselection and event cleaning cuts are also applied before these final sets of cuts.

6.12 Standard Model Background Measurement

As described in more detail in Section 6.3, the dominant backgrounds in this search are $t\bar{t}$, W+jets, and single top with smaller contributions from WH and Standard Model QCD. The QCD backgrounds can sometimes be mistaken as signal due to the misidentification of objects as leptons. The impact of these fake lepton QCD events is studied in Section 6.12.2. As for the other non-QCD background, they are estimated directly from Monte Carlo or using a control region to signal region extrapolation with the control regions described in Section 6.12.1.

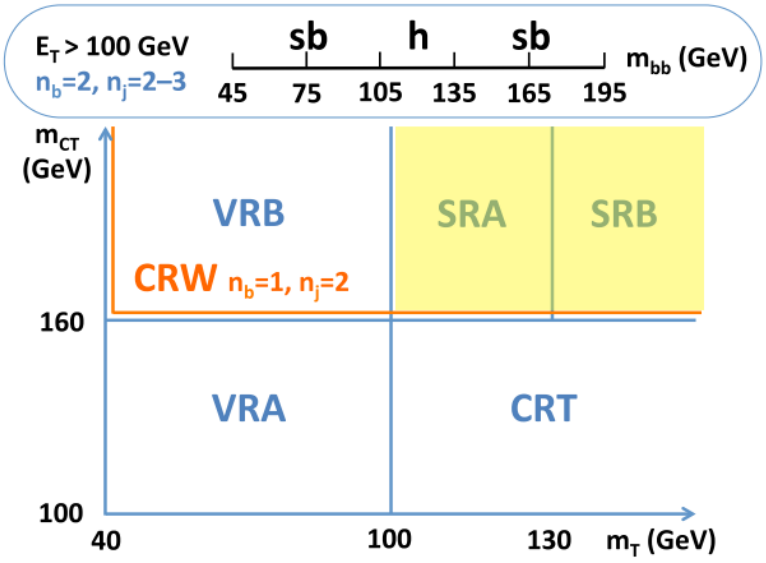

Figure 6.12: In yellow, the signal region (SR) definitions as a function of m_T and m_{CT}. The kinematic regions of the validation regions (VR) and control regions (CR) are also shown. The VRs and CRs will be discussed in more detail later.

6.12.1 Control Regions

We define two control regions, CRT and CRW which target $t\bar{t}$ and W+jets respectively. The cuts used to define these regions are given below:

- CRT - This control region is almost identical to SRA and SRB to remain as kinematically similar as possible. As with the SRs, we apply a cut of $m_T > 100$ GeV and also require a maximum of 2 b-jets and veto events if they contain a 4th baseline jet with $P_T > 25$ GeV. However, for CRT, we allow the $t\bar{t}$ events which are lost as a result of the m_{CT} cut by relaxing that cut to 100 GeV $< m_{CT} <$ 160 GeV.

- CRW - Because we want to keep $t\bar{t}$ out of this control region, we restore the

$m_{CT} > 160$ GeV cut. However, because W+jets events should only have one b-jet, the b-tagged jet requirement is relaxed to 1. We also reduce the total number of baseline jets in the event to no more than 2 in order to reject additional $t\bar{t}$ which tends to have more jets. Finally, we decrease the m_T cut to $m_T > 40$ GeV so that we can get more W+jets statistics.

The control regions are shown schematically in Figure 6.13.

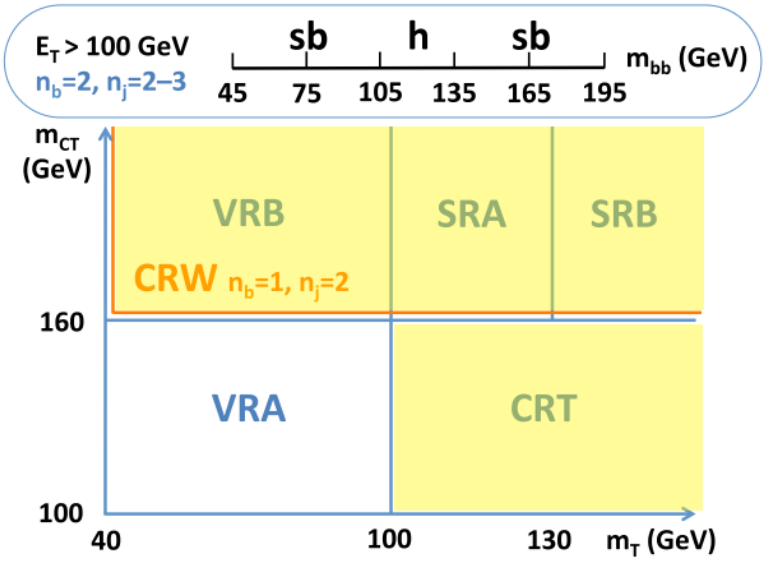

Figure 6.13: The control regions (CRs) definitions as a function of m_T and m_{CT}.

As will be discussed in more detail in Section 6.14, when we do our SR and CR fit, we actually bin in m_{bb}. Thus, we need to bin our CRs and SRs, into 5 bins of 30 GeV starting from $m_{bb} = 45$ GeV until $m_{bb} = 195$ GeV. As mentioned previously, we define our SR as just the middle "higgs" bin of $105 < m_{bb} < 135$ GeV but for the fit, we also have to define so called "sideband" regions which have all other SR cuts held

the same except they are binned in 30 GeV m_{bb} windows in the range $45 < m_{bb} < 105$ GeV and $135 < m_{bb} < 195$ GeV. The full range used for all SRs (including the "sb" regions) and CRs is approximately 5σ around the most probable value of the Higgs peak which is at 120 GeV with a fitted standard deviation of ≈ 15 GeV. The SR "sb" regions are never blinded and are only used to further constrain the fit so in effect, these regions act more like control regions despite being called signal regions. We will also denote the "sb" regions as SRAsb, SRBsb, while the signal regions themselves can also be denoted as SRAh and SRBh.

Finally, we define another region for QCD fake lepton events that is used as a validation region for the matrix method QCD background estimate described in Section 6.12.2. For this region, we require:

- One baseline lepton
- At least 2 central jets (but a maximum of 3 central + forward jets)
- $m_{bb} > 45$ GeV
- $\not{E}_T > 50$ GeV

Based on the results of Section 6.12.2, this section isn't used in any of the fits performed later to derive the Standard Model background estimate.

6.12.2 QCD Background Estimate

To estimate the impact of the fake lepton QCD events, we use the so called matrix method which is described in more detail in [33]. Here, we give an overview of the

method. The goal is to get an estimate of the rate at which fake lepton QCD events can pass our selections for the CRs and SRs.

For the matrix method, we define four types of leptons:

- Tight (T) - Tight leptons are signal leptons which pass all of our lepton cuts.
- Loose (L) - Loose leptons are baseline leptons which only pass the baseline lepton selection.
- Real (R) - Real leptons are actual leptons.
- Fake (F) - Fake leptons are jets or other non-lepton objects which are accidentally reconstructed as leptons.

These quantities are related through the following set of linear equations:

$$\begin{pmatrix} N_T \\ N_L \end{pmatrix} = \begin{pmatrix} \epsilon & f \\ (1-\epsilon) & (1-f) \end{pmatrix} \cdot \begin{pmatrix} N_R \\ N_F \end{pmatrix} \tag{6.10}$$

Here ϵ and f are the real lepton efficiency, and the fake rate. We can solve this system of equations for N_F (eliminating the variable N_R which is unknown). Multiplying the result by f gives us the number of fake leptons passing the tight cuts:

$$N_{F\to T} = \left(\frac{f}{\epsilon - f}\right)(\epsilon \times N_L - N_T + \epsilon \times N_T) \tag{6.11}$$

Therefore, if we know ϵ, f, and the number of loose and tight leptons passing our selection, the fake contribution in the tight selection region can be estimated. N_L

and N_T can be simply counted, but ϵ and f need to be derived from data. The real lepton efficiencies are known to be rather sample independent so we can use ATLAS reference numbers which are derived from data (Z boson decays) and MC simulations. Fake rates however tend to depend a lot on the specific analysis kinematics and must be specially derived for our selection. The rates also depend quite a bit on P_T and η and must be parameterized based on those two quantities. Thus, when we derive the QCD fake estimate, events must be reweighted on an event by event basis. This is done using equation 6.11 as well, except now N_L is always 1 and N_T is either 0 or 1 depending on whether that event passes the tight cuts.

To carry out this matrix method implementation, we make use of the ATLAS software package FakeLeptBkg-00-01-13 which provides the reference real electron/muon efficiencies. To calculate the fake rates for our selection, we use a special set of cuts on both data and our Monte Carlo background samples:

- One or more loose lepton
- At least 2 b-tagged jets
- $\not{E}_T < 25$ GeV (To selected QCD and reject everything else)
- $m_T < 40$ GeV (To selected QCD and reject everything else)
- require fourth-leading jet $P_T < 25$ GeV

These cuts are in effect reversing most of our usual selection cuts to specifically pick out QCD (as opposed to rejecting QCD). In this region, we subtract the MC real lepton yields from the data yields and then what remains is considered to be the

fakes. To get the rate, for each P_T and η bin, we take the ratio of events passing tight lepton requirements to those passing loose lepton requirements. The results we derived for electrons is shown below in Table 6.12

P_T (GeV)	η						
	0 - 0.8	0.8 - 1.37	1.37 - 1.52	1.52 - 2.01	2.01 - 2.19	2.19 - 2.37	2.37 - 2.47
25 - 30	0.12 ± 0.01	0.13 ± 0.01	0.10 ± 0.04	0.16 ± 0.2	0.13 ± 0.04	0.21 ± 0.05	0.10 ± 0.02
30 - 40	0.12 ± 0.01	0.10 ± 0.01	0.08 ± 0.02	0.16 ± 0.02	0.15 ± 0.04	0.15 ± 0.03	0.11 ± 0.02
40 - 50	0.10 ± 0.03	0.13 ± 0.03	0.05 ± 0.02	0.12 ± 0.03	0.10 ± 0.06	0.22 ± 0.08	0.08 ± 0.03
50 - 60	0.06 ± 0.05	0.20 ± 0.05	0.08 ± 0.03	0.22 ± 0.07	0.27 ± 0.11	0.08 ± 0.08	0.07 ± 0.04
60-70	0.10 ± 0.03	0.08 ± 0.02	0.07 ± 0.03	0.06 ± 0.02	0.16 ± 0.06	0.07 ± 0.03	0.05 ± 0.04
>70	0.14 ± 0.03	0.07 ± 0.02	0.03 ± 0.01	0.09 ± 0.02	0.07 ± 0.02	0.10 ± 0.03	0.04 ± 0.02

Table 6.12: The rate of fake electrons faking tight electrons in our QCD enriched sample as a function of P_T and η.

For muons, comparable rates cannot be so easily derived because our overlap removal for muons succeeds in removing most fakes so there aren't enough statistics in the fake region. Because the fake rate is expected to be much lower, this also means the impact of fakes is less and its less important to derive the fake rates perfectly. As a result, we use the muon fake rates which are provided in the FakeLeptBkg-00-01-13 package which are for heavy flavor samples which is what most of our background consists of anyways. Using these fake rates in Figure 6.14, we can see the fake contribution in the QCD validation region we defined in the previous section.

We see that there is excellent data and MC agreement within the error bars which gives us confidence in the results. Furthermore, we also notice that the QCD fake contribution is about two orders of magnitude smaller than the dominant $t\bar{t}$ background. This contribution should stay small given that in our CRs and SRs, we

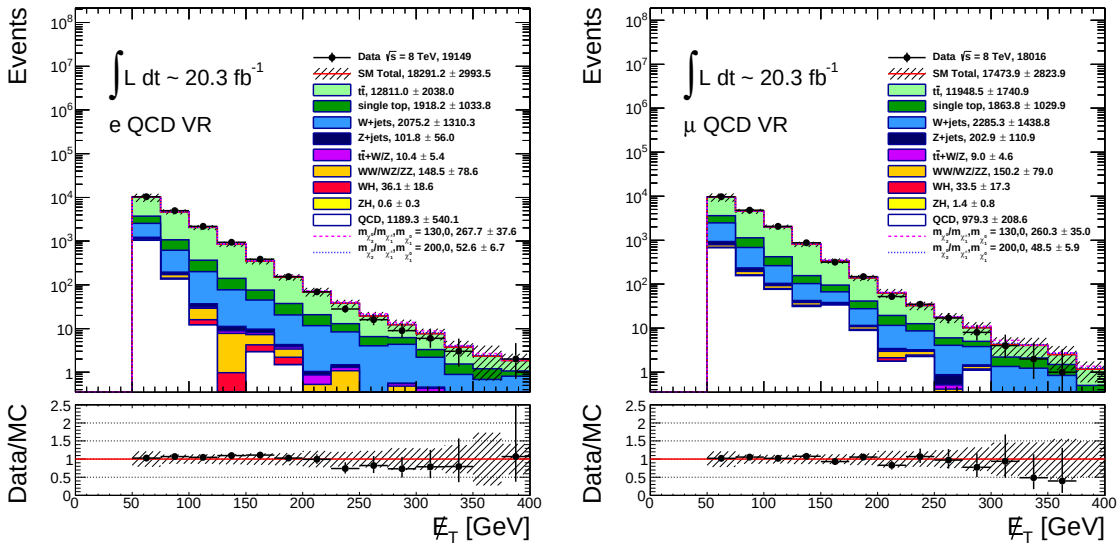

Figure 6.14: $\not{E}_T$ distributions in our QCD validation region with estimated fake contribution for electrons (left) and muons (right).

have a $\not{E}_T > 100$ GeV requirement which should be good at suppressing QCD fakes. Table 6.13 shows that at least in the CRs and VRs, the amount of QCD fakes never exceeds 3% and in the SRs, we actually estimate there to be basically zero QCD fakes.

QCD Estimate for Control and Validation Regions			
Region	QCD (MM)	Non-QCD (MC)	QCD/Non-QCD (%)
CRT	16.0 ± 8.9	527.31 ± 98.46	3.0
CRW	50.3 ± 14.6	1689.46 ± 81.78	3.0
VRA	21.0 ± 10.5	802.96 ± 62.16	2.6
VRB	4.0 ± 3.9	240.80 ± 21.43	1.7

Table 6.13: QCD fake contribution in CRs and VRs using the matrix method. For the SRs, there is actually no statistics so we consider the QCD fake contribution in those regions to be zero. Even if there were statistics, we would expect the QCD fake contribution in the SRs to be even lower than in the CRs.

Thus, the QCD fake contribution is well below the other backgrounds, and in fact even significantly lower than the expected cumulative systematic uncertainties from the other backgrounds so in this analysis, QCD can be ignored without danger. For simplicity, we drop this potential source of background from the analysis.

Even though we are able to drop QCD fakes from this analysis, we do one other adjustment in order to improve the analysis and get better data and MC agreement in our background estimates. It is known that in $t\bar{t}$ enriched regions, there is a discrepancy between Powheg $t\bar{t}$ and data. This was also observed in the ATLAS $h \to b\bar{b}$ analysis [30] and as a result, we also apply the same reweighting that was applied there in order to get slightly better data/MC agreement.

With this, all of the pieces necessary to do an accurate Standard Model background estimate are in place and we use this to do the statistical fits described in Section 6.14.

6.13 Systematic Uncertainties

We consider two categories of systematic uncertainties, experimental uncertainties arising from the ATLAS instrumentation and theoretical uncertainties arising from theoretical models and generator deficiencies. Systematic uncertainties are directly passed into the fit and can have a large impact on results so in this analysis, we expended much effort on being as thorough as possible.

6.13.1 Experimental Uncertainties

The experimental uncertainties arising from the ATLAS detector are now relatively well understood so for this analysis as we are able to benefit from nearly two years of experience from working on ATLAS 8 TeV datasets. The uncertainties we consider here are largely common to most other ATLAS SUSY Working Group analyses so we use the common SUSYTools-00-03-14 tool to evaluate them. The general strategy is to build one or two variations to the nominal quantity and evaluate the difference between the variation and the nominal as the systematic uncertainty. The following uncertainties are evaluated:

- Pileup - In order to account for uncertainties with our pileup reweighting, we scale $< \mu >$, the average number of interactions per bunch crossing, by 0.9 prior to pileup reweighting to get one variation while the unscaled $< \mu >$ is the nominal.

- Jet Energy Scale (JES) - The jet energy scale is reweighted up and down by its 1σ uncertainty calculated by the Jet/Etmiss group.

- Jet Energy Resolution (JER) - To account for the possible underestimate of the actual JER, the P_T of jets is smeared based on the jet P_T and η.

- Jet Vertex Fraction (JVF) - As discussed earlier, the JVF is a cut used to suppress pileup that is applied to all of the central jets in this analysis with $P_T < 50$ GeV. To calculate the systematic uncertainty, we vary it up or down by 1σ using the JVFUncertaintyTool.

- Electron Reconstruction Efficiency - We use a multiplicative scale factor to account for data/MC differences in electron reconstruction efficiency. For the systematic, we vary this scale factor up and down by 1σ.

- Electron Trigger Efficiency - Again, we vary the data/MC correction scale factor up and down by 1σ.

- Electron Resolution - The electron resolution correction factor and the MET_RefEle term in MC are scaled up and down by 1σ.

- Electron Energy Scale - The electron energy scale is scaled up and down by 1σ using the separate uncertainties derived from $Z \to ee$ (used for calibration), the presampler scale, detector material, and low P_T electrons, which we treat separately and assume are uncorrelated.

- Muon Reconstruction Efficiency - The scale factor used to account for data/MC differences in muon reconstruction efficiency is scaled up and down by the 1σ uncertainty.

- Muon Trigger Efficiency - The muon trigger scale factor is scaled up and down by its 1σ uncertainty.

- Muon MS and ID momentum - The muon momentum resolution scale factor for MS and ID muons are separately scaled up and down by their 1σ uncertainties.

- Muon Energy Scale - The muon energy scale is scaled up and down by its 1σ uncertainty.

- $\not{E}_T$ - There are energy scale and resolution uncertainties on the CellOut term used to compute $\not{E}_T$. We scale the term up and down by 1σ.

- b-tagging efficiency - The MV1 b-tagging algorithm has scale factors dependent on η, P_T, the operating point, and flavor. We vary these scale factors separately for b, c, and light jets and get three uncorrelated systematic uncertainties.

- Luminosity - We apply a 2.8% uncertainty on the integrated luminosity as calculated from ATLAS beam-separation studies.

These systematics are varied independently in our fit (described in Section 6.14) and their correlations are taken into account. The full correlation matrix for the systematics can be found in reference [14].

6.13.2 Theoretical Uncertainties

We evaluate theoretical uncertainties by comparing MC samples at reconstructed level, with the exception of the factorization and normalization of $t\bar{t}$ which is evaluated using MC samples at truth level. Theoretical uncertainties can impact both the background normalization and also the shape of kinematic distributions which can both impact the background prediction in the signal regions. The following systematic theoretical uncertainties are considered:

$\mathbf{t\bar{t}}$

- Generator - The uncertainty on how well the generator models the physics is derived by comparing POWHEG+JIMMY with MC@NLO+JIMMY and comparing the yields and symmetrizing.

- Parton Shower - The uncertainty in how well parton showers are modelled is derived by comparing POWHEG+PYTHIA and POWHEG+JIMMY. We take the difference in the yield and symmetrize.

- ISR/FSR - We use dedicated ACERMC+PYTHIA "MorePS" and "LessPS" samples. We take the difference in the yield and symmetrize.

- Factorization and Renormalization scales - We use the POWHEG+PYTHIA sample and vary the renormalization and factorization scales by 2x and 0.5x the nominal values and evaluate the systematic uncertainty as

$$\Delta_{scale} = \frac{N^{up} - N^{down}}{N^{up} + N^{down}} \tag{6.12}$$

- PDF - For all CRs and SRs, we add an uncertainty from the PDF. Since the nominal $t\bar{t}$ uses the CT10 PDF, we evaluate the 52 error sets in CT10 by reweighting each event using the PDF reweighting tools provided by the LHAPDF software package. The uncertainty is derived by looking at the maximum difference from the nominal PDF yield.

$t\bar{t}V$

- A flat 22% uncertainty is used for the production cross section based on recommendations from the ATLAS SUSY Working Group Background Forum.

W+jets

- Number of partons - We use samples with 4 partons, so we compare with samples with additional partons and we take the difference in the yield and symmetrize.

- Scale variations - We follow the procedure used by the ATLAS SUSY 0-lepton inclusive analysis [36] for the uncertainty related to the choice of factorization and renormalization scales in SHERPA MC samples. Basically the ALPGEN scale variations are applied to SHERPA based on the number of truth jets with $P_T > 30$ GeV.

- PDF - We use the same prescription as used for $t\bar{t}$ using the 52 CT10 error sets.

Z+jets

- PDF - We use the same prescription as used for $t\bar{t}$ using the 52 CT10 error sets.

Diboson

Due to low statistics in our systematics samples, we derive the uncertainties for this region by using an expanded region with ≥ 1 b-jet, $m_T > 40$ GeV, $\not{E}_T > 100$ GeV, $m_{CT} > 100$ GeV, and $45 < m_{bb} < 195$ GeV.

- Number of partons - The nominal samples are compared with samples with up to 3 extra partons and we take the difference in the yield and symmetrize.

- Scale variations - The nominal samples are compared with samples where the renormalization and factorization scales varied up and down by 0.5x and 2x.

- PDF - We use the same prescription as used for $t\bar{t}$ using the 52 CT10 error sets.

Single Top Systematic

For the single top systematics, we consider three separate single top channels, s, t, and Wt and we evaluate the systematics for each component channel. For the t and

s channels, there are insufficient statistics in the CRs and SRs so the systematics are also derived in the expanded region described above for dibosons and then applied to all regions. We evaluate the following systematics:

- ISR/FSR - We use ACERMC+PYTHIA samples with ISR/FSR increased and decreased from the nominal to derive a systematic using the difference in yields.
- Generator + Parton Shower (s-channel) - We compare POWHEG+PYTHIA with MC@NLO+JIMMY and derive the systematic based on the difference in yields.

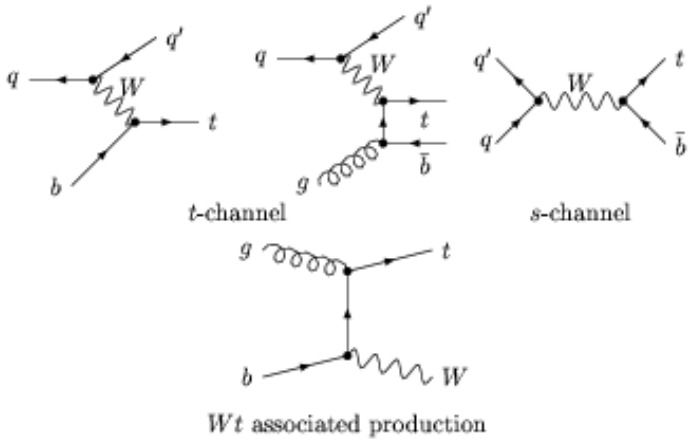

Figure 6.15: Feynman diagrams for the 3 types of Single top production at the LHC.

Generator, Parton Shower, and $t\bar{t}$ interference (Wt-channel) For the Wt mode single top, at LO, the process is actually relatively well defined. However, at NLO, there is interference with top pair production, especially if the invariant mass of the final state W and b approaches the top mass. Figure 6.16 shows some of the NLO real emission contributions to Wt.

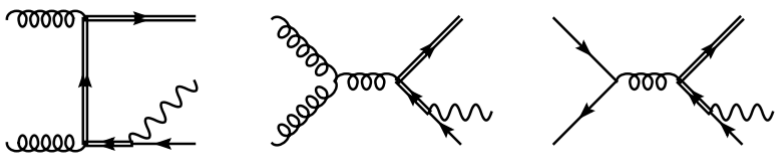

Figure 6.16: Feynman diagrams for some NLO real emission contributions to Wt production.

We need to estimate the uncertainty that arises from this potential interference. We produce an estimate for this uncertainty, along with the Wt uncertainty on generator and parton shower, by making several comparisons.

The first is to compare the POWHEG+PYTHIA NLO samples for Wt and $t\bar{t}$ with the LO production of WWbb using AcerMC. We use the so called Process 14 and Process 20 samples which correspond to the following channels:

- Process 14: $q + q \to WWbb$
- Process 20: $g + g \to WWbb$

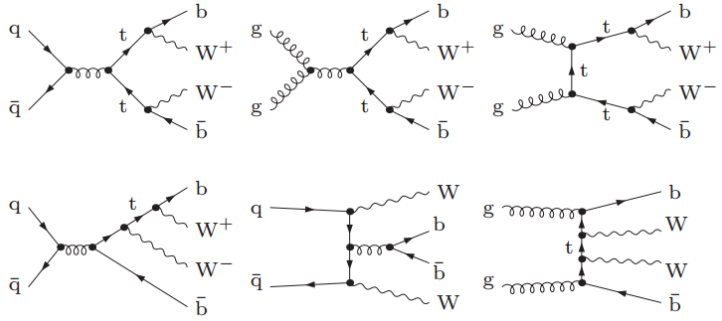

Figure 6.17: Some Feynman diagrams for the WWbb production we use for the comparison [29].

Our nominal POWHEG+PYTHIA Single top samples utilize the Diagram Removal scheme in which diagrams which include a $t\bar{t}$ pair are excluded. Thus the interference term with LO $t\bar{t}$ production is removed. Taking the ACERMC LO cross sections directly leads to a roughly factor of 2 normalization difference with the POWHEG+PYTHIA samples. Thus we apply a k-factor of 1.925 to ACERMC which allows us to compare POWHEG+PYTHIA Wt+$t\bar{t}$ with Process 14+20.

Secondly, we compare MC@NLO+JIMMY Wt+$t\bar{t}$ with POWHEG+JIMMY Wt+$t\bar{t}$. And thirdly, we compare POWHEG+PYTHIA Wt+$t\bar{t}$ with POWHEG+JIMMY Wt+$t\bar{t}$. Together with the ATLAS SUSY Working Group Background Forum, we decided to estimate the total Wt uncertainty for generator, parton shower, and interference to be the maximum of the first and second comparison, with the third comparison added in quadrature.

6.14 Statistical Fitting Methodology

In the preceding sections, the blueprint of the analysis has been laid out and the essential components defined. This provides everything that is needed to generate results. However, for these results to be useful, they must be derived from a statistically reliable approach. In this section, the statistical techniques used by the ATLAS SUSY working group for new physics discovery and limit setting are described. First a general overview of these methods is given, while in Section 6.14.1, the profile log likelihood ratio method endorsed by ATLAS and used in this analysis is described. In Section 6.14.2, the way this method is applied to this analysis is described while

Section 6.14.3 describes how the systematic uncertainties described in Section 6.13 are treated under the profiled likelihood method. This sets the context for the discussion of the analysis results which follows later in Section 6.16.

A critical component of the statistical analysis of ATLAS results is whether an observation is "significant" or not. This is quantified using something known as a p-value which is defined as the probability of getting a certain experimental outcome or one that is more extreme than the one observed. Thus, we can express the p-value as an integral over a probability density function $f(t)$, with the integration starting at the observed value of t where t is the test statistic as shown in equation 6.13. In a most basic analysis, the test statistic is simply the number of events in the signal region.

$$p = \int_{t_{obs}}^{\infty} f(t)dt \tag{6.13}$$

Particle physics experiments are counting experiments, and the outcome of an experiment is simply the number of events which fall within the signal region(s). As each event is independent (the event can either pass or fail the selection cuts), the number of events follows a binomial distribution. The physics processes that are searched for are exceedingly rare, so the probability for a given event to be in the signal region is quite low so we can go to the limit where the binomial distribution can be approximated as Poissonian, so the probability of observing n events when ν events are expected for a specific hypothesis H_0, is given by

$$p(n|\nu) = \frac{\nu^n}{n!}e^{-\nu}. \tag{6.14}$$

For a discovery search, the null hypothesis H_0 is always the Standard Model prediction (so in our case, for a given signal region, the expected number of SM background events) while the alternative hypothesis H_1 is the Standard Model plus the SUSY model being tested. To claim a discovery, we require a p-value of less than 2.87×10^{-7}. This means if the H_1 hypothesis is false, only one experiment in 3.5 million would lead to this result due to statistical fluctuation.

In the case of no discovery, it is still possible to get very interesting physics results. Limits can be set which can potentially exclude large swaths of the underlying SUSY model parameter space and these constraints can guide further theoretical developments and experiments. Limits are usually set in the context of a 95% confidence level. When a quantity (such as a production cross section) is excluded at the 95% CL, it means that given a value of the quantity in the exclusion region, the probability of seeing the data that we see, is only 1 in 20, which is a much lower standard than is applied to claim discovery.

6.14.1 Profiled Likelihood Method

Now that we have generally described significance and confidence levels, we can take a closer look at the Profiled Likelihood Method used in ATLAS. In our binned experiment, we can express the expected value (of the number of events) in each bin i as

$$E(n_i) = \mu s_i + b_i \tag{6.15}$$

where s is the number of expected signal events and b is the expected number of background events. In our likelihood, the parameter value we are interested in is μ. $\mu = 0$ would correspond to a background only hypothesis while $\mu = 1$ is the nominal SUSY+SM hypothesis. The likelihood function can thus be constructed as

$$L(\mu) = \prod_{i=1}^{N} \frac{(\mu s_i + b_i(\theta))^{n_i}}{n_i!} e^{-(\mu s_i + b_i(\theta))} \tag{6.16}$$

where N is the total number of bins. Here, θ are nuisance parameters which impact the value of b. The most probable value of μ, which is also known as the signal strength, can be found by maximizing this likelihood function. In order to test a null hypothesis value of μ against an alternative hypothesis, we construct the likelihood ratio

$$\lambda(\mu) = \frac{L(\mu, \hat{\hat{\theta}}(\mu))}{L(\hat{\mu}, \hat{\theta})}. \tag{6.17}$$

Here, the denominator is a maximum likelihood where $\hat{\mu}$ and $\hat{\theta}$ are the true MLEs (maximum likelihood estimators), with their values having been chosen to maximize the likelihood function. The numerator is the profile likelihood function where $\hat{\hat{\theta}}$ is chosen to be the value which maximizes L for some given (hypothesized) value of μ. It follows that $\hat{\hat{\theta}}$ depends on μ and the nuissance parameters have been "profiled". The possible values of λ ranges from 0 to 1, where $\lambda = 1$ means the hypothesized μ agrees very well with $\hat{\mu}$ implying good agreement between the data and the hypothesis. The hypothesis of $\mu = 0$ is used to test for discovery while a hypothesis of $\mu = 1$ is used

for exclusion.

As shown by the Neyman-Pearson Lemma, the log likelihood ratio is the most powerful test statistic so we define our test statistic as

$$t_\mu = -2ln\lambda(\mu). \tag{6.18}$$

This test statistic has a certain probability distribution function $f(t_\mu|\mu)$ for a given value of μ. In order to calculate the p-value, the distribution of the test statistic must be known. This distribution can be derived through psuedo experiments which randomize the number of observed events and the central value of the nuisance parameters. However, according to Wilks' theorem, when the statistics of the data sample is high enough (on the order of $O(10)$ events), the distribution of t follows a χ^2 distribution. In this asymptotic limit, the CPU intensive generation of pseudo experiments to determine the distribution of the test statistic can be avoided. With the distribution of the test statistic, the p-value can now be calculated from

$$p_\mu = \int_{t_{\mu,obs}}^{\infty} f(t_\mu|\mu)dt_\mu \tag{6.19}$$

where $t_{\mu,obs}$ is the value of the test statistic that was observed in data. For setting a 95% CL limit, equation 6.19 is also used, but now we set $p_\mu = 0.05$ and find the value of the signal strength μ, which satisfies the equation.

To exclude signal models however, we actually need to use a modified p-value known as CL_s which is normalized to the background only probability. This addresses the problem of a possible exclusion of the background only model in the case of a

downward statistical fluctuation. In this case, a downwards fluctuation can result in a observation that is much smaller than expected, and outside of the background only model's 95% CL, leading to an unrealistic limit that is much better than the experimental sensitivity.

We define the quantity CL_b as the probability of having a test statistic t_μ that is larger than the observed value of $t_{\mu,obs}$ in the background-only hypothesis. Thus, in the data, μ is set to 0, but for our test statistic, μ is equal to 1 since we are trying to exclude the null hypothesis $s + b$.

$$CL_b = \int_{t_{1,obs}}^{\infty} f(t_1|\mu s + b = b)dt_1 \tag{6.20}$$

We define CL_{s+b} in a similar fashion, but here we assume $s + b$ in the data, i.e. the nominal signal hypothesis. Here, $\mu = 1$ for the assumed value in the data distribution.

$$CL_{s+b} = \int_{t_{1,obs}}^{\infty} f(t_1|s + b)dt_1 \tag{6.21}$$

CL_s is then constructed as

$$CL_s = \frac{CL_{s+b}}{CL_b} \tag{6.22}$$

and in order to exclude a signal at 95% CL, it is required to have $CL_s < 0.05$. The CL_s method is a fundamentally conservative approach. Because CL_b is always less than or equal to 1, CL_s will always be larger than or equal to CL_{s+b}. What the CL_s method does is introduce a penalty for signal models which we are not supposed to be sensitive to as in this case, the CL_b will also be small.

6.14.2 Fit Setup

In order to do the profiled likelihood fit for this analysis, the HistFitter-00-00-36 software package is used [43]. This section details the fit setup used in this analysis. HistFitter is developed by the ATLAS SUSY Working Group and makes use of the HistFactory package in ROOT which is a tool to build parameterized Probability Density Functions (PDF) based on ROOT histograms stored within an XML file. Since 2012, HistFitter has been the standard statistical tool used in searches for supersymmetric particles performed by ATLAS.

Histfitter performs a fit to data assuming a statistically independent CR and SR which allows for modeling the regions using separate PDFs which are combined into a simultaneous fit. During the fit to the data, the observed background event counts in the CRs are used to generate normalization factors for the background processes, and this normalization is used to scale the background prediction in all regions, including the SRs. Generally, the background predictions are derived from Monte Carlo simulations. The factors used to normalize each background process between the CRs and SRs are calculated using [34]:

$$N_p(SR, est.) = N_p(CR, obs.) \times [\frac{MC_p(SR, raw)}{MC_p(CR, raw)}] \tag{6.23}$$

where $N_p(SR, est.)$ is the SR background estimate for each simulated physics process p we are considering, and $N_p(CR, obs.)$ is the observed number of data events in the CR for the process, and $MC_p(SR, raw)$ and $MC_p(CR, raw)$ are raw and unnormalized estimates of the contributions from the process to the SR and CR respectively,

which are obtained from MC simulations. Just like we saw earlier with the Z+Jet analysis described in the previous chapter, here we are able to benefit from the systematic uncertainties on the predicted background processes being cancelled as a result of using the ratio of Monte Carlo estimates. The consequence of this is that it is important to pick CRs with looser selection cuts in order to get a higher event count and reduce the size of the statistical uncertainties.

For the fit setup used in this analysis, we exploit the $h \to \bar{b}b$ resonance expected in the signal shown in Figure 6.18. When fitted with a Crystal Ball fit, the width is found to be approximately 15 GeV with a peak at 120 GeV.

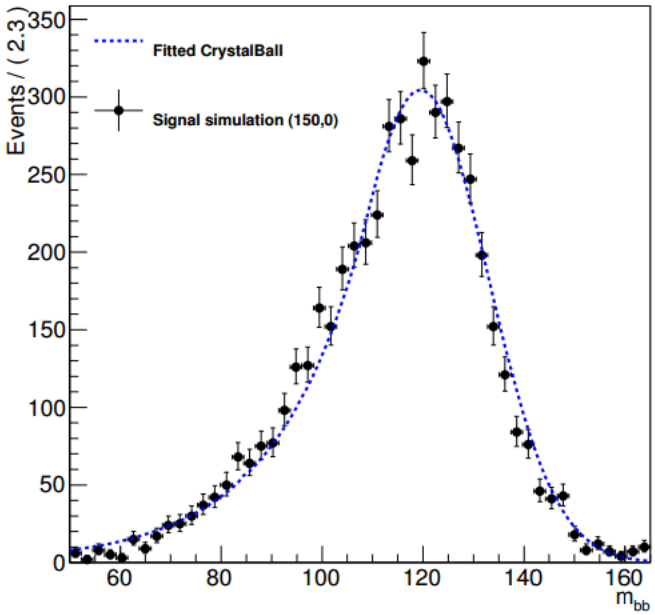

Figure 6.18: Fit of a Crystal Ball to signal sample in a region with exactly 2 b-tagged jets and no additional jets, $\not{E}_T$ >100 GeV and m_T >40 GeV

To exploit the resonance which is rather unique to this SUSY channel, we actually bin the SRs and CRs described above into 5 bins:

- 50 GeV $< m_{bb} <$ 75 GeV (side-band, "sb")
- 75 GeV $< m_{bb} <$ 105 GeV (side-band, "sb")
- 105 GeV $< m_{bb} <$ 135 GeV (higgs sensitive bin, "h")
- 135 GeV $< m_{bb} <$ 165 GeV (side-band, "sb")
- 165 GeV $< m_{bb} <$ 195 GeV (side-band, "sb")

For the initial background only fit, we fit using CRT and CRW and only the signal region side-band bins (SRAsb and SRBsb). After unblinding, the background only fit is performed with all SR bins included. The unblinding procedure is discussed in more detail in Section 6.15.

6.14.3 Treatment of Systematic Uncertainties

In a profiled likelihood method, the systematic uncertainties are treated as nuisance parameters, as they are parameters which are not of immediate interest, but must be accounted for in the analysis of parameters which are of interest (such as the signal strength). These nuisance parameters are approximated to be Gaussian distributed, and they are fitted simultaneously as the likelihood is maximized. The background predictions are allowed to vary within the size of the systematic uncertainties and also constrained by the data. Thus, the measurement itself helps to determine the size of the systematic uncertainties. For example, if observed and expected are relatively similar, the fitted systematic uncertainties will be less than the input systematic uncertainties, while if expected and observed differ significantly, the fitted systematic

uncertainties will be larger to partially account for this effect, hereby reducing the significance of the observed signal. In this sense, the systematic uncertainties reflect the loss of information about the true value of μ.

The HistFitter package (discussed in Section 6.14.2) has several built in ways of treating systematic uncertainties which we make use of in this analysis. In particular:

- **overallSys** - Uncertainties in the global normalization which are agnostic to the shape of the distribution
- **normSys** - overallSys that is constrained to conserve the total event count in a collection of regions
- **histoSys** - correlated uncertainty of shape and normalization
- **OneSide** - One sided uncertainty (e.g. a systematic that only has an up variation)
- **OneSideSym** - An one sided uncertainty which has been symmetrized.

The classification of all experimental and theoretical uncertainties in this analysis are given below:

- **Pile-up** - overallNormHistoSys
- **JES** - overallNormHistoSys (up and down variations are treated as a spectrum shape variation)
- **JER** - overallNormHistoSys (up and down variations are treated as a spectrum shape variation)

- ***b*-tagging** - overallNormHistoSys (spectrum shape variation and mid-identification scale factors treated together)
- **Leptop energy and resolution** - overallHistoSys
- **Leptop trigger and reconstruction** - overallHistoSys
- $t\bar{t}$ **theoretical uncertainties** - overallNormHistoSysOneSideSym
- W**+jets theoretical uncertainties** - overallNormHistoSys
- W**+jets theoretical uncertainties (ISR/FSR)** - overallNormHistoSysOneSideSym
- **Single top theoretical uncertainties** - OverallSys
- **Cross section uncertainties** - OverallSys

6.15 Validation

A crucial part of our analysis strategy is the validation of the model that is used to predict the background contamination in our SRs. An underlying assumption made is that the extrapolation of the normalization factors from the CRs to the SRs is valid. In order to validate this, validation regions (VR) are defined, usually in the kinematic regions between the CRs and SRs. After the fit, the changes made to the input PDFs are extrapolated to the VRs and this serves as a reasonable test because the VRs are not used to constrain the fit. If there is good agreement between the normalized background prediction and observed data in the VRs, then the background

prediction can be safely extrapolated to the SRs. Only after the fit has been validated do we compare the extrapolations in the SRs with the observed data. This process is called "unblinding" the analysis and is done so that premature SR predictions cannot accidentally bias the experimenter.

6.15.1 Validation Regions

The validation regions used in this analysis are shown schematically in Figure 6.19 and also given below in Table 6.14. As we have done for the signal and control regions, we enforce the requirement of $m_{jj} > 45$ GeV also in the validation regions in order to avoid biases coming from the discrepancy in low m_{jj} events between the Sherpa and Alpgen W+jets samples. We define our first validation region VRA the same as CRT except we use the lower m_T region. VRB uses the same m_T range as VRA except this time the m_{CT} is shifted higher like in the signal regions.

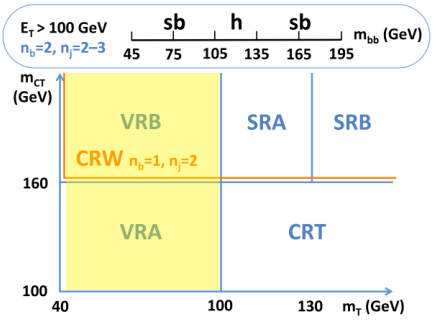

Figure 6.19: In yellow, the validation region (VR) definitions as a function of m_T and m_{CT}. The precise selection cuts used are given in Table 6.14

Selection	VRA	VRB
n_{jets}	2–3	2–3
$n_{b-\text{jets}}$	2	2
m_{CT} (GeV)	100–160	> 160
m_T (GeV)	40–100	40–100

Table 6.14: Summary of signal, control and validation region definitions.

6.15.2 Fit Validation

Using the fit methodology described in the previous sections, we first perform a blinded background only fit where the control regions, CRT and CRW are fitted simultaneously with the side-bands of SRA and SRB, and the fit results are extrapolated into VRA and VRB. The fit results are shown below in Table 6.15.

In the above table, and all subsequent tables and plots, all single top samples (s-channel, t-channel, and Wt-channel) have been grouped into single top and negligible backgrounds (Z+jets, WH, and ZH) are also grouped together. The uncertainties shown are a combination of the statistical and systematic uncertainties. By construction, these uncertainties are symmetric around the central value, and to avoid negative yields, the errors are truncated so the minimum event yield is zero.

From the fit, it is possible to derive the normalization factors for the $t\bar{t}$ and W+jets backgrounds which are given below in Table 6.16. The scale factor, μ, is the constant factor that we multiply the Monte Carlo samples by in order to bring them into agreement with data. It is found in the fit that the $t\bar{t}$ and W+jets normalization factors have a -0.39 correlation which makes sense given the composition of the control regions. CRT is a relatively pure $t\bar{t}$ region while CRW has a relatively even mix of

table.results.yields channel	CRT	CRW	SRAsb	SRBsb	VRA	VRB	SRAh	SRBh
Observed events	651	1547	14	10	885	235	4	3
Fitted bkg events	642.01 ± 24.93	1558.04 ± 38.65	13.05 ± 2.40	8.81 ± 1.65	880.44 ± 85.54	245.19 ± 17.21	5.96 ± 1.29	2.77 ± 0.79
Fitted $t\bar{t}$ events	607.29 ± 25.27	676.62 ± 56.91	8.00 ± 2.44	3.10 ± 1.38	684.79 ± 85.57	141.01 ± 17.88	3.82 ± 1.22	1.36 ± 0.67
Fitted W+jets events	11.13 ± 1.60	693.78 ± 59.83	2.66 ± 0.48	1.73 ± 0.32	99.18 ± 11.85	62.22 ± 8.44	0.58 ± 0.27	0.24 ± 0.13
Fitted Single top events	19.51 ± 3.54	111.47 ± 13.83	1.86 ± 0.58	2.48 ± 1.11	80.00 ± 9.62	27.20 ± 3.76	1.27 ± 0.36	0.71 ± 0.37
Fitted Diboson events	2.25 ± 0.35	64.44 ± 7.65	0.33 ± 0.11	1.10 ± 0.15	10.20 ± 1.48	8.99 ± 1.01	0.00 ± 0.00	0.21 ± 0.04
Fitted Other events	1.84 ± 0.29	11.73 ± 1.00	0.20 ± 0.04	0.40 ± 0.09	6.28 ± 0.56	5.76 ± 0.46	0.29 ± 0.04	0.24 ± 0.05
MC exp. SM events	547.96 ± 101.78	1703.17 ± 90.93	11.23 ± 3.27	7.79 ± 2.00	830.35 ± 71.49	241.95 ± 25.62	4.98 ± 1.69	2.24 ± 0.94
MC exp. $t\bar{t}$ events	511.65 ± 100.95	636.62 ± 93.49	5.83 ± 3.09	2.01 ± 1.55	617.17 ± 60.99	124.85 ± 23.76	2.79 ± 1.49	0.90 ± 0.75
MC exp. W+jets events	13.73 ± 1.59	880.52 ± 2.60	3.19 ± 0.55	2.18 ± 0.41	123.04 ± 9.15	76.63 ± 7.68	0.67 ± 0.39	0.30 ± 0.20
MC exp. Single top events	18.69 ± 3.78	111.59 ± 15.13	1.66 ± 0.58	2.14 ± 1.10	74.92 ± 13.81	26.16 ± 4.05	1.24 ± 0.40	0.60 ± 0.35
MC exp. Diboson events	2.05 ± 0.45	62.80 ± 8.72	0.36 ± 0.17	1.07 ± 0.16	9.40 ± 1.98	8.73 ± 1.18	0.00 ± 0.00	0.21 ± 0.05
MC exp. Other events	1.85 ± 0.32	11.63 ± 1.21	0.19 ± 0.05	0.40 ± 0.10	6.00 ± 0.73	5.57 ± 0.57	0.27 ± 0.05	0.23 ± 0.05

Table 6.15: The expected number of background events in each control region (CRT, CRW), signal region (SRAsb, SRBsb, SRAh, SRBh) and validation region (VRA, VRB) as defined in the text. The numbers are derived from Monte Carlo before and after the blinded background only fit done using HistFitter.

$t\bar{t}$ and W+jets. Thus, a downward fluctuation of CRW will be compensated by an upwards fluctuation of CRT. For the MC backgrounds that are not floated in the fit, we simply use the MC estimate as our background estimate.

Sample	Scale Factor (μ)
$t\bar{t}$	1.03 ± 0.15
W+jets	0.79 ± 0.07

Table 6.16: The background normalizations derived from the blinded background only fit. Errors are both statistical and systematic combined.

Figure 6.20 shows the "pull" distribution for VRA and VRB which is used to test the validity of the transfer-factor extrapolation. If the background model is well estimated, there should be good agreement between the data and the background estimated by our background model.

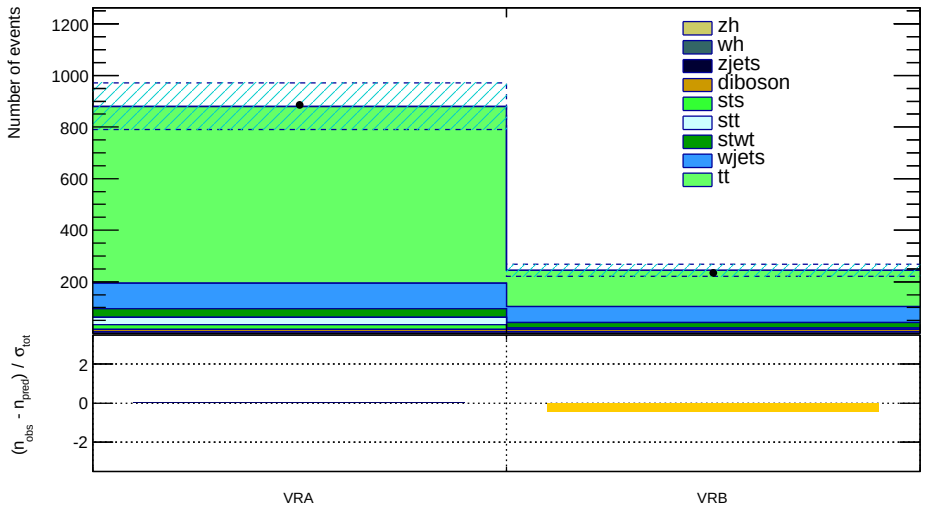

Figure 6.20: The distribution of data and background estimate in VRA and VRB for the blinded background only fit. The data is the black dots in the plot.

Table 6.17 shows the size of all the systematic uncertainties from the background

estimates for all regions, broken down by systematic. Individual uncertainties have correlations which can be negative so the total uncertainties are not simply derived through a quadratic sum of all individual uncertainties.

Figures 6.21 - 6.24 show the distributions for $\not{E}_T, m_T, m_{CT}$, and m_{bb} after fit in CRT, CRW, VRA, and VRB.

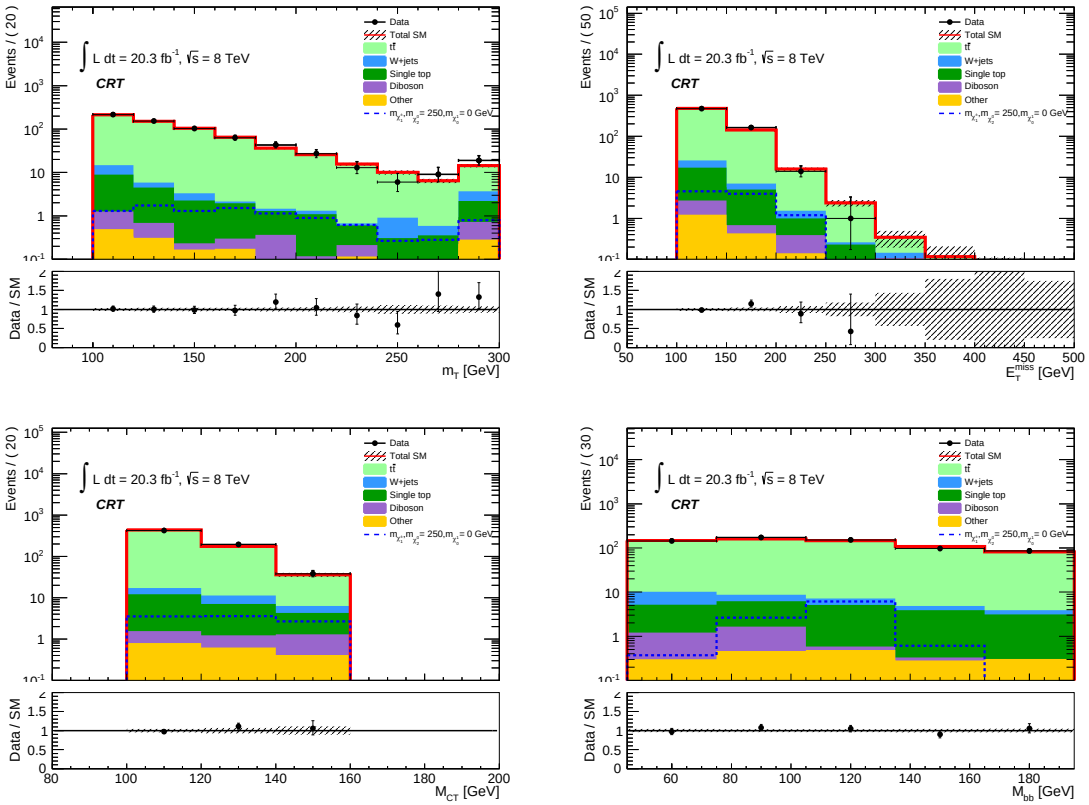

Figure 6.21: Distribution of data and background estimate in CRT for the blinded background only fit. The data is the black dots in the plot and all systematics are included.

Region	CRT	CRW	SRAsb	SRBsb	VRA	VRB	SRAh	SRBh
Total background expectation	642.02	1558.04	13.05	8.81	880.45	245.19	5.96	2.77
Total statistical ($\sqrt{N_{\text{exp}}}$)	±25.34	±39.47	±3.61	±2.97	±29.67	±15.66	±2.44	±1.66
Total background systematic	±24.93 [3.88%]	±38.65 [2.48%]	±2.40 [18.36%]	±1.65 [18.71%]	±85.54 [9.72%]	±17.21 [7.02%]	±1.29 [21.71%]	±0.79 [28.53%]
$t\bar{t}$ factorization scale uncertainty	±0.57	±0.36	±1.08	±0.41	±13.93	±0.24	±0.51	±0.18
$t\bar{t}$ generator uncertainty	±35.14	±35.68	±2.62	±1.50	±38.65	±14.13	±1.25	±0.66
$t\bar{t}$ parton shower uncertainty	±79.94	±61.19	±0.69	±0.42	±7.94	±11.83	±0.33	±0.19
$t\bar{t}$ renormalization uncertainty	±1.25	±0.78	±0.73	±0.12	±22.79	±0.96	±0.35	±0.05
$t\bar{t}$ ISR/FSR uncertainty	±30.37	±22.32	±0.88	±0.33	±9.46	±1.44	±0.42	±0.15
$t\bar{t}$ Normalization Uncertainty	±85.74	±95.53	±1.13	±0.44	±96.69	±19.91	±0.54	±0.19
Theoretical W+jet Uncertainties	±0.58	±0.57	±0.19	±0.14	±5.20	±4.68	±0.05	±0.02
W+jets Normalization Uncertainity	±0.96	±59.97	±0.23	±0.15	±8.57	±5.38	±0.05	±0.02
Single top Wt-channel generator+interference Uncertainty	±1.51	±5.30	±0.38	±1.05	±1.87	±1.49	±0.25	±0.31
Single top Wt-channel Parton Shower Uncertainty	±2.42	±8.19	±0.20	±0.03	±0.45	±1.75	±0.13	±0.01
Theoretical s and t-channel Single top Uncertainties	±0.28	±2.16	±0.03	±0.01	±3.35	±0.55	±0.02	±0.00
Jet Energy Scale	±28.28	±21.67	±0.56	±0.42	±22.77	±1.68	±0.38	±0.38
Jet Energy Resolution	±0.85	±0.09	±0.13	±0.05	±2.31	±1.00	±0.06	±0.11
B-tagging Scale Factors	±13.19	±10.01	±0.72	±0.37	±24.68	±14.21	±0.36	±0.12
Muon Instrumental Uncertainties	±0.92	±1.49	±0.07	±0.18	±1.00	±0.36	±0.08	±0.03
Electron Instrumental Uncertainties	±2.99	±2.85	±0.17	±0.10	±3.50	±1.13	±0.16	±0.09
PDF Uncertainity	±5.97	±5.37	±0.07	±0.05	±6.74	±1.85	±0.10	±0.06
Shape Uncertainity	±0.00	±0.00	±0.74	±0.65	±0.00	±1.09	±0.50	±0.34
Other	±8.12	±15.35	±0.48	±0.23	±6.09	±2.58	±0.23	±0.13

Table 6.17: Systematic uncertainties breakdown for all regions after the blinded fit.

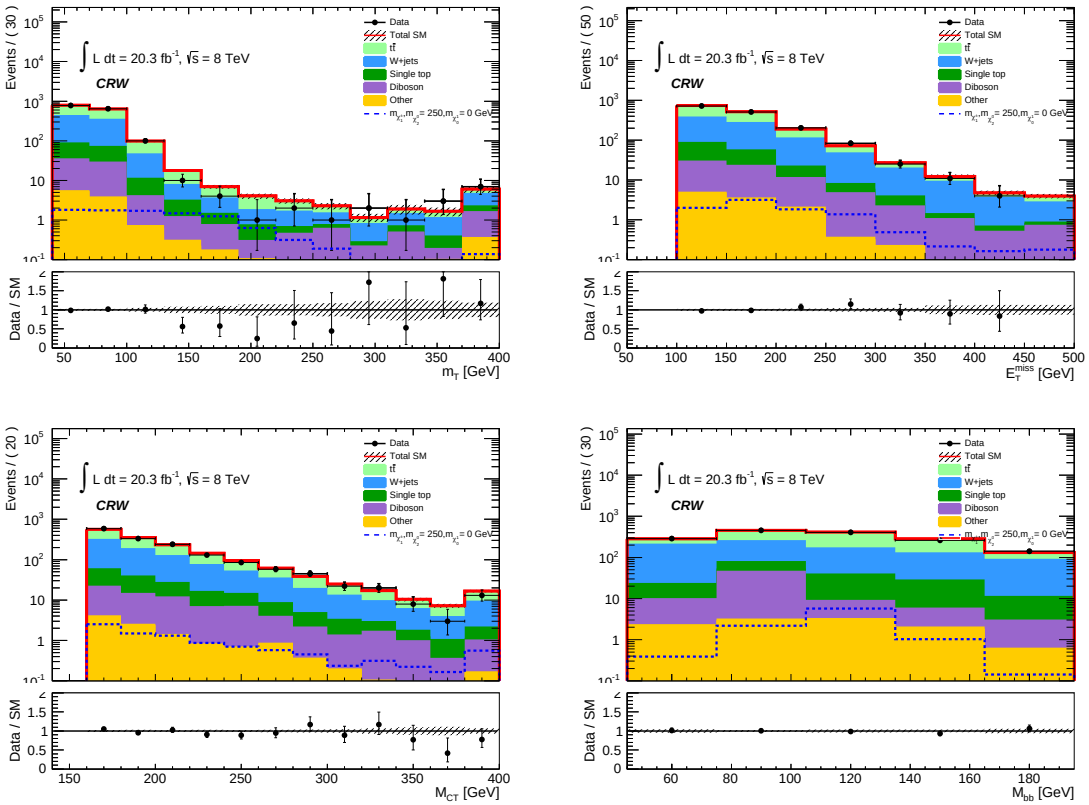

Figure 6.22: Distribution of data and background estimate in CRW for the blinded background only fit. The data is the black dots in the plot and all systematics are included.

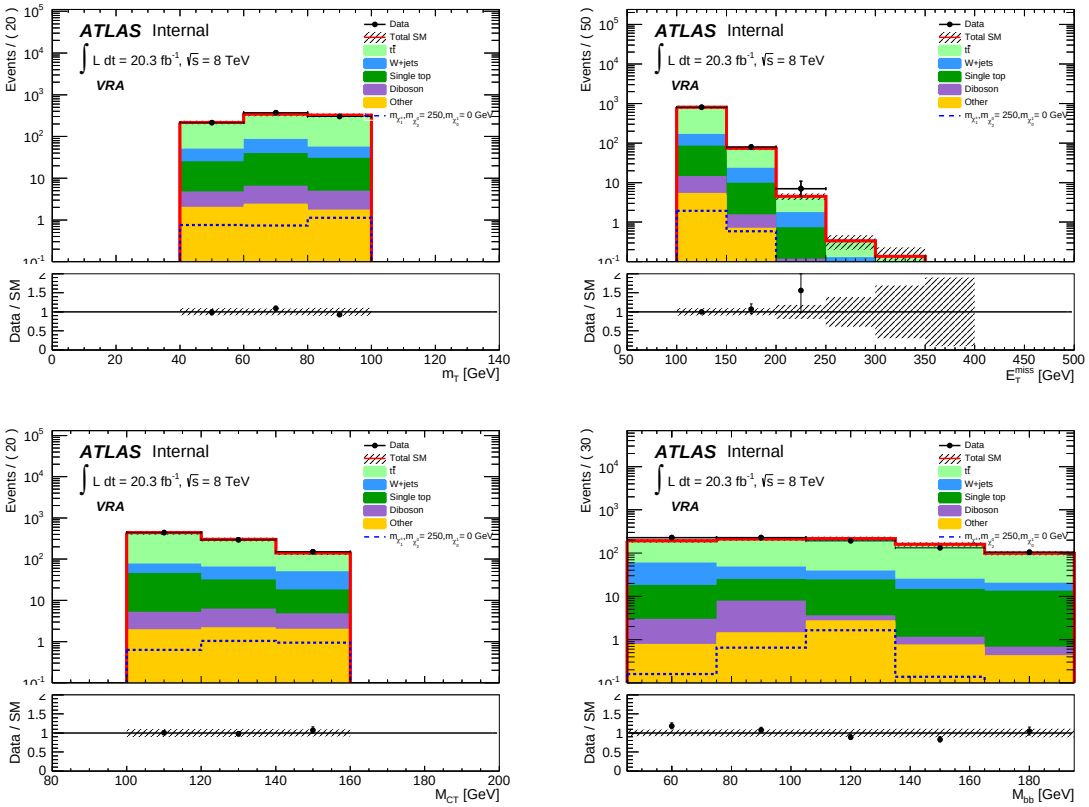

Figure 6.23: Distribution of data and background estimate in VBA for the blinded background only fit. The data is the black dots in the plot and all systematics are included.

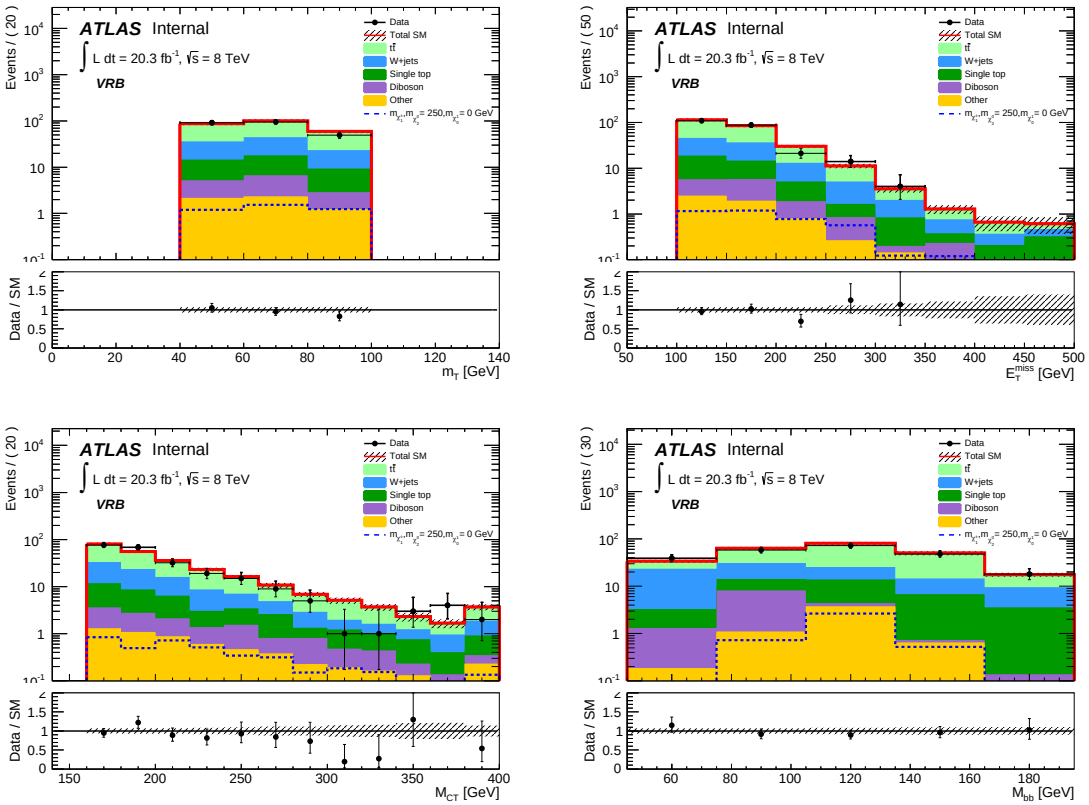

Figure 6.24: Distribution of data and background estimate in VRB for the blinded background only fit. The data is the black dots in the plot and all systematics are included.

The good agreement between data and our blinded background estimates gives confidence that the background model is performing well and accurately predicting the level of expected Standard Model background. Based on this, it is possible to finally unblind the analysis.

6.16 Results

For the unblinded fit, we perform another background only fit, except this time, we use the all of the m_{bb} bins, not just the side-band bins. From the fit, we do not observe any statistically significant excess over the Standard Model prediction in the signal regions and the observed number of events agrees with the fitted number of background events within the error bars. The results from this fit is shown in Table 6.18.

table.results.yields channel	CRT	CRW	SRAsb	SRBsb	SRAh	SRBh
Observed events	651	1547	14	10	4	3
Fitted bkg events	641.52 ± 24.91	1557.60 ± 38.64	12.50 ± 2.12	8.53 ± 1.53	5.69 ± 1.10	2.67 ± 0.69
Fitted $t\bar{t}$ events	606.80 ± 25.27	676.25 ± 56.56	7.48 ± 2.14	2.87 ± 1.20	3.57 ± 1.04	1.26 ± 0.57
Fitted W+jets events	11.15 ± 1.60	694.16 ± 59.67	2.65 ± 0.48	1.72 ± 0.32	0.56 ± 0.25	0.25 ± 0.13
Fitted Single top events	19.49 ± 3.50	111.35 ± 13.63	1.84 ± 0.57	2.46 ± 1.09	1.27 ± 0.36	0.71 ± 0.36
Fitted Diboson events	2.24 ± 0.35	64.13 ± 7.60	0.33 ± 0.11	1.09 ± 0.16	0.00 ± 0.00	0.21 ± 0.04
Fitted Other events	1.84 ± 0.29	11.69 ± 1.00	0.20 ± 0.04	0.40 ± 0.09	0.28 ± 0.04	0.24 ± 0.05
MC exp. SM events	547.96 ± 101.78	1703.17 ± 90.93	11.23 ± 3.27	7.79 ± 2.00	4.98 ± 1.69	2.24 ± 0.94
MC exp. $t\bar{t}$ events	511.65 ± 100.95	636.62 ± 93.49	5.83 ± 3.09	2.01 ± 1.55	2.79 ± 1.49	0.90 ± 0.75
MC exp. W+jets events	13.73 ± 1.59	880.52 ± 2.60	3.19 ± 0.55	2.18 ± 0.41	0.67 ± 0.39	0.30 ± 0.20
MC exp. Single top events	18.69 ± 3.78	111.59 ± 15.13	1.66 ± 0.58	2.14 ± 1.10	1.24 ± 0.40	0.60 ± 0.35
MC exp. Diboson events	2.05 ± 0.45	62.80 ± 8.72	0.36 ± 0.17	1.07 ± 0.16	0.00 ± 0.00	0.21 ± 0.05
MC exp. Other events	1.85 ± 0.32	11.63 ± 1.21	0.19 ± 0.05	0.40 ± 0.10	0.27 ± 0.05	0.23 ± 0.05

Table 6.18: The expected number of background events in each region derived from Monte Carlo before and after the full fit done using HistFitter, along with the number of observed events.

In Table 6.19, we have the breakdown of the systematic uncertainties for the full fit which doesn't spring any surprises on us compared to what we have seen previously.

In Figures 6.25 and 6.26 we have the distributions of m_{bb} in SRA and SRB after the full fit. We find good agreement with the Standard Model background estimates.

Region	CRT	CRW	SRAsb	SRBsb	SRAh	SRBh
Total background expectation	641.52	1557.59	12.50	8.53	5.69	2.67
Total statistical ($\sqrt{N_{\text{exp}}}$)	±25.33	±39.47	±3.54	±2.92	±2.38	±1.63
Total background systematic	±24.91[3.88%]	±38.63[2.48%]	±2.12[16.96%]	±1.53[17.93%]	±1.10[19.40%]	±0.69[25.72%]
$t\bar{t}$ factorization scale uncertainty	± 0.57	±0.36	±1.01	±0.38	±0.48	±0.16
$t\bar{t}$ generator uncertainty	±32.06	±32.55	±2.28	±1.31	±1.09	±0.57
$t\bar{t}$ parton shower uncertainty	±80.02	±61.34	±0.64	±0.39	±0.31	±0.17
$t\bar{t}$ renormalization uncertainty	±1.25	±0.78	±0.69	±0.11	±0.33	±0.05
$t\bar{t}$ ISR/FSR uncertainty	±30.43	±22.36	±0.82	±0.31	±0.39	±0.14
$t\bar{t}$ Normalization Uncertainty	±84.78	±94.48	±1.05	±0.40	±0.50	±0.18
Theoretical W+jet Uncertainties	±0.58	±0.57	±0.19	±0.14	±0.04	±0.02
W+jets Normalization Uncertainty	±0.96	±59.80	±0.23	±0.15	±0.05	±0.02
Single top Wt-channel generator+interference Uncertainty	±1.48	±5.20	±0.37	±1.02	±0.25	±0.31
Single top Wt-channel Parton Shower Uncertainty	±2.42	±8.20	±0.20	±0.03	±0.13	±0.01
Theoretical s and t-channel Single top Uncertainties	±0.28	±2.16	±0.03	±0.01	±0.02	±0.00
Jet Energy Scale	±28.04	±21.41	±0.54	±0.37	±0.36	±0.35
Jet Energy Resolution	±0.84	±0.07	±0.12	±0.05	±0.06	±0.11
B-tagging Scale Factors	±13.17	±9.99	±0.68	±0.36	±0.34	±0.12
Muon Instrumental Uncertainties	±0.92	±1.49	±0.07	±0.17	±0.07	±0.03
Electron Instrumental Uncertainties	±2.92	±2.89	±0.16	±0.09	±0.14	±0.09
PDF Uncertainity	±5.97	±5.37	±0.07	±0.05	±0.09	±0.05
Shape Uncertainity	±0.00	±0.00	±0.73	±0.65	±0.48	±0.33
Other	±8.23	±15.47	±0.46	±0.23	±0.21	±0.13

Table 6.19: Systematic uncertainties breakdown for all regions after the unblinded fit.

6.17 Interpretation

While it is disappointing that no signal excess was observed, we can still use these results to constrain the existing models. The results are obtained using the Frequentist hypothesis tests described earlier based on the profiled likelihood test statistic with the CL_S approach.

We can also set an upper limit on the model independent cross section based on the data we observe in the signal regions. The fit in the SR is done using the same setup as the fits in the previous section, except now we use the number of observed events in each m_{bb} bin of the signal region as an input to the fit. We solve for the value of μ_{sig} when the CL_s value falls below 0.05 which is the threshold for a 95% CL upper limit. This also allows us to obtain the 95% CL upper limit on the number of events in a beyond the Standard Model prediction for each SR. The hypothesis tests are done using both the asymptotic approximation and by also running psuedo-experiments

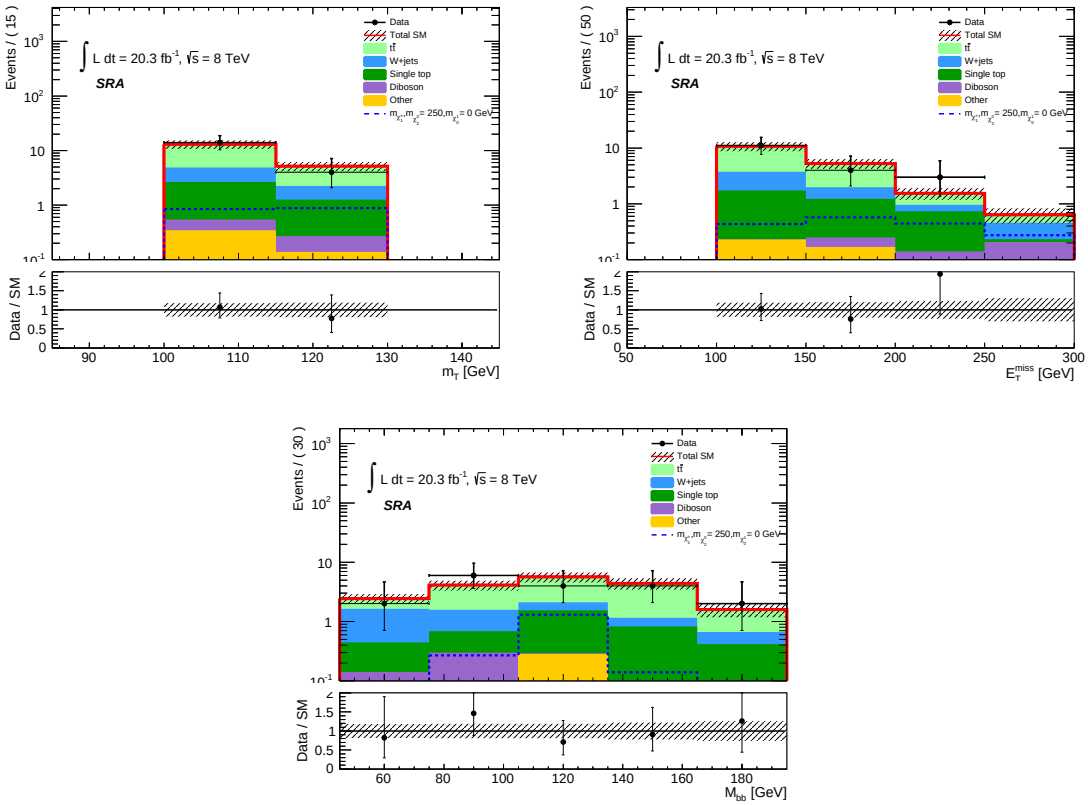

Figure 6.25: Distribution of data and background estimate in SRA for the full fit. The data is the black dots in the plot and all systematics are included.

with 10,000 toys and the results are shown below in Table 6.20.

SR	N_{exp}	N_{obs}	S^{95}_{exp}	S^{95}_{obs}	$\langle\epsilon\sigma\rangle^{95}_{\text{obs}}$[fb]	CL_B	$p(s=0)$
SRAh (toys)	5.69 ± 1.10	4	$6.3^{+2.6}_{-1.3}$	5.6	0.27	0.27	0.50
SRAh (asym)	5.69 ± 1.10	4	$6.3^{+3.4}_{-2.0}$	5.3	0.26	0.28	0.50
SRBh (toys)	2.67 ± 0.69	3	$5.1^{+2.2}_{-1.2}$	5.6	0.28	0.61	0.43
SRBh (asym)	2.67 ± 0.69	3	$5.1^{+2.6}_{-1.4}$	5.5	0.27	0.56	0.43

Table 6.20: Expected and observed event counts, expected and observed 95% CL upper limits for BSM predictions in each SR, along with the upper limit on the visible cross section.

The μ_{sig} upper limit is converted into an upper limit on the the visible cross section of new physics by normalizing to the integrated luminosity of the data sample. Here,

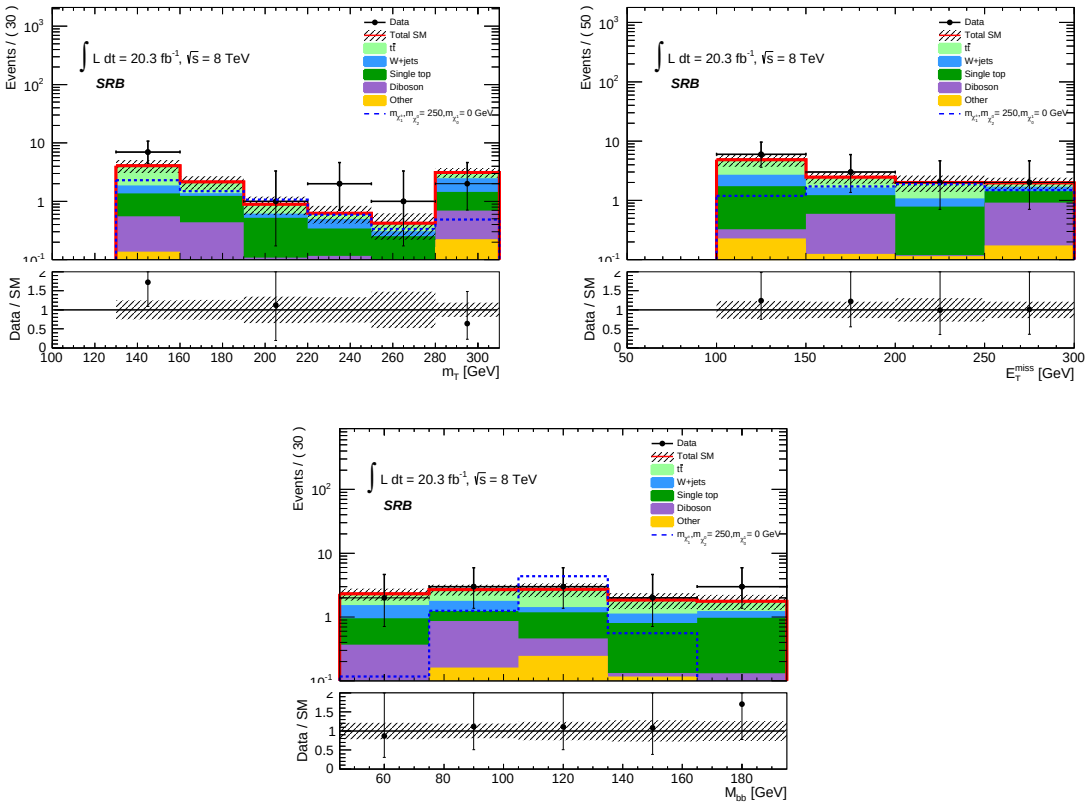

Figure 6.26: Distribution of data and background estimate in SRB for the full fit. The data is the black dots in the plot and all systematics are included.

the σ is really the product of acceptance, reconstruction efficiency, and production cross section.

The first two columns (N_{exp} and N_{obs}) give the expected (background only) and observed event counts in the signal regions. Columns three and four (S^{95}_{exp} and S^{95}_{obs}) are those same values, but now at the 95% CL upper limit for BSM physics (model independent). The CL_B can be interpreted to be the confidence level observed assuming the background-only hypothesis. The last column is the discovery p-value derived from the background only hypothesis test, which is capped at 0.5.

We also set limits in the context of two types of SUSY models, Simplified Models and pMSSM models as shown in the next two sections.

6.17.1 Simplified Model Limits

Limits can be set in the context of Simplified Models which we described previously. We can set an exclusion in the $m_{\tilde{\chi}_1^0} - m_{\tilde{\chi}_1^\pm}$ plane which are the only two free parameters in these particular SUSY models. For the model dependent signal limit fit, we calculate the expected and observed CL_S values for the background plus signal model. A CL_S of <0.05 would imply that our observed (or expected) test statistic is incompatible with the null hypothesis of $s + b$ and we can exclude such regions.

The expected exclusion is derived from Monte Carlo where the null hypothesis is $s+b$ and the alternative we test is no signal, only background. The observed exclusion comes from data where we test the fitted background estimate plus signal hypothesis against the actual observation. Thus, if we observe an excess, the observed limit will be weaker at that point (i.e. we would exclude less). Likewise, if we observe a downward fluctuation, then we would get a slightly better limit, although the CL_S prescription prevents us from getting a limit better than the experimental sensitivity. The results are shown below in Figure 6.27.

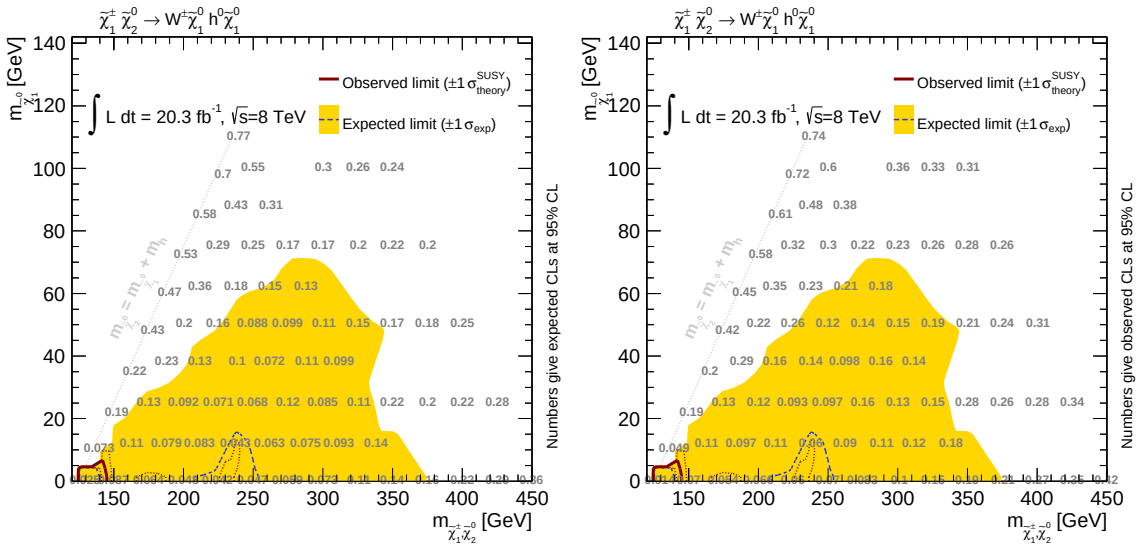

Figure 6.27: The Simplified Model 95% CL exclusion region in the $m_{\tilde{\chi}_1^0} - m_{\tilde{\chi}_1^\pm}$ plane. The numbers on the plots are the CL_S values from the hypothesis test for the expected limit (left) and observed limit (right).

The $\pm 1\sigma$ region on the expected limited (the yellow region) is derived from the experimental uncertainty band (statistical and systematic). For the observed limit, the $\pm 1\sigma$ region (the dashed red lines) comes from scaling the SUSY theoretical cross section by $\pm 1\sigma$ and therefore increasing/decreasing the signal hypothesis that is tested against the observation. We see that we are able to exclude a small region of phase space at lower $m_{\tilde{\chi}_1^0}$ and lower $m_{\tilde{\chi}_1^\pm}$ values. Because we have a slight excess in SRB, our observed limit is worse and we aren't able to exclude in the low $m_{\tilde{\chi}_1^0}$ region between $200 < m_{\tilde{\chi}_1^\pm}, m_{\tilde{\chi}_2^0} < 250$ GeV.

6.17.2 pMSSM Limits

The same limits are produced now as in the Simplified Model case, except now we assume the pMSSM model. Here, the quantity of interest is μ (Higgs mass parame-

ter). In the split-SUSY scenarios which are less constrained by previous experimental results, μ is generally accepted to be in the approximately 500 GeV range. For such values of μ, the Higgsinos become decoupled and $\tilde{\chi}_2^0$ and $\tilde{\chi}_1^\pm$ are almost pure wino and become mass degenerate, with mass M_2. Here, we assume that $m_{\tilde{\chi}_1^0}$ is fixed at 50 GeV. The exclusion plot is show below in Figure 6.28.

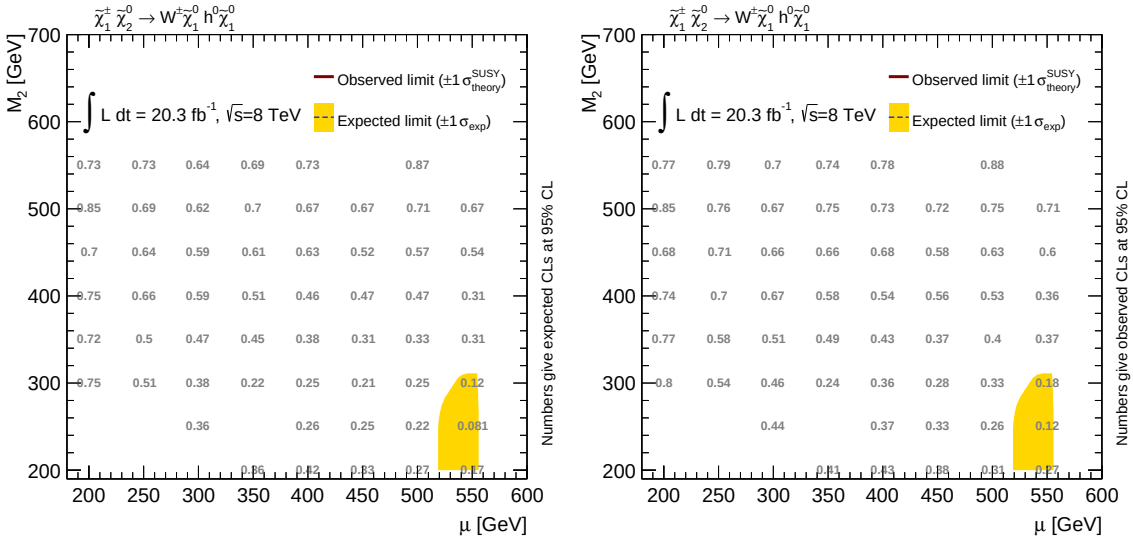

Figure 6.28: The Simplified Model 95% CL exclusion region in the $M_2 - \mu$ plane. The numbers on the plots are the CL_S values from the hypothesis test for the expected limit (left) and observed limit (right).

Because here $m_{\tilde{\chi}_1^0}$ is higher and we have to contend with a significantly lower production cross section, we are unable to exclude any of the phase space although we do have some experimental sensitivity at larger values of μ.

Chapter 7

Conclusion and Outlook

A search for direct production of $pp \to \tilde{\chi}_2^0\tilde{\chi}_1^\pm$ followed by $\tilde{\chi}_2^0 \to \tilde{\chi}_1^0 h(\to b\bar{b})$ has been performed using 20.3 fb^{-1} of $\sqrt{s} = 8$ TeV proton-proton collision data recorded with the ATLAS detector. All of the observations are consistent with the Standard Model predictions and 95% confidence level limits are obtained in the context of both simplified supersymmetric models and phenomenological Minimal Supersymmetric Standard Models.

Parallel analyses performed using final state signatures with one lepton and two photons, and two same-sign leptons, in association with $\not{E}_T$ were also found to be consistent with the Standard Model. When limits are set in the Simplified Model by combining those two final states with the one studied here, we find that the common masses of $\tilde{\chi}_2^0$ and $\tilde{\chi}_1^\pm$ can be excluded up to 250 GeV in the case of a massless $\tilde{\chi}_1^0$ [24]. The result of this combination is shown in Figure 7.1. The contribution from the analysis described in this thesis is shown by the green line corresponding to the

lbb observed limit.

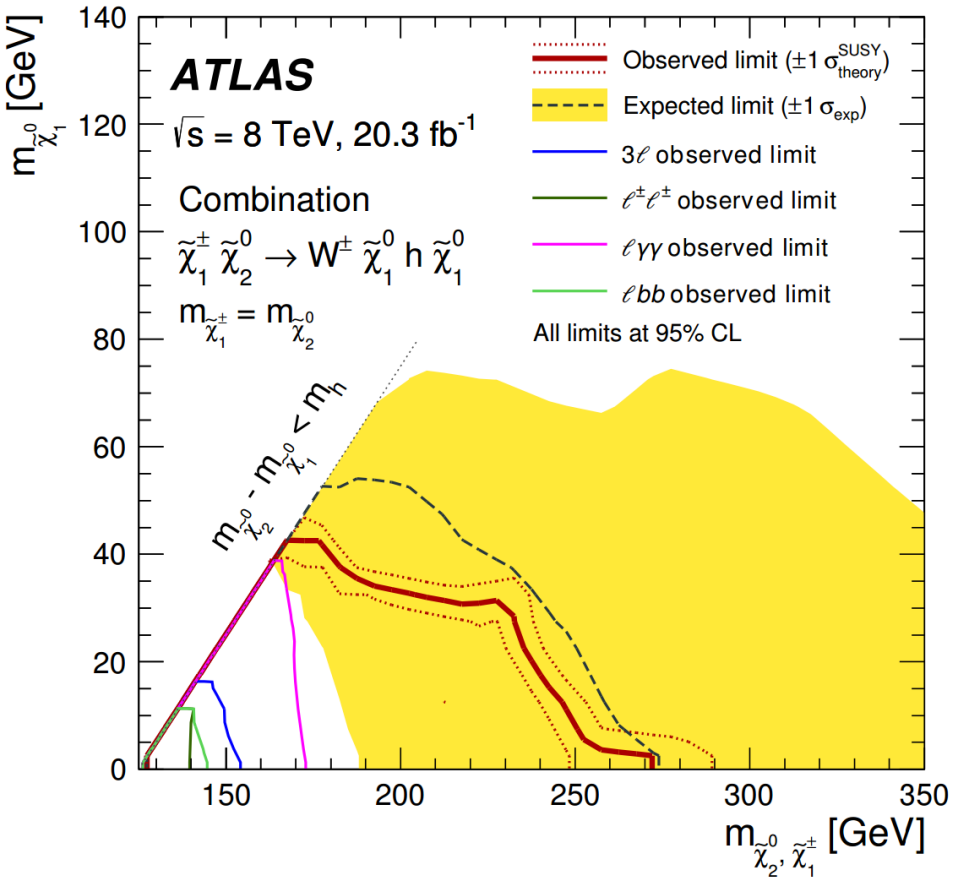

Figure 7.1: The Simplified Model 95% CL exclusion region in the $m_{\tilde{\chi}_1^0} - m_{\tilde{\chi}_1^\pm}$ plane for the combined analysis.

With the 13 TeV ATLAS Run II data, it will be possible to improve upon these results as there will be a factor of 3 increase in the signal production cross sections. However, gains will only be realised if the *b*-jet calibration is done again and validated using the same techniques discussed in Chapter 5. Furthermore, to take full advantage of the 3000 fb^{-1} of data ATLAS will collect at the High Luminosity LHC, the New Small Wheel detector upgrade discussed in Chapter 4 will be necessary. In particular, excellent detector simulation will be necessary to ensure that the NSW we build is

capable of reaching the performance goals. Assuming this work is done successfully, the LHC will continue to be an exciting experiment for many years to come.

Bibliography

[1] http://www.quantumdiaries.org/2014/03/14/the-standard-model-a-beautiful-but-flawed-theory/.

[2] https://inspirehep.net/record/1252561/plots.

[3] http://www.atlas.ch/photos/lhc.html.

[4] http://www.lhc-closer.es/1/4/7/2.

[5] http://hepwww.rl.ac.uk/OpenDays97/Atlas_SCT_sidetector.htm.

[6] S. Agostinelli et al. GEANT4: A Simulation toolkit. *Nucl.Instrum.Meth.*, A506:250–303, 2003.

[7] B.C. Allanach. SOFTSUSY: a program for calculating supersymmetric spectra. *Comput.Phys.Commun.*, 143:305–331, 2002.

[8] The ATLAS Collaboration. Atlas data periods. https://twiki.cern.ch/twiki/bin/viewauth/AtlasProtected/DataPeriods.

[9] The ATLAS Collaboration. Expected Performance of the ATLAS Detector. ATLAS publication: CERN-OPEN-2008-020.

[10] The ATLAS Collaboration. Jet energy measurement and systematic uncertainties using tracks for jets and for b-quark jets produced in proton-proton collisions at $\sqrt{s} = 7$ TeV in the ATLAS detector. ATLAS conference note: ATLAS-CONF-2013-002.

[11] The ATLAS Collaboration. Pile-up subtraction and suppression of jets in ATLAS. ATLAS conference note: ATLAS-CONF-2013-083.

[12] The ATLAS Collaboration. Probing the measurement of jet energies with the ATLAS detector using Z+jet events from proton-proton collisions at $\sqrt{s} = 7$ TeV. ATLAS conference note: ATLAS-CONF-2012-053.

[13] The ATLAS Collaboration. Properties of jets and inputs to jet reconstruction and calibration with the ATLAS detector using proton-proton collisions at $\sqrt{s} = 7$ TeV. ATLAS Technical Report: ATLAS-CONF-2010-053.

[14] The ATLAS Collaboration. Search for Chargino and Neutralino Production in Final States with One Lepton, Two b-jets Consistent with a Higgs Boson, and Missing Transverse Momentum with the ATLAS detector. ATLAS internal note: ATLAS-COM-PHYS-2013-1640.

[15] The ATLAS Collaboration. Search for direct production of charginos and neutralinos in events with three leptons and missing transverse momentum in 21 fb^{-1} of pp collisions at $\sqrt{s} = 8$ TeV with the ATLAS detector. ATLAS Conference Note: ATLAS-CONF-2013-035.

[16] The ATLAS Collaboration. Search for direct-slepton and direct-chargino production in final states with two opposite-sign leptons, missing transverse momentum and no jets in 20 fb^{-1} of pp collisions at $\sqrt{s} = 8$ TeV with the ATLAS detector. ATLAS Conference Note: ATLAS-CONF-2013-049.

[17] The ATLAS Collaboration. Search for direct-slepton and direct-chargino production in final states with two opposite-sign leptons, missing transverse momentum and no jets in 20 fb^{-1} of pp collisions at $\sqrt{s} = 8$ TeV with the ATLAS detector. ATLAS-COM-CONF-2013-050.

[18] The ATLAS Collaboration. Search for strong production of supersymmetric particles in final states with missing transverse momentum and at least three b-jets using 20.1 fb^{-1} of pp collisions at $\sqrt{s} = 8$ TeV with the ATLAS Detector. ATLAS Conference Note: ATLAS-CONF-2013-061.

[19] The ATLAS Collaboration. Search for supersymmetry in events with four or more leptons in 21 fb^{-1} of pp collisions at $\sqrt{s} = 8$ TeV with the ATLAS detector. ATLAS Conference Note: ATLAS-CONF-2013-036.

[20] The ATLAS Collaboration. Susyd3pdmaker. https://twiki.cern.ch/twiki/bin/view/AtlasProtected/SUSYD3PDMaker.

[21] The ATLAS Collaboration. The ATLAS Experiment at the CERN Large Hadron Collider. *JINST*, 3:S08003, 2008.

[22] The ATLAS Collaboration. *Expected performance of the ATLAS experiment: detector, trigger and physics*. CERN, Geneva, 2009.

[23] The ATLAS Collaboration. *Technical Design Report: New Small Wheel*. CERN, Geneva, 2013.

[24] The ATLAS Collaboration. Search for direct pair production of a chargino and a neutralino decaying to the 125 GeV Higgs boson in $\sqrt{s} = 8$ TeV pp collisions with the ATLAS detector. *Eur. Phys. J. C*, 75:208, 2015.

[25] The CMS Collaboration. Search for electroweak production of charginos, neutralinos, and sleptons using leptonic final states in pp collisions at $\sqrt{s} = 8$ TeV. CMS Note: CMS-PAS-SUS-13-006.

[26] The CMS Collaboration. Search for top-squark pair production in the single lepton final state in pp collisions at 8 TeV. CMS Note: CMS-PAS-SUS-13-011.

[27] G. Corcella et al. HERWIG 6: an event generator for Hadron Emission Reactions With Interfering Gluons. *JHEP*, 010:0101, 2001.

[28] Patrick Draper, Patrick Meade, Matthew Reece, and David Shih. Implications of a 125 GeV Higgs for the MSSM and Low-Scale SUSY Breaking. *Phys.Rev.*, D85:095007, 2012.

[29] A. Denner et al. NLO QCD corrections to $WWbb$ production at hadron colliders. *Phys.Rev.Lett*, 106:052001, 2011.

[30] G. Aad et al. Search for the Standard Model Higgs boson in associated production with a vector boson and decaying to botton quarks with the ATLAS detector. ATLAS internal note: ATL-COM-PHYS-2013-465.

[31] G. Aad et al. Search for squarks and gluinos with the ATLAS detector in final states with jets and missing transverse momentum using 4.7 fb^{-1} of $\sqrt{s} = 7$ TeV proton-proton collision data. *Phys.Rev.D*, 0012008:087, 2013.

[32] G. Iakovidis et al. Micromegas under magnetic field for the nsw. http://indico.cern.ch/event/197577/contribution/3/0/material/slides/0.pdf.

[33] L. Ancu et al. Search for supersymmetry in events with three leptons and missing transverse momentum in 20.3 fb^{-1} pp collisions at $\sqrt{s} = 8$ TeV with the ATLAS detector. ATLAS internal note: ATL-COM-PHYS-2013-888.

[34] M. Baak et al. HistFitter software framework for statistical data analysis. Technical report, CERN, Geneva, Switzerland, Oct 2014.

[35] M. Cacciari et al. The anti-k_t jet clustering algorithm. *JHEP*, 04:063, 2008.

[36] S. Amoroso et al. Search for squarks and gluinos using final states with jets and missing transverse momentum with the ATLAS experiment in $\sqrt{s} = 8$ TeV proton-proton collisions. ATLAS internal note: ATL-PHYS-INT-2012-063.

[37] D. Farhi. Overview of the standard model lagrangian. Harvard Physics Summer 2012 Theory Study Group.

[38] A. Farbin for the ATLAS Collaboration. ATLAS Analysis Model. *Journal of Physics: Conference Series*, 119(042012), 2008.

[39] ATLAS SUSY Working Group. Summary plots for the atlas supersymmetry physics group. https://atlas.web.cern.ch/Atlas/GROUPS/PHYSICS/CombinedSummaryPlots/SUSY/.

[40] The ATLAS Egamma Performance Group. Medium electrons technical wiki. https://twiki.cern.ch/twiki/bin/viewauth/AtlasProtected/TechnicalitiesForMedium1.

[41] The ATLAS JetEtMiss Working Group. How to clean jets. https://twiki.cern.ch/twiki/bin/view/AtlasProtected/HowToCleanJets.

[42] The ATLAS Muon Combined Performance Group. Mcp analysis guidelines. https://twiki.cern.ch/twiki/bin/view/AtlasProtected/MCPAnalysisGuidelinesRel15.

[43] The ATLAS SUSY Working Group. Histfitter twiki. https://twiki.cern.ch/twiki/bin/viewauth/AtlasProtected/SusyFitter.

[44] The ATLAS SUSY Working Group. Susysignaluncertainties twiki. https://twiki.cern.ch/twiki/bin/viewauth/AtlasProtected/SUSYSignalUncertainties.

[45] The ATLAS SUSY Working Group. Susytools svn. https://svnweb.cern.ch/trac/atlasoff/browser/PhysicsAnalysis/SUSYPhys/SUSYTools.

[46] The AtlasSLAC JetMETbTagAnalysis Group. The proofana analysis framework. https://twiki.cern.ch/twiki/bin/viewauth/AtlasSandboxProtected/ProofAna.

[47] A.D. Martin et al. Parton distributions for the LHC. arXiv:hep-ph/0901.0002.

[48] S. Martin. A Supersymmetry Primer. arXiv:hep-ph/9709356v6, 2011.

[49] H. Miyazawa. Baryon Number Changing Currents. *Prog. Theor. Phys.*, 36:1266–1276, 1966.

[50] H. Murayama. Supersymmetry Phenomenology. arXiv:hep-ph/0002232v2, 2000.

[51] A. Neveu and J.H. Schwarz. Factorizable dual model of pions. *Nucl. Phys. B.*, 31:86–112, 1971.

[52] Instrument Design Weizmann Institute of Science. Tgc with mm on small wheel. 2012.

[53] D. Pitzl. Detector for particle physics. DESY Summer Student Lectures 4.8.2009.

[54] P. Ponsot. Atlas nsw layout meeting 06/07/2012.

[55] J. Pumplin et al. Inclusive Jet Production, Parton Distributions, and the Search for New Physics. arXiv:hep-ph/0303013.

[56] P. Ramond. Dual Theory for Free Fermions. *Phys. Rev. D.*, 3:2415–2418, 1971.

[57] The TMVA team. TMVA Users Guide. http://tmva.sourceforge.net/docu/TMVAUsersGuide.pdf.

[58] M. Titov. Radiation Damage and Long-Term Aging in Gas Detectors. *ICFA Instrum.Bull.*, 26:002, 2004.

[59] Daniel R. Tovey. On measuring the masses of pair-produced semi-invisibly decaying particles at hadron colliders. *JHEP*, 0804:034, 2008.

[60] R. Schapire Y. Freund. A Decision-Theoretic Generalization of On-Line Learning and an Application to Boosting. *Journal of Computer and System Sciences*, 55:119–139, 1997.